

UCLA

UCLA Electronic Theses and Dissertations

Title

Lensfree Holographic Microscopy and Wide-field Optical Imaging using Wetting Films and Nano-Lenses

Permalink

<https://escholarship.org/uc/item/4cs8x43g>

Author

Mudanyali, Onur

Publication Date

2012

Peer reviewed|Thesis/dissertation

UNIVERSITY OF CALIFORNIA

Los Angeles

Lensfree Holographic Microscopy and Wide-field Optical
Imaging using Wetting Films and Nano-Lenses

A dissertation submitted in partial satisfaction of the
requirements for the degree Doctor of Philosophy
in Electrical Engineering

by

Onur Mudanyali

2012

© Copyright by

Onur Mudanyali

2012

ABSTRACT OF THE DISSERTATION

Lensfree Holographic Microscopy and Wide-field Optical
Imaging using Wetting Films and Nano-Lenses

By

Onur Mudanyali

Doctor of Philosophy in Electrical Engineering

University of California, Los Angeles, 2012

Professor Aydogan Ozcan, Chair

Impressive revolution of optical imaging and microscopy architectures has been expanding our horizon and increasing the opportunities in medical diagnostics. Although we experience significant advancements such as better resolution, speed and throughput, advanced imaging platforms are still complex, bulky and expensive, such that their function beyond well-established clinical environment is quite limited. Therefore, innovative imaging techniques are necessary to combat global health problems in resource-scarce settings where health care infrastructure is extremely limited or does not even exist. In such poor settings, imaging devices should be compact, robust, cost-effective and easy to use, without a trade-off in their performance.

Centered on this vision, here I demonstrate a new lensfree on-chip microscopy and nanoparticle imaging platform based on partially-coherent digital in-line holography, providing a

highly-sensitive and high-throughput approach for rapid medical diagnostics and screening, especially for field settings and resource-limited environments. This computational microscopy and nano-particle imaging platform achieves subcellular spatial resolution and also directly images, for the first time in on-chip microscopy, single sub-100 nm particles using self-assembled aspheric liquid nano-lenses around individual nano-particles across a large field-of-view of $>20 \text{ mm}^2$, i.e., more than two orders-of-magnitude larger than existing nano-imaging techniques.

This platform does not utilize any lenses, lasers or other bulky optical/mechanical components which greatly simplifies its architecture making it portable, light-weight, and cost-effective. It has been successfully implemented on a compact stand-alone unit which weighs only ~46 grams with dimensions smaller than 4.2 x 4.2 x 5.8 cm as well as on a commercially-available cell-phone that is modified with a light-weight (~ 38 grams) hardware attachment.

Using stable and biocompatible wetting films to self-assemble aspheric liquid nano-lenses around individual nano-particles, I also introduce a wide-field on-chip microscopy modality that is capable of directly imaging single nano-particles and viruses (i.e., adenoviruses and influenza A (H1N1) viral particles) within a field-portable design.

Creating new opportunities for rapid medical diagnostics in point-of-care and field conditions, this lensfree microscopy and nano-particle imaging toolset may bring improved healthcare delivery especially to resource-poor regions of the world and may significantly benefit our fight against various global health challenges including HIV, malaria, waterborne diseases and viral infections.

The dissertation of Onur Mudanyali is approved.

Warren Bicknell Mori

Oscar M. Stafsudd

Dino Di Carlo

Aydogan Ozcan, Committee Chair

University of California, Los Angeles

2012

Table of Contents

Chapter 1	Introduction.....	1
Chapter 2	Lensfree Partially-Coherent In-Line Holographic Imaging.....	6
2.1	Introduction.....	6
2.2	Theoretical Analysis of Digital Lensfree In-Line Holographic Imaging.....	8
2.3	Image Reconstruction in Digital Lensfree In-Line Holographic Imaging.....	16
2.4	Discussions	23
Chapter 3	Compact, Light-weight and Cost-effective Lensfree Microscopy.....	27
3.1	Introduction.....	27
3.2	Portable Lensfree Telemedicine Microscope.....	28
3.3	Lensfree Microscopy on a Cellphone	34
Chapter 4	Lensfree Microscopy for Global Health Applications.....	42
4.1	Water Quality Management using Field-Portable Lensfree Holographic Microscopes	42
4.2	Lensfree Imaging of Antibody Microarrays for High-Throughput On-Chip Detection of Leukocyte Numbers and Function	49
Chapter 5	Lensfree Super-Resolution Microscopy using Wetting Films on a Chip	58
5.1	Introduction.....	58
5.2	Experimental Methods	60
5.3	Experimental Results and Discussion.....	63
Chapter 6	Wide-Field Optical Imaging of Single Nano-Particles and Viruses using On-Chip Microscopy and Self-Assembled Liquid Nano-Lenses	72
6.1	Introduction.....	72

6.2	Experimental Methods	73
6.3	Experimental Results and Discussion.....	81
Chapter 7	Conclusion	95
Appendix:	Smart Rapid Diagnostics Test Reader running on a Cell-Phone for Real-time Mapping of Epidemics	98
References	114

Acknowledgements

First and foremost, I am deeply grateful to my advisor Prof. Aydogan Ozcan for his patience, guidance and support throughout my PhD study at UCLA. I admire his dedication, vision and enthusiasm for research that have profound influence on my professional career. It is a privilege to be one of his first students and I would like to thank him for giving me this opportunity.

I would like to also thank my doctoral committee members, Prof. Dino Di Carlo, Prof. Oscar Stafsudd and Prof. Warren Bicknell Mori for their time, helpful comments and feedback that significantly helped me to improve the quality and the clarity of this PhD dissertation.

Since 2008, I have been so lucky to know and collaborate with many great people including Waheb Bishara, Serhan O. Isikman, Derek Tseng, Alon Greenbaum, Wei Luo, Ikbal Sencan, Ahmet F. Coskun, Euan McLeod, Uzair Sikora, Yunbo Liu, Sam Mavandadi, Ting-Wei Su, Hongying Zhu, Anthony Erlinger, Cetin Oztoprak, Caglar Arpali, Serap Arpali, Oguzhan Yaglidere, Isa Navruz, Qingshan Wei, Gabriel Biener, Justin Wong, Zoltan Gorocs, Bahar Khademhosseinieh, Myungjun Lee, Meng Yu, Swati Padmanabhan, Liang Xue, Steve Feng, Frank Yu, Stoyan Dimitrov, Liang Xue and others. I would like thank these brilliant members of Ozcan research Group.

In addition, I have collaborated with many influential scientist and researcher who contributed to my research in various ways, therefore I would like to thank Prof. Alexander Revzin and Dr. Gulnaz Stybayeva (UC Davis Biomedical Engineering Department, USA), Prof. Dino Di Carlo, and his students Dr. Danny Gossett, Dr. Albert J. Mach, Dr. Westbrook Weaver and Ivan Pushkarsky (UCLA Bioengineering Department, USA), Dr. Yves Hennequin and Dr.

Cédric P. Allier (CEA, LETI, MINATEC, France), Prof. Karin Nielsen and Dr. Santhosh Nadipuram (David Geffen UCLA School of Medicine, USA), Dr. Rajendranath Ramasawmy (Fundação de Medicina Tropical do Amazonas, Brazil) and Prof. Shirley Luckhart (UC Davis Department of Medical Microbiology and Immunology, USA).

Finally, I would like to express my deepest gratitude to my family to whom I owe everything. I would like to thank my mom, dad, grandma and grandpa who gifted me this life and support me in every possible way in every moment of it. I want to also thank my best friend and wife, Pelin, who I met just before this long journey, has been the source of energy, motivation and support. Therefore, I dedicate this dissertation to my family.

Vita

Onur Mudanyali received BSc and MSc degrees in Electronics and Communication Engineering from Istanbul Technical University (ITU). In 2008, he joined the University of California, Los Angeles (UCLA) to pursue his PhD Degree in Electrical Engineering. He is the recipient of the Undergraduate Merit Scholarship (ITU), the Graduate Scholarship of the Scientific and Technological Research Council of Turkey (TUBITAK), the International PhD Fellowship of The Council of Higher Education of Turkey (YOK), the 2011 UCLA Tech Forum poster award, the 2012 SPIE Scholarship in Optics and Photonics and conference travel grant from National Science Foundation (NSF) in 2012. He is the author/co-author of 2 book chapters and over 50 research articles in scientific journals and conferences.

Selected Publications

O. Mudanyali, A. Erlinger, S. Seo, Ting-Wei Su, D. Tseng, and A. Ozcan, “Lensless On-chip Imaging of Cells Provides a New Tool for High-throughput Cell-Biology and Medical Diagnostics,” *Journal of Visualized Experiments*, no. 34, December 2009.

S. O. Isikman, I. Sencan, O. Mudanyali, W. Bishara, C. Oztoprak, and A. Ozcan, “Color and Monochrome Lensless On-chip Imaging of *Caenorhabditis Elegans* Over a Wide Field-of-View,” *Lab on a Chip*, vol. 10, no. 9, pp. 1109-1112, March 2010.

G. Stybayeva, O. Mudanyali, S. Seo, J. Silangcruz, M. Macal, E. Ramanculov, S. Dandekar, A. Erlinger, A. Ozcan, and A. Revzin, “Lensfree Holographic Imaging of Antibody Microarrays for High-Throughput Detection of Leukocyte Numbers and Function,” *Analytical Chemistry*, vol. 82, no. 9, pp. 3736-3744, April 2010.

O. Mudanyali, D. Tseng, C. Oh, S.O. Isikman, I. Sencan, W. Bishara, C. Oztoprak, S. Seo, B. Khademhosseini, and A. Ozcan, “Compact, Light-weight and Cost-effective Microscope based on Lensless Incoherent Holography for Telemedicine Applications”, *Lab on a Chip*, vol. 10, no. 11, pp. 1417-1428, April 2010.

D. Tseng, O. Mudanyali, C. Oztoprak, S.O. Isikman, I. Sencan, O. Yaglidere, and A. Ozcan, "Lensfree Microscopy on a Cell-phone," *Lab on a Chip*, vol. 10, no. 14, pp. 1787-1792, May 2010.

Sungkyu Seo, Serhan O. Isikman, Ikbal Sencan, Onur Mudanyali, Ting-Wei Su, Waheb Bishara, Anthony Erlinger, and Aydogan Ozcan, "High-Throughput Lens-Free Blood Analysis on a Chip," *Analytical Chemistry*, vol. 82, no. 11, pp. 4621-4627, June 2010.

O. Mudanyali, C. Oztoprak, D. Tseng, A. Erlinger, and A. Ozcan, "Detection of waterborne parasites using field-portable and cost-effective lensfree microscopy", *Lab on a Chip*, vol. 10, no. 18, pp. 2419-2423, August 2010.

W. Bishara, U. Sikora, O. Mudanyali, T. Su, O. Yaglidere, S. Luckhart, and A. Ozcan, "Holographic pixel super-resolution in portable lensless on-chip microscopy using a fiber-optic array", *Lab on a Chip*, vol. 11, no. 7, pp. 1276-1279, March 2011.

O. Mudanyali, W. Bishara and A. Ozcan, "Lensfree Super-Resolution Holographic Microscopy using Wetting Films on a Chip", *Optics Express*, vol. 19, no. 18, pp. 17378-17389, August 2011.

S.O. Isikman, A. Greenbaum, M. Lee, W. Bishara, O. Mudanyali, Ting-Wei Su, and A. Ozcan, "Lensfree computational microscopy tools for cell and tissue imaging at the point-of-care and in low-resource settings," *Analytical Cellular Pathology*, vol. 35, no. 4, pp. 229-247, 2012.

O. Mudanyali, S. Dimitrov, U. Sikora, S. Padmanabhan, I. Navruz, and A. Ozcan, "Integrated Rapid-Diagnostic-Test Reader Platform on a Cellphone", *Lab on a Chip*, vol. 12, no. 15, pp. 2678-2686, April 2012.

S.O. Isikman, W. Bishara, O. Mudanyali, I. Sencan, T. Su, D. Tseng, O. Yaglidere, U. Sikora, and A. Ozcan, "Lensfree On-Chip Microscopy and Tomography for Bio-Medical Applications", *IEEE Journal of Selected Topics in Quantum Electronics (JSTQE)*, vol. 18, no. 3, pp. 1059-1072, May 2012.

H. Zhu, S.O. Isikman, O. Mudanyali, A. Greenbaum, and A. Ozcan, "Optical Imaging Techniques for Point-of-care Diagnostics", *Lab on a Chip*, DOI: 10.1039/C2LC40864C, 2012.

A. Greenbaum, W. Luo, T-W. Su, Z. Göröcs, L. Xue, S.O. Isikman, A.F. Coskun, O. Mudanyali, and A. Ozcan, "Imaging without lenses: achievements and remaining challenges of wide-field on-chip microscopy", *Nature Methods*, vol.9, no. 9, pp. 889-895, August 2012.

Chapter 1 Introduction

Optical microscopy and imaging occupies the center of attraction in various fields including engineering, physical sciences and medicine. Wondering about the realm of the nano-world, there has been a considerable effort to overcome the fundamental limitations and challenges of optical imaging. However, nano-scale objects are difficult to directly visualize using optical techniques because of their small size compared to the optical wavelength, resulting in a weak scattering signal from individual nano-particles. To mitigate this challenge, various innovative techniques¹⁻³⁰ have been developed to overcome the fundamental barriers of imaging (e.g., signal to noise ratio (SNR), throughput, and speed), including near-field optical microscopy,¹⁻⁴ super-resolution microscopy,^{5-10,21,22} atomic force microscopy,^{11,12} electron microscopy,¹³⁻¹⁶ and other recently developed imaging techniques.¹⁷⁻³⁰ While generally providing excellent resolution and imaging performance, all of these existing approaches, however, are relatively complex, bulky, expensive and low throughput with a limited imaging field-of-view (FOV). These limitations pose challenges in the detection and enumeration of sparse nano-scale objects, such as viral particles at low concentrations. This can especially be critical in e.g., early-stage disease diagnosis in point-of-care settings or resource-scarce environments, which ideally demand field-portable, cost-effective, and wide-field imaging and detection modalities that can create new opportunities towards medical diagnostics beyond well-established laboratories.

In parallel to the advancements in imaging modalities, we have been experiencing another revolution in digital technologies with solid state electronics such as opto-electronic detector arrays having significantly larger imaging areas with smaller pixels, better dynamic ranges, and frame rates, as well as much faster, cheaper and more powerful digital processors

and memories. Moreover, predicted by Moore's Law,³¹ the number of transistors on integrated circuits doubles approximately every 18 months, significantly increasing the performance of digital platforms. This on-going digital revolution, when combined with advanced imaging modalities and numerical techniques, also creates an opportunity for optical imaging to face another dimension in this renaissance towards simplification of the optical imaging apparatus, making it significantly more compact, light-weight, cost-effective and easy to use, potentially without a trade-off in its performance.

In the meantime, cell-phone subscriptions have reached to 5 billion by 2012, and the majority of these cellphones are being used in the developing parts of the world. In addition to this, 80% of the world population currently lives in locations that are already covered through wireless communication links such as GSM networks.^{32,33} These numbers will further grow in the near-future, where it is predicted that by 2015 more than 86% of the world population will own at least one cellphone.³⁴

This massive volume of wireless phone communication brings an enormous cost-reduction and unprecedented levels of access to cellphones despite their sophisticated hardware and software capabilities. Quite importantly, most of these existing cellphones are already equipped with advanced digital imaging and sensing platforms that can be utilized for various health monitoring applications. Similar to the predictions of Moore's Law, the performance and megapixel count of the mobile phone cameras has been doubling in approximately every 18 months. Considering the early generation cell-phones with 0.3 megapixel cameras in 2002, pixel count of mobile phone cameras has reached 41 megapixels in 2012, remarkably increasing the imaging performance of consumer grade mobile phones.^{35,36} Utilizing this advanced state-of-the-art of the cellphone technology towards medical diagnostics, imaging and/or sensing applications

can offer numerous opportunities to improve health care especially in the developing world where medical facilities and infrastructure are extremely limited or even do not exist. For this revolution in health care to occur, lab-on-a-chip systems that can potentially be miniaturized to the level of a handheld wireless unit are needed. Ideally, such systems should better be compatible with the existing designs of cellphones, which will make their wide-spread use in the developing world much more cost-effective (e.g., see Appendix).

Lensfree incoherent holographic on-chip imaging can be considered to be at the heart of this new opportunity and when combined with the advanced state of the art and cost-effective nature of digital electronics, it can provide a transformative solution to some of the unmet needs of cell biology and medical diagnostics especially for resource-limited environments.³⁷

Over the last few years, various lensfree on-chip imaging architectures were also demonstrated.^{32,37-52} Among these innovative approaches, lensfree computational holography^{32,37,39-43,45-52} deserves a special attention since with new computational algorithms and mathematical models,⁵³ it has the potential to make the most out of this digital revolution that we have been experiencing. In this context, lensfree digital in-line holography has already been successfully demonstrated for high-resolution microscopy of cells and other micro-organisms.^{40,46-52}

Conventional coherent lensfree in-line holography approaches demand near-perfect spatial coherence for illumination, and therefore require focusing of a laser light on a small aperture that is on the order of a wavelength for spatial filtering.^{40,43} The use of a small aperture size (e.g., 1-2 μm) requires a mechanically stable and a carefully aligned system together with a focusing lens to efficiently couple the laser radiation to the aperture for improved light throughput. In addition, keeping such a small aperture clean and operational over an extended

period of time can be another challenge especially for field use. Further, the objects (cells) of interest are typically positioned far away (e.g., >1 cm) from the sensor surface such that the holographic signature of each object (cell) is spread almost over the entire sensor area, where all the cells' signatures significantly overlap. Such an approach unfortunately limits the imaging field-of-view (FOV) at the cell plane. All these requirements not only relatively increase the cost and the size of the optical instrument, but also make lensfree coherent in-line holography somewhat inconvenient for use in resource limited settings.

Partially coherent or incoherent illumination sources in holography have also been utilized in different lens-based optical architectures.⁵⁴⁻⁵⁸ These holographic imaging techniques are not on-chip as they utilize various bulky optical components and therefore they can be considered under the same category as the advanced imaging modalities discussed in the introduction making them much less suitable for field use. Moreover, these approaches also suffer from a small field-of-view as they position the objects-of-interest far away from the sensor surface, e.g., with a fringe magnification of >10 , reducing the available field-of-view of the digital sensor by more than two orders of magnitude.⁴² Further, these studies used coupling optics for the illumination such as a microscope objective-lens and had relatively coarse imaging performance.

In this dissertation, I demonstrate a new lensfree on-chip microscopy and nano-particle imaging platform that operates based on partially-coherent digital in-line holography, which is capable of directly imaging micro- and nano-particles within field-portable designs (e.g., compact stand-alone units and cell-phone hardware attachments), providing a highly-sensitive and high-throughput toolset for rapid medical diagnostics and screening especially for resource-limited regions of the world. This computational microscopy and nano-particle imaging platform

achieves subcellular spatial resolution and also directly images, for the first time in on-chip microscopy, single sub-100 nm particles using self-assembled aspheric liquid nano-lenses around individual nano-particles across a large field-of-view of $>20 \text{ mm}^2$, i.e., more than two orders-of-magnitude larger than existing nano-imaging techniques.

Chapter 2 Lensfree Partially-Coherent In-Line Holographic

Imaging

2.1 Introduction

In this chapter, I will describe the lensfree partially-coherent in-line holography that constitutes the underlying mechanism and theory of lensfree wide-field optical imaging of single nano-particles on a chip.

Lensfree holography provides $\sim 1\text{-}1.5\ \mu\text{m}$ spatial resolution (sufficient to image e.g., sub-cellular features) over a large field of view (FOV) of $>24\ \text{mm}^2$, which constitutes more than ~ 10 fold improvement compared to a typical 10X objective-lens FOV. This holographic imaging modality does not utilize any lenses, lasers or other bulky optical/mechanical components which can greatly simplify its architecture making it compact, light-weight, and cost-effective (see Fig. 2.1). Instead of using a coherent source (e.g., a laser) as one would normally find in conventional holography approaches, a simple light-emitting-diode (LED) is utilized for illumination which suppresses the coherent speckle noise and the undesired multiple-reflection interference effects on the detected holograms. This incoherent LED light is initially filtered by passing it through a large aperture of $\sim 50\text{-}100\ \mu\text{m}$ diameter, which also eliminates the need for any coupling and focusing optics/mechanics between the LED and the aperture plane (Fig. 2.1). This large aperture size also makes it robust to mechanical misalignments or potential clogging problems, making it highly suitable for use in the field by minimally trained personnel. The filtered LED light, after propagating in air a distance (z_1) of e.g., $\sim 3\text{-}10\ \text{cm}$, interacts with the object of interest (e.g., a whole blood sample) that is located on the top of the optoelectronic imaging detector ($z_2 = \sim 0.3\text{-}1\ \text{mm}$). Each object (e.g., blood cells) within the sample scatters, absorbs and refracts the

incoming light based on its size, 3D morphology, sub-cellular elements, and refractive index. The interference of the light waves that passed through the cells (objects) with the unscattered LED light creates the hologram of each cell (with unit fringe magnification), which is detected without any lenses using a CMOS (complementary metal-oxide semiconductor) sensor array or a CCD (charge-coupled device) (Fig. 2.1). The digital hologram of each cell (or object) is extremely rich (despite the use of a simple LED through a large aperture and a unit fringe magnification) and permits rapid reconstruction of its optical phase (which was lost during the recording process) as well as its microscopic (amplitude) image.

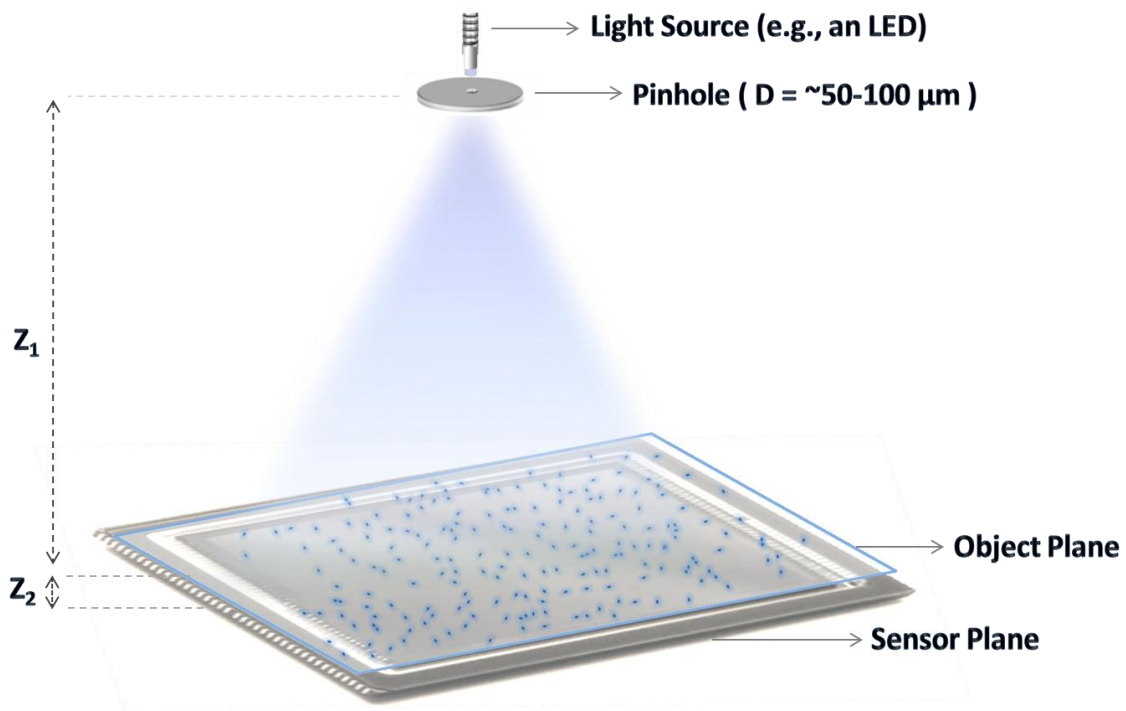


Figure 2.1 Schematic diagram of lensfree holographic microscopy set-up (not drawn to scale). The aperture to sample plane distance ($z_1 = \sim 3\text{-}10\text{ cm}$) is much larger than the sample to sensor plane distance ($z_2 = \sim 0.3\text{-}1\text{ mm}$). A partially coherent light source (e.g., an LED) is utilized for illumination, emanating from a large aperture ($D = \sim 50\text{-}100\ \mu\text{m}$). Samples of interest are directly placed onto the CMOS sensor-chip that records holograms of individual particles over a field of view of 24 mm^2 .

2.2 Theoretical Analysis of Digital Lensfree In-Line Holographic Imaging

Holography is all about recording the optical phase information in the form of amplitude oscillations. To be able to read or make use of this phase information for microscopy and imaging, most existing lensfree in-line holography systems are hungry for spatial coherence and therefore use a laser source that is filtered through a small aperture (e.g., 1-2 μm). Utilizing a completely incoherent light source that is filtered through a large aperture (e.g., $\sim 50\text{-}100$ μm in diameter) should provide orders-of-magnitude better transmission throughput as well as a much simpler, inexpensive and more robust optical set-up. Here I aim to provide a theoretical analysis of this opportunity and its implications for compact and cost-effective lensfree holographic microscopy.

To record lensfree holograms of individual particles (e.g., cells) that contain useful digital information with a spatially incoherent source emanating from a large aperture, one of the key steps is to bring the object plane close to the detector array by ensuring $z_2 \ll z_1$, where z_1 defines the distance between the incoherently illuminated aperture plane and the object (cell) plane, and z_2 defines the distance between the cell plane and the sensor array (see Fig. 2.1). In conventional lensless in-line holography approaches, this choice is reversed such that $z_1 \ll z_2$ is utilized, while the total aperture-to-detector distance ($z_1 + z_2$) remains comparable in both cases, leaving the overall device length almost unchanged. Therefore, apart from using an incoherent source through a large aperture, my choice of $z_2 \ll z_1$ is also quite different from the main stream lensfree holographic imaging approaches and thus deserves more attention.

To better understand the quantified impact of this choice on incoherent on-chip microscopy, let me assume two point scatterers (separated by $2a$) that are located at the cell plane ($z = z_1$) with a field transmission of the form $t(x, y) = 1 + c_1 \delta(x - a, y) + c_2 \delta(x + a, y)$ where c_1

and c_2 can be negative and their intensity denotes the strength of the scattering process, and $\delta(x,y)$ defines a Dirac-delta function in space. These point scatterers can be considered to represent sub-cellular elements that make up the cell volume. For the same imaging system let me assume that a large aperture of arbitrary shape is positioned at $z=0$ with a transmission function of $p(x,y)$ and that the digital recording screen (e.g., a CCD or a CMOS array) is positioned at $z= z_1 + z_2$, where typically $z_1 \sim 3-10$ cm and $z_2 \sim 0.3-1$ mm.

Assuming that the aperture $p(x,y)$ is uniformly illuminated with a spatially incoherent light source, the cross-spectral density at the aperture plane can be written as:

$$W(x_1, y_1, x_2, y_2, \gamma) = S(\gamma) p(x_1, y_1) \delta(x_1 - x_2) \delta(y_1 - y_2),$$

where (x_1, y_1) and (x_2, y_2) represents two arbitrary points on the aperture plane and $S(\gamma)$ denotes the power spectrum of the incoherent source with a center wavelength (frequency) of λ_0 (γ_0).

It should be noted that in this experimental scheme (Fig. 2.1), the incoherent light source (the LED) was butt-coupled to the pinhole with a small amount of unavoidable distance between its active area and the pinhole plane. This remaining small distance between the source and the pinhole plane also generates some correlation for the input field at the aperture plane. In this theoretical analysis, I ignore this effect and investigate the imaging behavior of a completely incoherent field hitting the aperture plane. The impact of such an unavoidable gap between pinhole and the incoherent source is an “effective” reduction of the pinhole size in terms of spatial coherence (without affecting the light throughput), which I will not consider in this analysis.

Based on these assumptions, after free space propagation over a distance of z_1 , the cross-spectral density just before interacting with the cells can be written as:⁵³

$$W(\Delta x, \Delta y, q, \gamma) = \frac{S(\gamma)}{(\lambda z_1)^2} e^{-j\frac{2\pi y q}{c z_1}} \iint p(x, y) e^{j\frac{2\pi}{\lambda z_1}(x\Delta x + y\Delta y)} dx dy$$

where $\Delta x = x'_1 - x'_2$, $\Delta y = y'_1 - y'_2$, $q = \frac{x'_1+x'_2}{2} \Delta x + \frac{y'_1+y'_2}{2} \Delta y$; and (x'_1, y'_1) (x'_2, y'_2) represent two arbitrary points on the cell plane. After interacting with the cells i.e., with $t(x, y)$, the cross-spectral density, right behind the cell plane, can be written as:

$$W(\Delta x, \Delta y, q, \gamma) \cdot t^*(x'_1, y'_1) \cdot t(x'_2, y'_2)$$

This cross-spectral density function will effectively propagate another distance of z_2 before reaching the detector plane. Therefore, one can write the cross-spectral density at the detector plane as:

$$W_D(x_{D1}, y_{D1}, x_{D2}, y_{D2}, \gamma) = \iint \iint h_C^*(x'_1, x_{D1}, y'_1, y_{D1}, \gamma) h_C(x'_2, x_{D2}, y'_2, y_{D2}, \gamma) W(\Delta x, \Delta y, q, \gamma) t^*(x'_1, y'_1) t(x'_2, y'_2) dx'_1 dy'_1 dx'_2 dy'_2$$

where (x_{D1}, y_{D1}) and (x_{D2}, y_{D2}) define arbitrary points on the detector plane (i.e., within the hologram region of each cell); and

$$h_C(x', x_D, y', y_D, \gamma) = \frac{1}{j\lambda z_2} e^{j\frac{2\pi z_2}{\lambda}} e^{j\frac{\pi}{\lambda z_2}[(x'-x_D)^2+(y'-y_D)^2]}.$$

At the detector plane (x_D, y_D) , the optical intensity $i(x_D, y_D)$ can then be written as:

$$i(x_D, y_D) = \int W_D(x_D, y_D, x_D, y_D, \gamma) d\gamma$$

Assuming $t(x, y) = 1 + c_1\delta(x - a, y) + c_2\delta(x + a, y)$, this last equation can be expanded into 4 physical terms, i.e.,

$$i(x_D, y_D) = C(x_D, y_D) + I(x_D, y_D) + H_1(x_D, y_D) + H_2(x_D, y_D),$$

where:

$$C(x_D, y_D) = D_0 + \frac{|c_1|^2 S_0}{(\lambda_0 z_1 z_2)^2} \tilde{P}(0, 0) + \frac{|c_2|^2 S_0}{(\lambda_0 z_1 z_2)^2} \tilde{P}(0, 0) \quad (1)$$

$$I(x_D, y_D) = \frac{c_2 c_1^* S_0}{(\lambda_0 z_1 z_2)^2} \tilde{P}\left(\frac{2a}{\lambda_0 z_1}, 0\right) e^{j\frac{4\pi a x_D}{\lambda_0 z_2}} + c. c. \quad (2)$$

$$H_1(x_D, y_D) = \frac{S_0}{(\lambda_0 z_1)^2} [c_1 \cdot \{p(-x_D \cdot M + a \cdot M \cdot F, -y_D \cdot M) * h_c(x_D, y_D)\} + c. c.] \quad (3)$$

$$H_2(x_D, y_D) = \frac{S_0}{(\lambda_0 z_1)^2} [c_2 \cdot \{p(-x_D \cdot M - a \cdot M \cdot F, -y_D \cdot M) * h_c(x_D, y_D)\} + c. c.] \quad (4)$$

In these Equations “c.c.” and “*” refer to the complex conjugate and convolution operations, respectively, $M = \frac{z_1}{z_2}$, $F = \frac{z_1 + z_2}{z_1}$, and \tilde{P} is the 2D spatial fourier transform of the aperture function $p(x, y)$. It should be emphasized that (x_D, y_D) in these equations refers to the cell hologram extent, not to the entire field-of-view of the detector array.

Further, $h_c(x_D, y_D) = \frac{1}{j \lambda_0 \cdot F \cdot z_2} e^{j \frac{\pi}{\lambda_0 \cdot F \cdot z_2} (x_D^2 + y_D^2)}$ which effectively represents the 2D coherent impulse response of free space over $\Delta z = F \cdot z_2$. For the incoherent source, a center frequency (wavelength) of γ_0 (λ_0) has been assumed, where the spectral bandwidth was assumed to be much smaller than λ_0 with a power spectrum of $S(\gamma) \cong S_0 \delta(\gamma - \gamma_0)$.

Note that in these derivations I have also assumed paraxial approximation to simplify the results, which is a valid assumption since for this work z_1 and z_2 are typically much longer than the extend of each cell hologram (L_H). However for the digital microscopic reconstruction of the cell images from their raw holograms, no such assumptions were made as also emphasized in the next section.

Furthermore, D_0 of Eq. 1 can further be expanded as:

$$D_0 = \iiint \int \frac{W(\Delta x, \Delta y, q, \gamma)}{(\lambda z_2)^2} e^{-j \frac{\pi}{\lambda z_2} [(x'_1 - x_D)^2 + (y'_1 - y_D)^2]} e^{j \frac{\pi}{\lambda z_2} [(x'_2 - x_D)^2 + (y'_2 - y_D)^2]} dx'_1 dy'_1 dx'_2 dy'_2 d\gamma$$

which simply represents the background illumination and has no spatial information regarding the cells' structure or distribution. Although this last term, D_0 can further be simplified, for most

illumination schemes it constitutes a uniform background and therefore can be easily subtracted out.

Equations (1-4) are rather important to understand the key parameters in lensfree on-chip microscopy with spatially incoherent light emanating from a large aperture. Equation 1 describes the classical diffraction that occurs from the cell plane to the detector under the paraxial approximation. In other words, it includes both the background illumination (D_0) and also the self-interference of the scattered waves (terms that are proportional to $|c_1|^2$ and $|c_2|^2$). It is quite intuitive that the self-interference terms representing the classical diffraction in Eq. (1) are scaled with $\tilde{P}(0,0)$ as the extent of the spatial coherence at the cell plane is not a determining factor for self-interference.

Equation 2, however, contains the information of the interference between the scatterers located at the cell plane. Similar to the self-interference term, the cross-interference term, $I(x_D, y_D)$, also does not contain any useful information as far as holographic reconstruction of the cell image is concerned. This interference term is proportional to the amplitude of $\tilde{P}\left(\frac{2a}{\lambda_0 z_1}, 0\right)$, which implies that for a small aperture size (hence wide \tilde{P}) two scatterers that are located far from each other can also interfere. Based on the term $\tilde{P}\left(\frac{2a}{\lambda_0 z_1}, 0\right)$, one can estimate that if $2a < \frac{\lambda_0 z_1}{D}$ (where D is roughly the aperture width) the scattered fields can quite effectively interfere at the detector plane giving rise to the interference term $I(x_D, y_D)$. This result is not entirely surprising since the coherence diameter at the cell plane is proportional to $\frac{\lambda_0 z_1}{D}$, as also predicted by the van Cittert-Zernike theorem. It is another advantage of the incoherent holography approach presented here that the cross-interference term, $I(x_D, y_D)$, will only contain the contributions of a limited number of cells within the imaging field-of-view since $\tilde{P}\left(\frac{2a}{\lambda_0 z_1}, 0\right)$

will rapidly decay to zero for a large aperture. This cross-interference term will be stronger for coherent in-line holography due to much better spatial coherence. This difference can especially make an impact in favor of incoherent large aperture illumination for imaging of a dense cell solution such as whole blood samples where $I(x_D, y_D)$ can no longer be ignored.

The final two terms (Eqs. (3-4)) describe the holographic diffraction phenomenon and they are of central interest in all forms of digital holographic imaging systems, including the one presented here. Physically these terms dominate the information content of the detected intensity, especially for weakly scattering objects, and they represent the interference of the scattered light from each object with the background light, i.e., $H_1(x_D, y_D)$ represents the holographic diffraction of the first scatterer $c_1 \delta(x - a, y)$, whereas $H_2(x_D, y_D)$ represents the holographic diffraction of the second scatterer, $c_2 \delta(x + a, y)$. Note that the complex conjugate (c.c.) terms in Eqs. 3 and 4 represent the source of the twin images of the scatterers since $h_c^*(x_D, y_D)$ implies propagation in the reverse direction creating the twin image artifact at the reconstruction plane. Elimination of such twin images during digital holographic reconstruction process is discussed in the next section.

The terms inside the curly brackets of Eqs. (3-4) indicates that, for each scatterer position, a scaled and shifted version of the aperture function $p(x, y)$ appears to be coherently diffracting with the free space impulse response $h_c(x_D, y_D)$. In other words, as far as holographic diffraction is concerned, each point scatterer at the cell plane can be replaced by a scaled version of the aperture function (i.e., $p(-x_D \cdot M, -y_D \cdot M)$) that is shifted by F fold from origin, and the distance between the cell plane and the sensor plane can now be effectively replaced by $\Delta z = F \cdot z_2$. Quite importantly this scaling factor is $M = \frac{z_1}{z_2}$, which implies that the large aperture size that is illuminated incoherently is effectively narrowed down by M fold at the cell plane (typically

$M \approx 40-100$). Therefore, for $M \gg 1$, incoherent illumination through a large aperture is approximately equivalent (for each cell's holographic signature) to coherent illumination of each cell individually, where the wave propagation over Δz determines the detected holographic intensity of each cell. This is valid as long as the cell's diameter is smaller than the coherence diameter ($D_{\text{coh}} \sim \frac{\lambda_0 z_1}{D}$, see Eq. 2) at the object (cell) plane, where D defines the width of the illumination aperture and typically $D_{\text{coh}} \sim 400\lambda_0 - 1000\lambda_0$, which is quite appropriate for most cells (objects) of interest. Accordingly, for a completely incoherent source and a sensor area of A , $d=D/M$ defines the effective width of each point scatterer on the cell plane and $f = A/F^2$ determines the effective imaging field-of-view. Assuming some typical numbers for z_1 (~ 4 cm) and z_2 (~ 0.8 mm), the scaling factor (M) becomes ~ 50 with $F \approx 1$, which means that even a $D=50 \mu\text{m}$ wide pinhole would be scaled down to $\sim 1 \mu\text{m}$ at the cell plane, which can now quite efficiently be mapped to the entire active area of the sensor array, i.e., $f \approx A$. To conclude: for $M \gg 1$ the spatial features of the cells over the entire active area of the sensor array will not be affected by the large incoherent aperture, which permits recording of coherent hologram of each cell (object) individually.

Even though the entire derivation above was made using the formalism of wave theory, the end result is quite interesting as it predicts a geometrical scaling factor of $M = z_1/z_2$. Further, because $M \gg 1$, each cell hologram only occupies a tiny fraction of the entire field-of-view and therefore behaves independent of most other cells within the imaging field-of-view. That is the same reason why (unlike conventional lensfree in-line holography) there is no longer a Fourier transform relationship between the detector plane and the cell plane. Such a Fourier transform relationship only exists between each cell hologram and the corresponding cell.

Notice also that in Eqs. (3-4) the shift of the scaled aperture function $p(-x_D \cdot M \mp a \cdot M \cdot F, -y_D \cdot M)$ from origin can be written as $x_D = \mp a \cdot F$, which is in perfect agreement with the choice of the word “fringe magnification factor” to describe the function of $F = \frac{z_1+z_2}{z_1}$ for the holographic diffraction term. This also explains the reduction in the imaging field-of-view by F^2 fold for in-line digital holography. Assuming $M \gg 1$, Δz approaches to z_2 and the shift terms in Eqs. (3-4), i.e., $\mp a \cdot F$ also approach to $\mp a$, which makes sense since it corresponds to the shift of the scatterers at the cell plane from origin.

According to Eqs. (3-4), for a narrow enough $p(-x_D \cdot M, -y_D \cdot M)$ (such that the spatial features of the cells are not washed out), the modulation of the holographic term at the detector plane can be expressed as $\sin\left(\frac{\pi}{\lambda_0 F z_2}(x_D^2 + y_D^2)\right)$. This modulation term of the holographic signature at the detector plane implies that for a large fringe magnification (F), the pixel size of the sensor array will have an easier time to record the rapidly oscillating fringes of the cell hologram, which effectively increases the numerical aperture of the sampling as much as the sensor width permits. However, there are penalties to be paid for this large F choice: (1) a large F does not permit the use of an incoherent source emanating through a large aperture, which makes it more demanding on the optics and alignment, also increasing the relative cost and complexity; and (2) the effective imaging field-of-view is also reduced by factor proportional to F^2 .

The derivation discussed above was made for 2 point scatterers separated by $2a$, such that $c_1\delta(x - a, y) + c_2\delta(x + a, y)$. The more general form of the incoherent holographic term (equivalent of Eqs. 3 and 4 for a continuous distribution of scatterers - as in a real cell) can be expressed as:

$$H(x_D, y_D) \propto \frac{S_0}{(\lambda_0 z_1)^2} \cdot \left(\frac{z_2}{z_1}\right)^2 \left[\left\{ s\left(\frac{x_D}{F}, \frac{y_D}{F}\right) * h_c(x_D, y_D) \right\} + \text{c. c.} \right]$$

where $s(x_D, y_D)$ refers to the transmission image of the sample/cell of interest, which represents the 2D map of all the scatterers located within the sample/cell volume. The above derivation assumed a narrow enough $p(-x_D/M, -y_D/M)$ such that $M \gg 1$, which is characteristic of the approach discussed in this manuscript. The physical effect of the fringe magnification factor (F) on the object hologram can also be visualized in this final equation, in harmony with the discussions in the previous paragraphs.

2.3 Image Reconstruction in Digital Lensfree In-Line Holographic Imaging

The use of incoherent illumination through a large aperture brings numerous advantages to on-chip microscopy, making it a highly suitable and promising platform cell biology and medical diagnostics in resource limited settings. Despite significant practical advantages of the lensfree holographic microscopy and imaging, it may mislead the reader that incoherent illumination will increase the burden on the numerical reconstruction process. Nevertheless, for incoherent lensfree holography with $M = z_1/z_2 \gg 1$, each individual cell can still be treated to be illuminated with a coherent light. Further, due to their microscopic cross-sections, the incident wave on each cell can be assumed to be a plane wave. Consequently, the reconstruction of each recorded cell hologram can be performed assuming plane-wave illumination.

In order to diffract the wavefronts, the angular spectrum approach is used to numerically solve the Rayleigh-Sommerfeld integral. This computation involves multiplying the Fourier transform of the field with the transfer function of propagation through linear, isotropic media, as shown below:

$$H_z(f_x, f_y) = \begin{cases} \exp\left(j2\pi z \frac{n}{\lambda}\right) \sqrt{1 - (\lambda f_x/n)^2 - (\lambda f_y/n)^2}, & \sqrt{f_x^2 + f_y^2} < \frac{n}{\lambda} \\ 0, & \text{otherwise} \end{cases}$$

where f_x and f_y are the spatial frequencies and n is the refractive index of the medium. It should be noted that no paraxial approximations are made in image reconstructions.

Two different iterative approaches are taken in order to reconstruct the microscopic images of cells, free from any twin-image artifact. Both methods work with a single recorded hologram and rely on the constraint that each cell has a finite support. In both methods, the raw holograms are upsampled typically by a factor of four to six, using cubic spline interpolation before the iterative reconstruction procedure. Although upsampling does not immediately increase the information content of the holograms, it still offers significant improvements for achieving a more accurate phase recovery and higher resolution in the reconstructed image. First, it allows defining a more accurate object support by smoothing the edges of the objects in the initial back-projection of the hologram. Using an object support that is closer to the actual cell in terms of size and shape reduces the error of the iterative algorithms, as well as ensuring faster convergence. Second, upsampling introduces higher spatial frequencies initially carrying zero energy, in the hologram. Through the iterative reconstruction steps detailed below, these higher spatial frequencies gradually attain non-zero energy, which allows sub-cellular spatial resolution in the final reconstruction.

Lensfree Holographic Image Reconstruction Method 1

The first method falls under the broad category of Interferometric Phase-Retrieval Techniques and is applicable to cases where the recorded intensity is dominated by the holographic diffraction terms.⁵⁹⁻⁶¹ The first step is the digital reconstruction of the hologram,

which is achieved by propagating the hologram intensity by a distance of z_2 away from the hologram plane yielding the initial wavefront U_{rec} . As a result of this computation, the virtual image of the object is recovered together with its spatially overlapping defocused twin-image. It is important to note that the recorded intensity can also be propagated by a distance of $-z_2$. In this case, the real image of the object can be recovered, while the defocused virtual image leads to the twin-image formation.

Due to the small cell-sensor distance in the incoherent holographic microscopy scheme presented here, the twin-image may carry high intensities, especially for relatively large objects like white blood cells. In such cases, the fine details inside the micro-objects may get suppressed. Similarly, the twin-images of different cells which are close to each other get superposed, leading to an increase in background noise. This issue is especially pronounced for holographic microscopy of dense cell solutions, where the overlapping twin images of many cells lowers the counting accuracy due to reduced SNR.

In order to eliminate the twin-image artifact, an iterative approach using finite support constraints⁶¹ is utilized. Basically, this technique⁶¹ relies on the fact that duplicate information for the phase and amplitude of the object exists in two different reconstruction planes at distances $+z_2$ and $-z_2$ from the hologram plane, where the virtual and real images of the object are recovered, respectively. Therefore, a twin-image-free reconstruction in one of the image planes can be obtained, while filtering out the duplicate image in the other plane. Without loss of generality, I have chosen to filter out the real image to obtain a twin-image-free reconstruction in the virtual image plane at $-z_2$. Due to the finite size of the micro-objects, the real image of the object only occupies the region inside its support, while the defocused twin-image image spreads out to a wider region around the object, also

overlapping with the real image inside the support. Hence, deleting the information only inside the support ensures that the real image is completely removed from the reconstructed wavefront. Nevertheless, the virtual image information inside the support is also lost, and the iterative technique tries to recover the missing information of the virtual image by going back and forth between the virtual and real image planes, recovering more of the lost information at each iteration. The success of this algorithm is highly dependent on the Fresnel number of the recording geometry, which is given by $N_f = n(\text{object size})^2/(\lambda z)$. It is reported that the technique⁶¹ proves successful for Fresnel numbers as high as 10. For RBCs of approximately 7 μm diameter, the typical recording geometries presented here involve Fresnel numbers of <0.2 ; hence, the twin-image elimination method yields highly satisfactory results.

The steps of twin-image elimination are detailed below:

(a) Initially the real image, which is the back-projected hologram at a distance of $+z_2$, is used for determining the object support. Object support can be defined by either thresholding the intensity of the reconstructed image, or searching for its local minima.

(b) The region inside the support is deleted and a constant value is assigned to this region as an initial guess for the deleted part of the virtual image inside the support as shown below:

$$U_{z_2}^{(i)}(x,y) = \begin{cases} U_{\text{rec}} , & x,y \notin S \\ \bar{U}_{\text{rec}} , & x,y \in S \end{cases}$$

where $U_z^{(i)}(x,y)$ denotes the field at the real image plane after the i^{th} iteration. S represents the area defined by the object support, and \bar{U}_{rec} is the mean value of U_{rec} within the support.

(c) Then, the field at the real image plane is back propagated by $-2z_2$ to the virtual image plane. Ideally, the reconstruction at this plane should be free from any twin-image

distortions. Therefore, the region outside the support can be set to a constant background value to eliminate any remaining out-of-focus real image in the virtual image plane. However, this constraint is applied smoothly as determined by the relaxation parameter β below, rather than sharply setting the image to dc level outside the support:

$$U_{-z_2}^{(i)}(x, y) = \begin{cases} D - \frac{D - U_{-z_2}^{(i)}}{\beta}, & x, y \notin S \\ U_{-z_2}^{(i)}, & x, y \in S \end{cases}$$

where D is the background in the reconstructed field, which can either be obtained from a measured background image in the absence of the object, or can simply be chosen as the mean value of the field outside the object supports at the virtual image plane. β is a real valued parameter greater than unity, and is typically chosen around 2-3 here. Increasing β leads to faster convergence, but compromises the immunity of the iterative estimation accuracy to background noise.

(d) The field at the virtual image plane is forward propagated to the real-image plane, where the region inside the support now has a better estimate of the missing part of the virtual image. The region outside the support can be replaced by $U_{z_2}^{(1)}(x, y)$, the original reconstructed field at the real image plane, as shown below:

$$U_{z_2}^{(i+1)}(x, y) = \begin{cases} U_{z_2}^{(1)}, & x, y \notin S \\ U_{z_2}^{(i+1)}, & x, y \in S \end{cases}$$

Steps c to d can be repeated iteratively until the final image converges. In most cases, convergence is achieved after 10-15 iterations. This iterative computation takes around 4 seconds for an image size of ~5 Mpixels using a regular CPU (central processing unit – e.g., Intel Q8300) and it gets >40X faster using a GPU (graphics processing unit – e.g., NVIDIA GeForce GTX 285) achieving <0.1 sec computation time for the same image size.

Lensfree Holographic Image Reconstruction Method 2

The second method utilized for eliminating the twin-image is classified under Non-Interferometric Phase-Retrieval Techniques,⁶² where the recorded image is not necessarily treated as a hologram, but as the intensity of any diffraction field. Together with the constraint that the objects have finite support, this technique is capable of iteratively recovering the phase of the diffracted field incident on the detector from a single intensity image. As a result, the complex field (amplitude and phase) of the holograms, rather than the intensity, can be back-propagated, thereby allowing reconstruction of the objects free from any twin-image contamination. This method can be decomposed into the following steps:

(a) The square-root of the recorded hologram intensity is propagated by a distance of $-z_2$ to the cell plane, assuming a field phase of zero as an initial guess. The aim of the algorithm is to iteratively determine the actual phase of the complex field at the detector plane, and eventually at the object plane. In the first iteration, the object support is defined either by thresholding the intensity of the field at the object plane, or by locating its regional maxima and/or minima.

(b) The field inside the object supports is preserved, while the complex field values outside the supports is replaced by a background value $D_{-z_2}(x,y)$, as shown below:

$$U_{-z_2}^{i+1}(x,y) = \begin{cases} m \cdot D_{-z_2}(x,y), & x,y \notin S \\ U_{-z_2}^i(x,y), & x,y \in S \end{cases}$$

where $D_{-z_2}(x,y)$ is obtained by propagating the square root of the background intensity (amplitude) of the image obtained by the same setup in the absence of the cells (objects); and $m = \text{mean}(U_{-z_2}^i(x,y))/\text{mean}(D_{-z_2}(x,y))$.

(c) The modified field at the object plane is propagated back to the detector plane, where the field now has a non-zero phase value. The amplitude of this field is replaced with

the square root of the original recorded hologram intensity as no modification for the amplitude should be allowed while converging for its phase. Consequently, $U_0^{(i)}(x,y)$, the complex diffraction field at the detector plane after the i^{th} iteration can be written as follows:

$$U_0^{(i)}(x,y) = \left| U_0^{(0)}(x,y) \right| \cdot \exp(j \cdot \phi_0^{(i)}(x,y))$$

where the superscripts denote the iteration step, and $\phi_0^{(i)}(x,y)$ denotes the phase of the field after the i^{th} iteration. Steps a to c can be iterated until the phase recovery converges. Typically, the results are obtained with less than 15 iterations, which is quite similar to the first Method above.

For small or weakly scattering objects such as whole blood cells or micro-beads, both reconstruction methods yield satisfactory results of comparable image quality. For such objects, the typical Fresnel number of the recording geometry is <1 and the focused real image occupies a small fraction of the area over which the twin-image is spread out. Therefore, deleting the object image in the real image plane leads to minimal information loss for the virtual image, which is to be recovered without twin-image artifacts. However, for larger objects of interest the Fresnel number of the system increases, and deleting the real image may cause excessive information loss in the virtual image, which may be harder to recover iteratively. Furthermore, for strongly scattering objects, the self and cross-interference terms may start dominating such that the holographic content of the recorded intensity gets distorted. Therefore for strongly scattering and/or extended objects, the second method discussed above becomes more preferable over the first method, which requires the holographic terms to be dominant in a setup with Fresnel numbers <10 . However, an advantage of the first method is that it does not necessarily require a separate background image taken prior to inserting the sample into the setup. Although a mean value of the field

at the object plane can also be used, in the absence of a background image for method 2 (step b), it has been observed that the final image quality becomes better with an experimentally obtained background.

2.4 Discussions

The use of an incoherent light source emanating through a large aperture (e.g., 50-100 μm) greatly simplifies the optics for lensfree on-chip microscopy also making it more robust and cost-effective both of which are highly desired qualities for resource poor environments. Bringing the object plane much closer to the sensor surface together with a fringe magnification of $F \sim 1$ is one of the key steps in making lensfree holographic imaging possible with a large incoherent source without smearing the spatial information of the cells. This choice also brings a significant increase in the FOV and throughput of this imaging modality. However, when compared to the state of the art in lensless holography, there is some trade-offs to be made in return for these improvements that are addressed below in this section.

The advantages of a small cell-sensor distance and unit fringe magnification in incoherent lensfree holography can be listed as follows:

i) The size of the aperture, its exact shape and alignment with respect to the light source is much less of a concern. This makes it orders-of-magnitude more power efficient, easier to align and operate without the use of a laser or any coupling/focusing optics. This is highly important for global health applications, which demand robust, cost-effective, compact and easy-to-use devices for microscopy and medical diagnostics.

ii) A small cell-sensor distance enables imaging of individual holograms (both phase and amplitude), which I treat as fingerprint signatures of cells based on their size, shape,

intracellular elements, refractive index etc. This holographic signature/texture (which is now also free from speckle noise⁶³ of a coherent source) is a powerful tool that can enable diagnostic decisions to be made without any reconstruction by using pattern matching algorithms that compare cell hologram libraries to measured hologram textures. This can reduce computation time significantly since digital pattern analysis & matching is the common required step for most automated cytometry & diagnostic platforms, i.e., the entire digital computation can be made much simpler and faster.

iii) The presented approach also significantly improves the imaging FOV as illustrated with experimental results in next chapters.

iv) By the use of a small z_2 , the collection numerical aperture (NA) at the detection plane approaches to the medium refractive index, n . For larger z_2 values (as in conventional in-line holography), the sensor array width starts to define the collection NA, which reduces the effective light collection efficiency of the system.

This last point requires more discussion since the improved light collection efficiency does not necessarily imply a better resolution as the sampling period at the hologram plane (i.e., the pixel size, Δx_D) is also quite important. To summarize the conclusions: the detection numerical aperture for a small cell-sensor distance is significantly improved which increases the light collection efficiency; however, not all the collected light contributes to the holographic texture. It turns out that the price that is paid for simplification of the optical system towards achieving lensfree cell holography with a large incoherent source over a large field-of-view is an increased need for a smaller pixel size to be able to record all the hologram fringes that are above the detection noise floor to claim a high NA for better lateral and axial resolution.

Imaging field-of-view of this platform is equivalent to direct near-field (i.e., contact) imaging of the object plane due to the fringe magnification of ~ 1 , such that it has the entire sensor area available as its field of view. However, achieving sub-pixel ($< \sim 2.2 \mu\text{m}$) resolution implies that the presented lensfree incoherent holography technique achieves much better performance than direct contact imaging, without a trade-off in any image metric, such as field of view, signal to noise ratio, phase contrast, etc. In other words, undoing the effect of diffraction through digital holographic processing (even with unit magnification and incoherent LED illumination) performs much better than an hypothetical near-field sampling experiment where a sensor-array having the same pixel size directly images the object plane all in parallel (i.e., without diffraction).

Another significant advantage of lensfree holographic imaging over direct near-field sampling (i.e., contact imaging) would be the capability of phase imaging. Any phase-only object would not create a detectable contrast in direct near-field sampling on the sensor-array, whereas the presented lensfree incoherent holography approach would naturally pick up the diffraction oscillations that contain the phase information of the samples located over the entire sensor area.

The key for sub-pixel spatial resolution in lensfree incoherent holographic microscopy is hidden in the iterative recovery techniques, where a digitally identified object support is enforced at each iteration to recover the lost phase of the hologram texture. This object support can be made appropriately tighter if a priori information about the object type and size is known – for instance if the cells of interest are known to be human blood cells, a tighter object support (with dimensions of $< 15 \mu\text{m}$) can be utilized for faster convergence of the phase recovery process. Intuitively, this behavior can be explained by a reduction in the

number of unknown pixels in the phase recovery step, which enables iterative convergence to the unique solution, among many other possibilities, based on the measured hologram intensity and the estimated object support. Sub-pixel resolution is therefore coupled to iterative use of this object support for estimation of higher spatial frequencies of the object plane.

Like any other frequency extrapolation method, the practical success of this iterative approach and the spatial resolution of this system also depend on the SNR, which is a strong function of the cell/object size (i.e., its scattering cross section). For deeply submicron sized cells ($<0.1 \mu\text{m}$), the scattering is rather weak, which implies that the high spatial frequencies (close to n/λ_0) carry rather weak energies that can easily fall below the noise floor at the sensor. Therefore, the true resolution and the NA of digital reconstruction indeed depend on the SNR as well as the scattering cross section of the cells/objects, making deeply sub-micron cell imaging challenging for this reason.

Chapter 3 Compact, Light-weight and Cost-effective Lensfree

Microscopy

3.1 Introduction

Recent progress in optical imaging and microscopy architectures has been expanding our horizon and increasing the opportunities in medical diagnostics. Although we experience significant advancements¹⁻³⁰ such as better resolution, speed and throughput, novel platforms are still bulky and expensive as discussed in detail in the Chapter 1, their function beyond well-established clinical environment is quite limited. Furthermore, microscopy applications occupy the center of attraction in medical diagnostics and prevalence of innovative imaging techniques is necessary to combat global health problems in resource scarce settings where health care infrastructure is extremely limited or does not even exist. In such poor settings, imaging devices should be portable, robust, cost-effective and ideally integrated with telemedicine networks that connect end-users to a central medical establishment (e.g., a hospital or a laboratory).

In the meantime, telemedicine applications offer numerous opportunities to improve the quality of public health care and decrease costs by enabling rapid evaluation of human well-being. In this evolution of health care delivery, massive growth in wireless communication networks stands for a milestone such that mobile and light-weight telemedicine devices can be used for more cost-effective and user-friendly health care services. On the other hand, majority of the world population own at least one cell-phone today and the number of mobile subscribers is expected to be increasing in the near future.³²⁻³⁴ Utilizing the fascinating features of this advanced state-of-the-art cell-phone technology towards medical diagnostics can complement the current stage of telemedicine and wireless health.

Centered on this vision, I have successfully implemented lensfree partially-coherent in-line holography (that has been described in detail in the Chapter 2) on a portable and mechanically robust stand-alone unit³⁷ which weighs only ~46 grams with dimensions smaller than 4.2x4.2x5.8cm (Fig. 3.1(a)) as well as on a commercially-available cell-phone³² that is modified with a light-weight (~ 38 grams) hardware attachment (Fig. 3.1(b)). Offering significant advantages over conventional holographic imaging modalities in terms of the use of optical components and the operation principle as discussed in Chapter 2, lensfree holography permits the miniaturization of the technology towards such compact, light-weight and cost-effective microscopes for telemedicine applications that I will describe in this chapter.

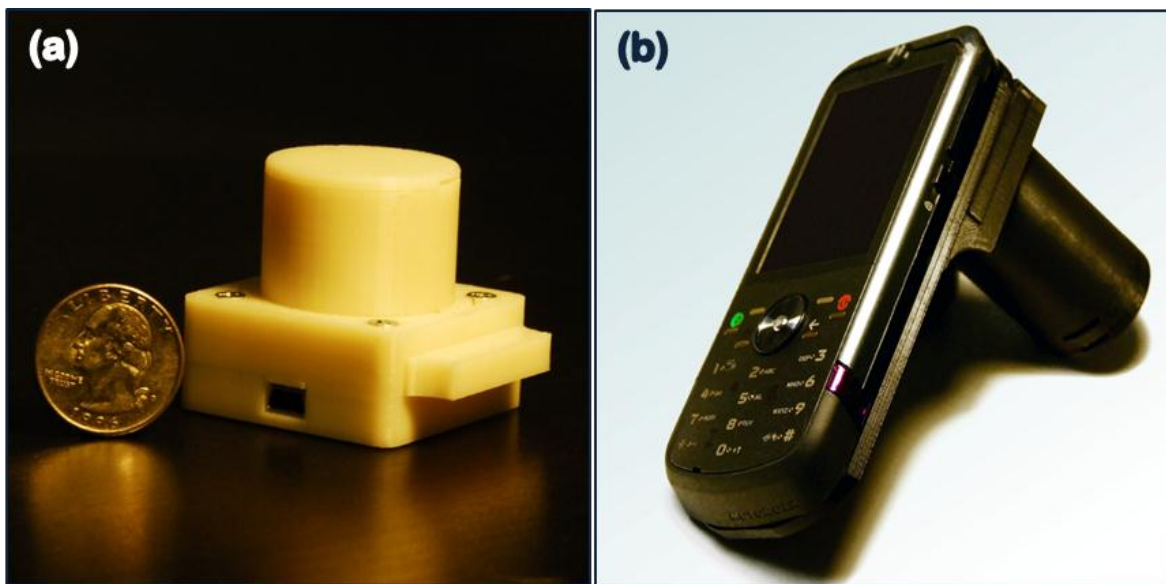


Figure 3.1 Schematic diagram of the portable lensfree telemedicine microscope (a) and lensfree cell-phone microscope (b)

3.2 Portable Lensfree Telemedicine Microscope

Here I illustrate an incoherent holographic microscope³⁷ weighing ~46 grams with dimensions smaller than 4.2 x 4.2 x 5.8 cm that achieves ~1-1.5 μm resolution (sufficient to

image e.g., sub-cellular features) over a large field of view (FOV) of $\sim 24 \text{ mm}^2$, which constitutes >10 fold improvement compared to a typical 10X objective-lens FOV. A simple light-emitting-diode (LED - OSRAM Opto Semiconductors Inc., Part# LY E65B – center wavelength: 591 nm, bandwidth: 18 nm) is utilized for illumination and initially filtered by passing the incoherent LED light through a butt-coupled large pinhole (aperture) of $\sim 50\text{-}100 \text{ }\mu\text{m}$ diameter, which also eliminates the need for any coupling and focusing optics between the LED and the pinhole plane (Fig. 3.2). After propagating in air a distance of e.g., $\sim 3\text{-}4 \text{ cm}$ inside the customized tubes, spatially filtered LED light interacts with the sample of interest that is loaded from the side through a simple mechanical interface (see Fig. 3.2). Each object (e.g., cells) within the sample scatters, absorbs and refracts the incoming light based on its size, morphology, sub-cellular elements, and refractive index. The interference of the light waves that passed through the cells with the unscattered LED light creates the hologram of each cell with unit fringe magnification, which is detected using a USB (universal serial bus) powered CMOS (complementary metal-oxide semiconductor) sensor array (Model: MT9P031, Micron Technology – pixel size: $2.2 \text{ }\mu\text{m}$, 5 Mpixels) without any lenses (Fig. 3.2). The recorded holograms are then digitally transferred to a computer for rapid reconstruction (see Chapter 2) of microscopic images of the sample. This computation does not need to be performed locally since wireless transmission of the acquired lensfree holographic images (using e.g., a cellphone through a USB connection) to a central PC station could potentially be used to reduce the hardware and software requirements at the user end. Data load of such a cloud computing model is rather easy to manage since each lensfree holographic image can be compressed (without loss of apparent resolution)³⁷ to less than 0.1 Mbytes per 1 mm^2 field of view (FOV).

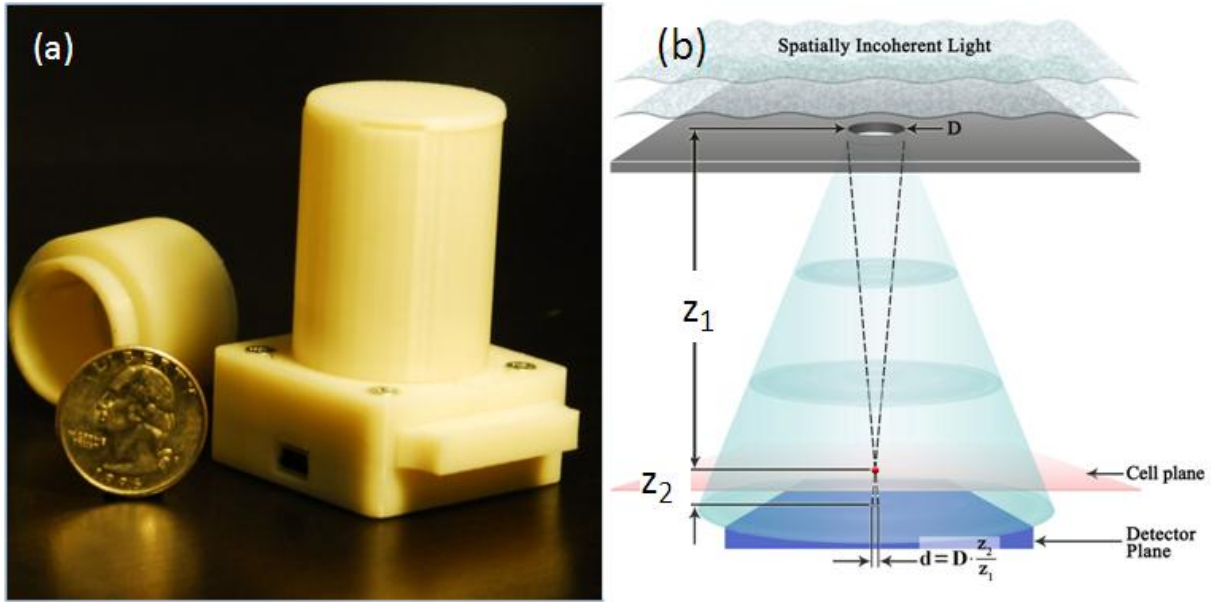


Figure 3.2 (a) A lensfree holographic on-chip microscope is shown. It utilizes an LED source (at 591 nm) with an aperture of $\sim 50\text{-}100\ \mu\text{m}$ in front of the source. The LED and the sensor are powered through USB connection from the side. This lensless holographic microscope operates with a unit fringe magnification (see Fig. 2.1) to claim the entire active area of the sensor as its imaging field of view ($\sim 24\ \text{mm}^2$). (b) Schematics of the incoherent lensfree holographic microscope shown in (a). Typical z_1 and z_2 distances used in this design are $\sim 2\text{-}5\ \text{cm}$ and $< 1\ \text{mm}$, respectively. The LED source and the CMOS sensor are powered through a USB connection from the side. The entire assembly weighs ~ 46 grams and achieves a numerical aperture of $\sim 0.1\text{-}0.2$ over an imaging field of view of $\sim 24\ \text{mm}^2$, which is more than an order of magnitude larger than the field of view of a typical 10X objective lens.

The digital image reconstruction process as outlined in Chapter 2, is quite fast taking less than 4 seconds for a total image size of ~ 5 Mpixels using a regular CPU (central processing unit – e.g., Intel Q8300) and it gets $>40\text{X}$ faster using a GPU (graphics processing unit – e.g., NVIDIA GeForce GTX 285) achieving < 0.1 sec computation time for ~ 5 Mpixels. The holographic images that are saved for digital processing are compressed using Portable Network Graphics (png) format, yielding a typical image size of $< 2\text{-}3\ \text{MB}$ for the entire $\sim 24\ \text{mm}^2$ FOV.

Depending on the image, a much smaller FOV can also be selected to reduce the overall size of the raw hologram.

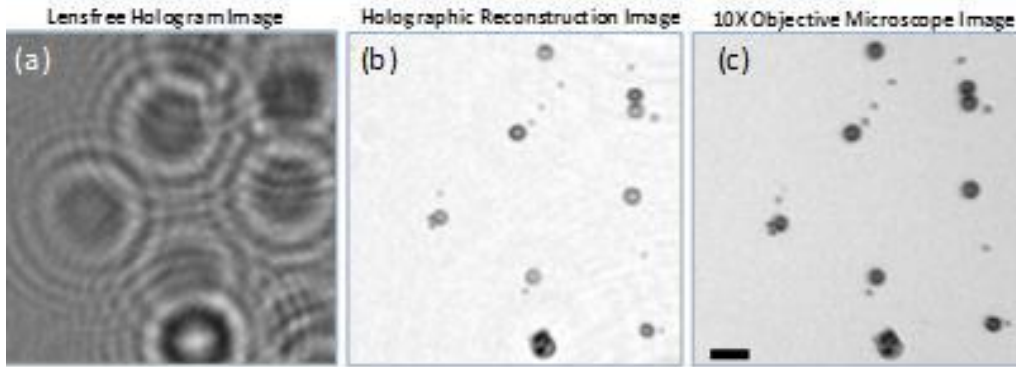


Figure 3.3 (a) A digitally cropped lensfree hologram of a blood smear that is acquired with the unit in Fig. 3.2 (a) is shown. Due to LED illumination spatial coherence diameter at the sample plane is much smaller than the imaging FOV, however it is sufficiently large to record the hologram of each cell individually. Integration time: 225ms; $D=50\ \mu\text{m}$; $z_1\sim 3.5\ \text{cm}$, $z_2\sim 1\ \text{mm}$. (b) Reconstruction result of the raw hologram shown in (a) for the same FOV illustrating the images of RBCs, platelets and a white blood cell. (c) 10X objective-lens ($NA=0.2$) microscope image of the same FOV as in (b) is shown for comparison purposes. Scale bar in (c) is $20\ \mu\text{m}$.

I have tested the imaging performance of the handheld lensless microscope of Fig. 3.2 with various cells and particles (such as red blood cells, white blood cells, platelets, as well as 3, 5, 7 and $10\ \mu\text{m}$ polystyrene particles), the results of which are summarized in Figs. 3.3 - 3.5. In these experiments, the reconstruction results of the presented digital microscope were compared against conventional microscope images of the same FOV obtained with 10X and 40X objective lenses with numerical apertures of 0.2 and 0.6, respectively. This comparison illustrates that the presented lensless on-chip microscope achieves sub-cellular resolution sufficient to determine the type of a white blood cell (granulocyte, monocyte or lymphocyte – towards 3 part differential imaging) based on the texture of its stained nuclei.

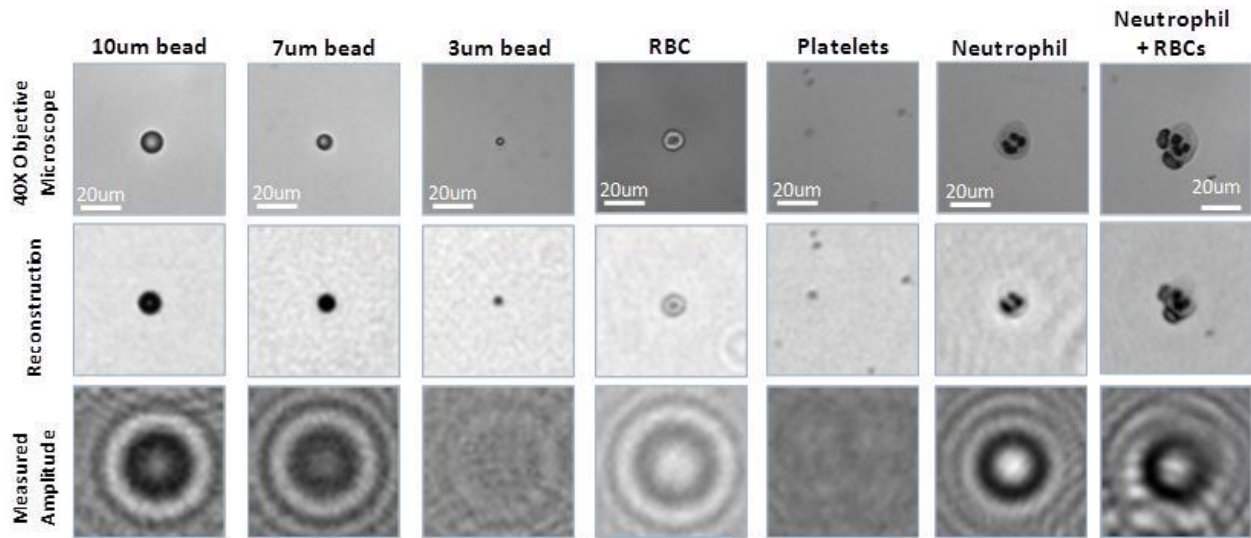


Figure 3.4 Various objects imaged using the lensfree incoherent holographic microscope of Fig. 3.2(a) are illustrated and compared against 40X objective-lens (NA=0.6) images of the same FOV. The bottom row illustrates the lensfree incoherent holograms that are digitally processed to reconstruct the middle row images. The last 3 columns are taken from a blood smear sample, whereas the other 4 columns on the left are imaged within a solution/buffer. Same imaging parameters as in Fig. 3.3 are used.

For blood smear imaging experiments (see Fig. 3.3 and last 3 columns of Fig. 3.4), whole blood samples were treated with 2.0 mg EDTA/ml; and 1 μ L of sample was dropped on the top of a type 0 (zero) glass cover slip and another identical cover slip was used for spreading and smearing the blood droplet over the entire cover slip with about 30 degree of smearing angle. Smear specimen was air-dried for 5 min before being fixed and stained by HEMA 3 Wright-Giemsa staining kit (Fisher Diagnostics). Dipping dried samples into three Coplin jars which contain methanol based HEMA 3 fixative solution, eosinophilic staining solution (HEMA 3 solution I) and basophilic solution (HEMA 3 solution II), respectively, was performed five times in a row for one second each step. Then, the specimen was rinsed with de-ionized water and air-dried again before being imaged. For aqueous imaging of

whole blood samples (see 4th column of Fig. 3.4), I used RPMI 1640 classic liquid media with L-Glutamine (Fisher Scientific) as a diluent to achieve a desired dilution factor. To achieve accurate dilution, I followed the international standard⁶⁴ established by the International Council for Standardization in Hematology (ICSH).

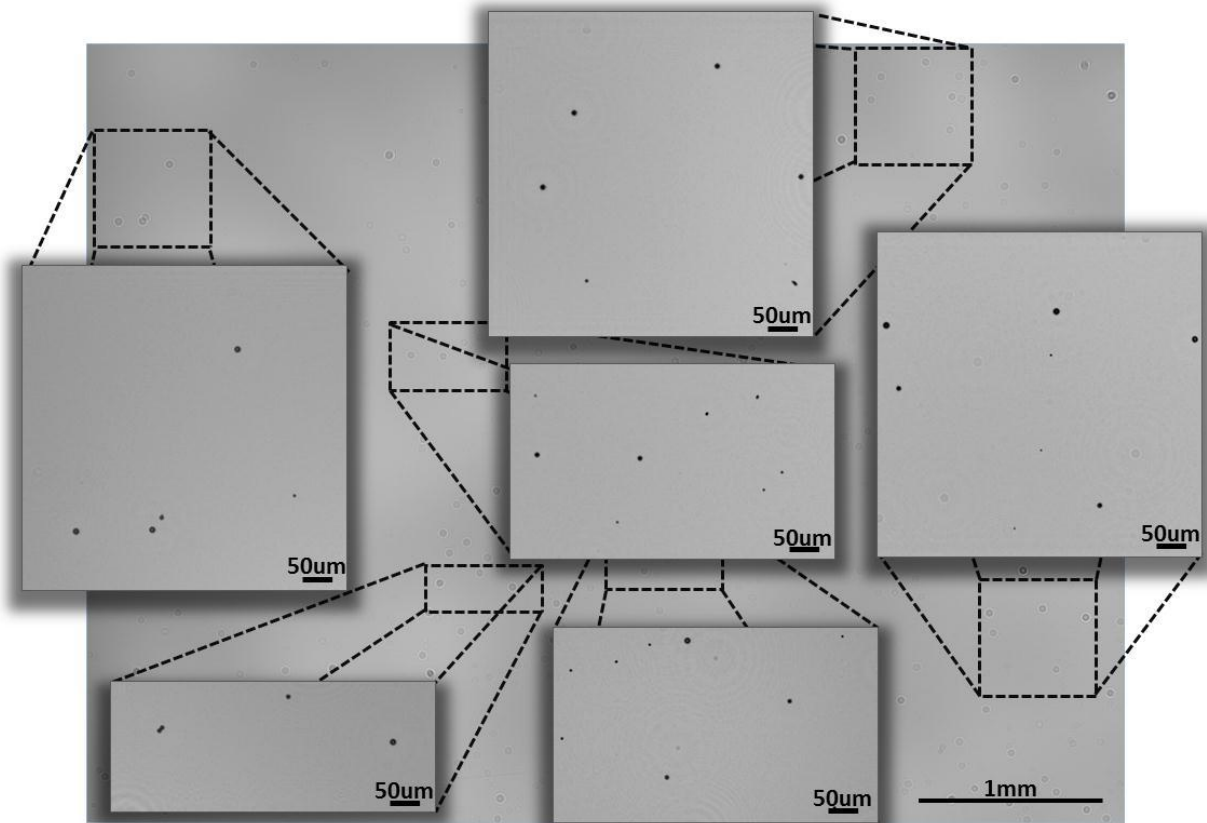


Figure 3.5 Full field-of-view ($\sim 24 \text{ mm}^2$) reconstructed image of a sample that is composed of 3, 7 and 10 μm polystyrene particles is illustrated. The raw holographic image is captured using the lensfree microscope of Fig. 3.2(a). Integration time: 220 ms; $D=50 \mu\text{m}$; $z_1 \sim 4 \text{ cm}$, $z_2 \sim 1 \text{ mm}$.

This compact and light-weight lensless holographic microscope has orders-of-magnitude improved light collection efficiency and is very robust to mechanical misalignments it may offer a cost-effective tool especially for telemedicine applications involving various global health problems such as malaria, HIV and TB.

3.3 Lensfree Microscopy on a Cellphone

Several diagnostic tests today are still conducted using conventional optical microscopes that are not always compatible with compact wireless systems to be used in resource limited settings. To address this important need, an important research direction is to miniaturize the existing designs of lens-based microscopes to be compatible with cellphones, while making use of the installed digital camera of the phone. Recent approaches⁶⁵⁻⁶⁶ successfully demonstrated both the significance and the feasibility of this approach.

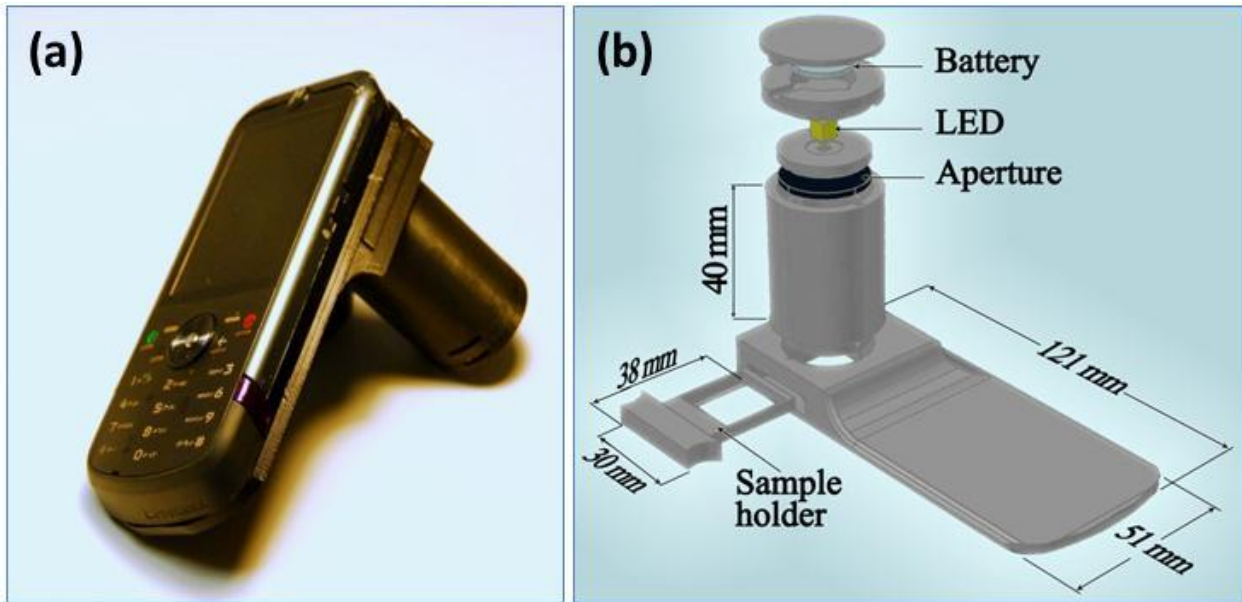


Figure 3.6 (a) A lensfree cellphone microscope which operates based on incoherent in-line holography is shown. The additional hardware installed on the cellphone weighs ~38 grams (<1.4 ounces) and is composed of an inexpensive light emitting diode (at 587 nm) with an aperture of ~100 μm in front of the source. This cellphone microscope does not utilize any lenses or other bulky optical components and operates with a unit fringe magnification to claim the entire active area of the sensor as its imaging field of view. The samples to be imaged are loaded from the side through a mechanical sample holder. (b) Schematic diagram of the microscope attachment shown in (a) is illustrated.

In order to provide a complementary effort to this important need in telemedicine, here I illustrate an alternative digital microscopy platform running on a cellphone.³² This holographic cellphone microscope does not utilize any lenses, lasers or other bulky optical components which greatly simplifies its architecture making it extremely compact and light-weight, such that only ~38 grams (~1.34 ounces) of attachment to the cellphone is required (see Fig. 3.6). Instead of using a coherent light source (e.g., a laser) as in conventional holography approaches,⁵³ an inexpensive light-emitting-diode (LED) is utilized to vertically illuminate the samples, which can be mechanically loaded into the cellphone from the side as illustrated in Fig. 3.6. This incoherent LED light is initially filtered by passing it through a large aperture of ~100 μm diameter to better control the spatial coherence of the illumination at the sensor plane. This large aperture also provides orders of magnitude improved light transmission efficiency as well as tolerance to misalignments. This spatially filtered LED light, after travelling in air a distance of ~4 cm (see Fig. 3.6(b)), interacts with the sample of interest, where each cell/particle within the sample scatters and refracts the incoming LED light based on its size, 3D morphology, sub-cellular elements, and refractive index. The interference of the light waves that passed through the cells with the unscattered LED light creates the hologram of each cell, which is detected using the CMOS (complementary metal-oxide semiconductor) detector array that is already installed on the cellphone camera unit. The lensfree hologram of each cell is extremely rich (despite the simplicity of the recording geometry) and permits rapid reconstruction of its microscopic image through digital processing as discussed in the Chapter 2.

A MotoZine ZN5 phone from Motorola is used as the starting base of this lensfree cellphone microscope. However, I should also emphasize that the presented technique can easily be installed on various other camera cell-phones (independent of the operating system,

the communication protocol or the service provider). This cellphone has a 5Mpixel color (RGB) sensor installed on it, which I used to capture the raw lensfree holograms as described in earlier sections. The LED source (OSRAM Opto Semiconductors Inc., Part# LY E63B-CBEA-26-1-Z – Center wavelength: 587 nm, Bandwidth: ~20 nm) is butt-coupled to a ~100 μm pinhole without the use of any focusing or alignment optics, illuminating the entire FOV of ~23.8 mm^2 of the cell-phone camera chip. Following Fig. 3.6, typical distances used in this design are ~4 cm between the source and the sample; and <1.5 mm between the sample and the sensor planes. The LED source is powered through a flat-battery installed at the top of the unit. The disposable samples to be imaged are loaded into the lensfree cellphone microscope within a mechanical tray from the side as illustrated in Fig. 3.6. This entire holographic microscope unit that attaches to the cellphone body weighs ~38 grams (~1.34 ounces) including the battery, the LED, the sample tray and the other mechanical components. In terms of the cost of the cellphone modification, excluding labor and the custom-made plastic components shown in Fig. 3.6, the other significant components are the LED (0.35 USD per piece for <10 units; 0.18 USD per piece for ~2000 units) and the flat-battery (0.2 USD per piece for ≥ 100 units), the cost of which can be further reduced through mass-production.

To convert a cellphone into a microscope to be used in telemedicine applications there are several approaches that one can take. If the cellphone does not have an installed camera unit on it, one can create an ultra-compact and light-weight digital microscope that can attach to the cellphone through e.g., a USB interface. Such a unique combination of a cellphone and a compact microscope can be used for telemedicine purposes to wirelessly transmit the acquired images to a remote location such as a central hospital or a clinic. In this

platform, however, I have explored the use of the existing digital camera unit of the cellphone to create a microscope as part of the cellphone. For this task, I have adapted lensfree holographic on-chip imaging and made it compatible with an existing camera-cellphone to conduct microscopy on a cellphone.

The color sensor that was already installed on the camera-phone is used to record the lensfree holograms of the cells. This color sensor chip, unlike a monochrome one, has color filters at each pixel yielding what is known as the Bayer pattern composed of a periodic array of red-green-blue (RGB) pixels. In a regular lensfree holographic microscope, a color sensor would hardly be the optimal choice, since not all the pixels would receive enough light under quasi-monochromatic illumination, which in this case is at ~ 587 nm. As summarized in Fig. 3.7, to handle this issue of hologram distortion due to the Bayer pattern of the camera-phone, a digital image reconstruction process involved an extra step³² of converting the raw format (Bayer Pattern Image) into a monochrome equivalent image before conducting holographic reconstruction of the particle (e.g., cells) images.

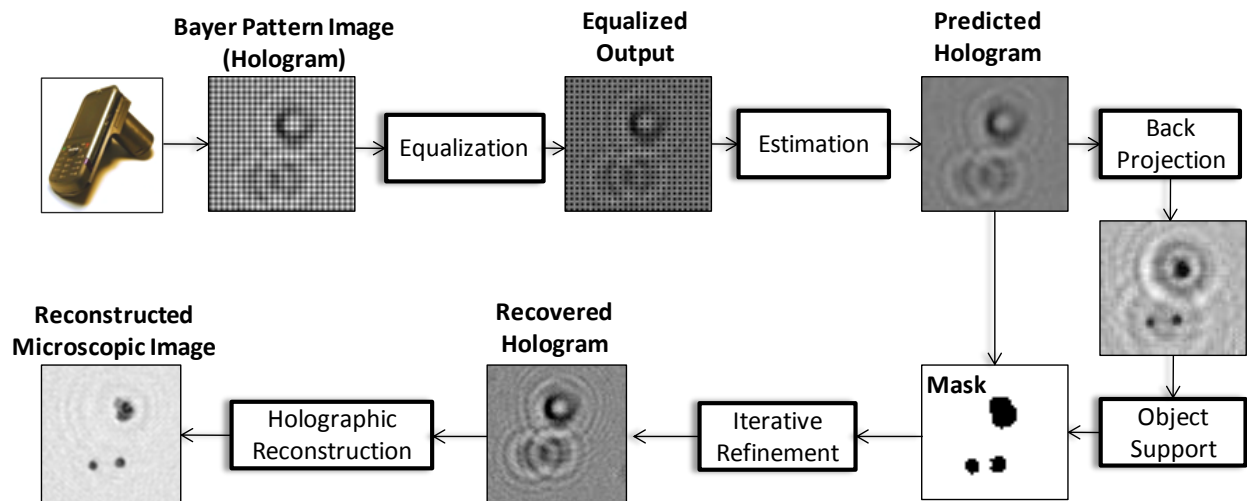


Figure 3.7 De-Bayering algorithm developed to create monochrome holographic images from Bayer patterned output of the lensfree cellphone microscope is summarized. Red and Green channels of the acquired raw

holographic image are equalized using a background image that was recorded with identical illumination conditions as the object. Blue pixels are estimated from their Red and Green neighbors (which include high SNR information) using an edge-aware interpolation approach and are further refined through an iterative recovery process with the help of an automatically generated object support mask. Finally, the recovered hologram is up-sampled and fed into a custom-developed holographic reconstruction algorithm (see Chapter 2) to create the corresponding microscopic images of the objects.

To demonstrate the performance of this lensfree cellphone microscope, I imaged several micro-particles (with diameters of 3 and 7), as well as red blood cells, white blood cells, and platelets, the results of which are summarized in Fig. 3.8. In these experiments, the disposable samples were inserted into the lensless cellphone microscope from the side for detection of their holographic shadows, illustrated in Fig. 3.8 bottom row. These holographic shadows were then digitally processed using a custom-developed reconstruction algorithm to create the microscopic images of the samples shown in the same figure within the middle row. Because of its significance for global health, I also imaged a waterborne parasite, namely a *Giardia Lamblia* cyst, with this lensfree cellphone microscope, the result of which is also illustrated in Fig. 3.8, first column. For comparison purposes, the same objects were also imaged using a conventional lens-based microscope (see Fig. 3.8 top row), providing a decent match to the lensfree imaging results. The spatial resolution of the lensfree reconstructions, under unit fringe magnification, is limited by the pixel size of the sensor, which in this case was $\sim 2.2 \mu\text{m}$ for each color pixel. For a monochrome sensor of the same pixel size, it can be normally achieved a sub-pixel resolution of $\sim 1-1.5 \mu\text{m}$ as discussed in previous section, however, the distortions and the lower signal to noise ratio introduced by the color filters under quasi-monochromatic illumination relatively degrades the spatial resolution when compared to a monochrome sensor. With recently emerging sub-micron

pixel CMOS sensors⁶⁷, the resolution could be further enhanced to claim $< 1 \mu\text{m}$.

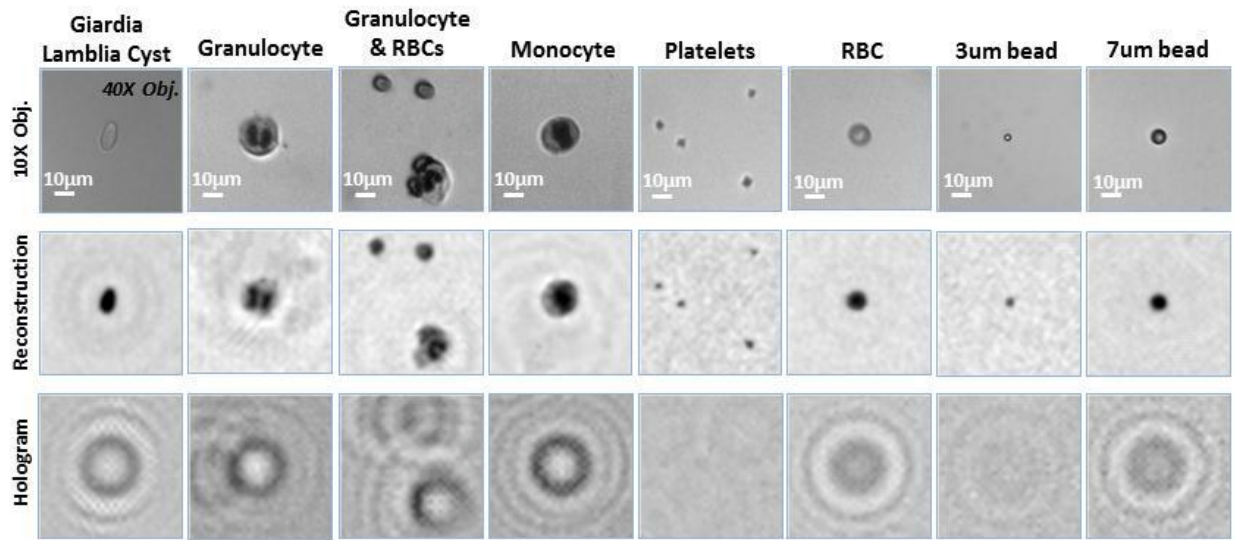


Figure 3.8 (a) Imaging performance of the lensfree cellphone microscope shown in Fig. 3.6(a) is compared against a regular microscope (10X objective lens, 0.25 numerical aperture) for various micro-objects, including red blood cells, white blood cells (monocytes and granulocytes), platelets, Giardia Lambliia cyst, as well as 3 and 7 μm diameter particles. The lensfree holograms captured by the cellphone sensor are digitally processed within less than 30 ms to reconstruct microscopic images of the specimen as shown on the middle column.

An important benefit of this lensfree cellphone microscope towards telemedicine and global health related applications could be to bring the function of microscopy to remote locations for performing more accurate medical diagnostics or even for screening of water quality in resource poor environments. For this end, in an ideal setting, the cellphone itself should be used not only for the actual holographic image acquisition, but also for wireless transmission of the raw images together with other related information (such as demographic data of the patient, the location, etc) to a central computer installed in e.g., a clinic or a hospital for gathering larger sets of data from remote locations. This implies that the holographic reconstruction process can ideally be performed remotely such that the

computational burden on the cellphone hardware can be significantly reduced. Using a cost-effective graphics processing unit (GPU) installed in e.g., a central hospital, the digital image reconstruction from the raw holograms captured by this cellphone microscope can be achieved within less than 1 second, i.e., the end-users can quickly have access to the reconstructed microscopic images through wireless communication.

The above discussed model of operation surely relaxes the hardware and software requirements on the cellphone unit, which is the right step to further reduce the cost, size and the weight of the lensless microscopy platform. However, it puts the entire burden on wireless data communication, which can be expensive and time consuming depending on the status of the network. To mitigate this problem, I investigated the compressibility of raw holographic images to better estimate the minimum amount of digital holographic data to be transmitted over the wireless link without an apparent loss of resolution in the microscope image. As a result of this study (see Fig. 3.9), It was found out that the recorded holograms with this lensfree cellphone microscope are highly compressible, such that for one pixel of the holographic image it would only be necessary to transmit (on average) ~ 3 Bits in PNG (portable network graphics) format, which provides lossless compression. This implies that 1 Mega Pixel worth of raw holographic data would require transmission of only ~ 0.375 Mbytes. In other words, to transmit a holographic image that contains the microscopic information corresponding to a field of view of $\sim 5 \text{ mm}^2$, it would be needed to transfer only 0.375 Mbytes over the wireless network. Fig. 3.9 summarizes these results by showing how the reconstructed image is getting affected as one quantizes the holographic image using different bit depths and saves it in PNG format. These results imply that it can be quickly communicated back and forth between the lensfree cellphone microscope and the central processing unit with much smaller data rates (compatible with GSM

networks) reducing the total cost of wireless data transfer without degrading the microscopic image quality.

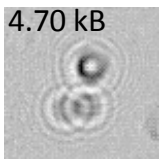
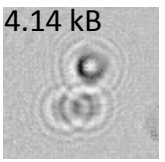
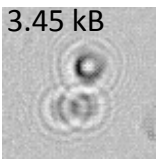
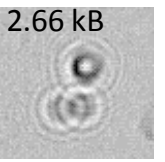
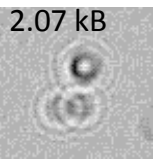
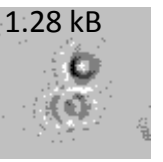
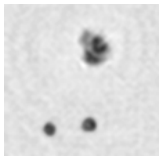
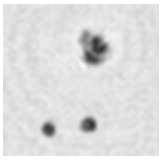
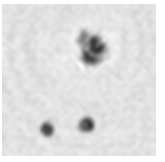
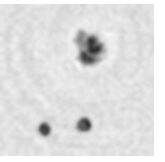
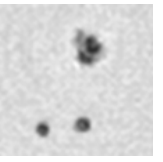
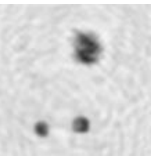
Hologram Intensity	 4.70 kB	 4.14 kB	 3.45 kB	 2.66 kB	 2.07 kB	 1.28 kB
Reconstructed Image						
Bit Depth	8	7	6	5	4	3
Image Size	6.68 Bits/Pixel	5.89 Bits/Pixel	4.91 Bits/Pixel	3.78 Bits/Pixel	2.94 Bits/Pixel	1.82 Bits/Pixel

Figure 3.9 The change in the reconstructed image quality of the lensfree cellphone microscope is illustrated as a function of the number of steps used for uniform quantization. The objects are red blood cells and a granulocyte on a blood smear sample. The top row presents the processed lensfree holograms of the cells captured by the cellphone microscope, where the digital size (in kBytes, when saved in PNG format) of each holographic image is indicated at the left corner as an inset. The middle row presents the reconstructed images of the cells for each bit depth. These results demonstrate that even for a bit depth of 4 (the second column on the right), the holographic recovery still remains very good at an average image size of 2.94 Bits/Pixel. This implies that for one pixel of the holographic image it would only be necessary to transmit (on average) 2.94 Bits in PNG format. In other words, 1 Mega Pixel worth of holographic data (corresponding to an imaging field of view of $\sim 5\text{mm}^2$) on average would require transmission of only ~ 0.38 Mbytes.

I believe that this compact and light-weight microscopy platform running on a cellphone could be very important especially for various global health problems by providing infectious disease diagnosis from bodily fluids, as well as rapid screening of the quality of water resources.

Chapter 4 Lensfree Microscopy for Global Health Applications

4.1 Water Quality Management using Field-Portable Lensfree Holographic Microscopes

Waterborne diseases associated with insufficient provision and sanitation of water resources stand for one of the most important global challenges endangering human health and well-being especially in the developing parts of the world. The same danger also occurs during natural disasters and wars, where water treatment and sewage facilities lose their functionality. As a matter of fact, the occurrence of waterborne diseases has been dramatically increasing worldwide including in highly industrialized countries such as the United States.⁶⁸⁻⁷¹ Two widely spread examples of such diarrheal diseases include Giardiasis and Cryptosporidiosis which are caused by protozoan parasites,⁷² namely *Giardia Lamblia* and *Cryptosporidium Parvum*, respectively. Unfortunately, these parasites can survive in cold water for several weeks and are resistant to most of the conventional water treatment methods such as chlorination.⁷³

Various approaches have been demonstrated so far for identification and quantification of pathogens in drinking and recreational water resources.⁷⁴⁻⁹² Traditional culture-based methods are time-consuming and have serious drawbacks due to lack of accurate enumeration methods as well as rapid transition of some of the species into non-culturable state after being released into freshwater.^{77,78} To address the challenges of these laborious tools, culture-independent techniques have also been demonstrated, which utilize various technologies including polymerase chain reaction (PCR),^{79,80} DNA microarrays and biosensors,⁸¹⁻⁸³ surface plasmon resonance,⁸⁴ immunomagnetic separation,⁸⁵ flow cytometry, as well as opto-fluidics and others.⁸⁶⁻⁹² Although these approaches complement each other

and emerge as effective tools for detection of pathogens in water, such platforms require moderately complex maintenance and operation skills together with relatively bulky and expensive architectures which partially hinder their application in field settings.

To provide an alternative solution to this important problem, here I investigate the use of the field-portable lensfree holographic microscope described in Chapter 3 (see Fig. 3.2(a)) to image and automatically detect pathogenic protozoan parasites such as Giardia Lamblia and Cryptosporidium Parvum at low concentration levels of $<400/\text{mL}$ without the use of any pre-concentration steps.⁵² Having a total imaging field of view of $\sim 24 \text{ mm}^2$ (i.e., more than an order of magnitude larger FOV than a typical 10X objective lens) together with a numerical aperture (NA) of $\sim 0.1-0.2$, this compact and light weight microscope may provide an important high-throughput analysis tool for combating waterborne diseases especially in resource poor settings.

To investigate the performance of the lensfree holographic microscope as a screening tool for water quality management, I imaged heterogeneous and homogeneous solutions of two protozoan pathogens; Giardia Lamblia Cyst and Cryptosporidium Parvum which are commonly spread by contaminated drinking water (see Fig. 4.1). In these experiments, parasite suspensions were fixed in 5% Formalin at pH 7.4 / 0.01% Tween 20 with a concentration of 5×10^6 parasites/mL (Waterborne Inc., USA). Each parasite sample is placed between two identical type-1 glass slides using a micro-pipette.⁹³ This disposable sample is then positioned onto the sample tray located on the side of the lensfree microscope shown in Fig. 3.2(a). Fig. 4.1 left column illustrates the raw lensfree holograms of these pathogens (over selected regions of interest that are digitally cropped from a much larger FOV of $\sim 24 \text{ mm}^2$). The middle column of the same figure shows the reconstructed microscopic images of these parasites (see Chapter 2 for lensfree image reconstruction process). For comparison purposes, the same regions of the sample

are also imaged using a 40X objective lens (NA~0.65) as illustrated in the right column of Fig. 4.1, which very well match to the lensfree reconstruction results.

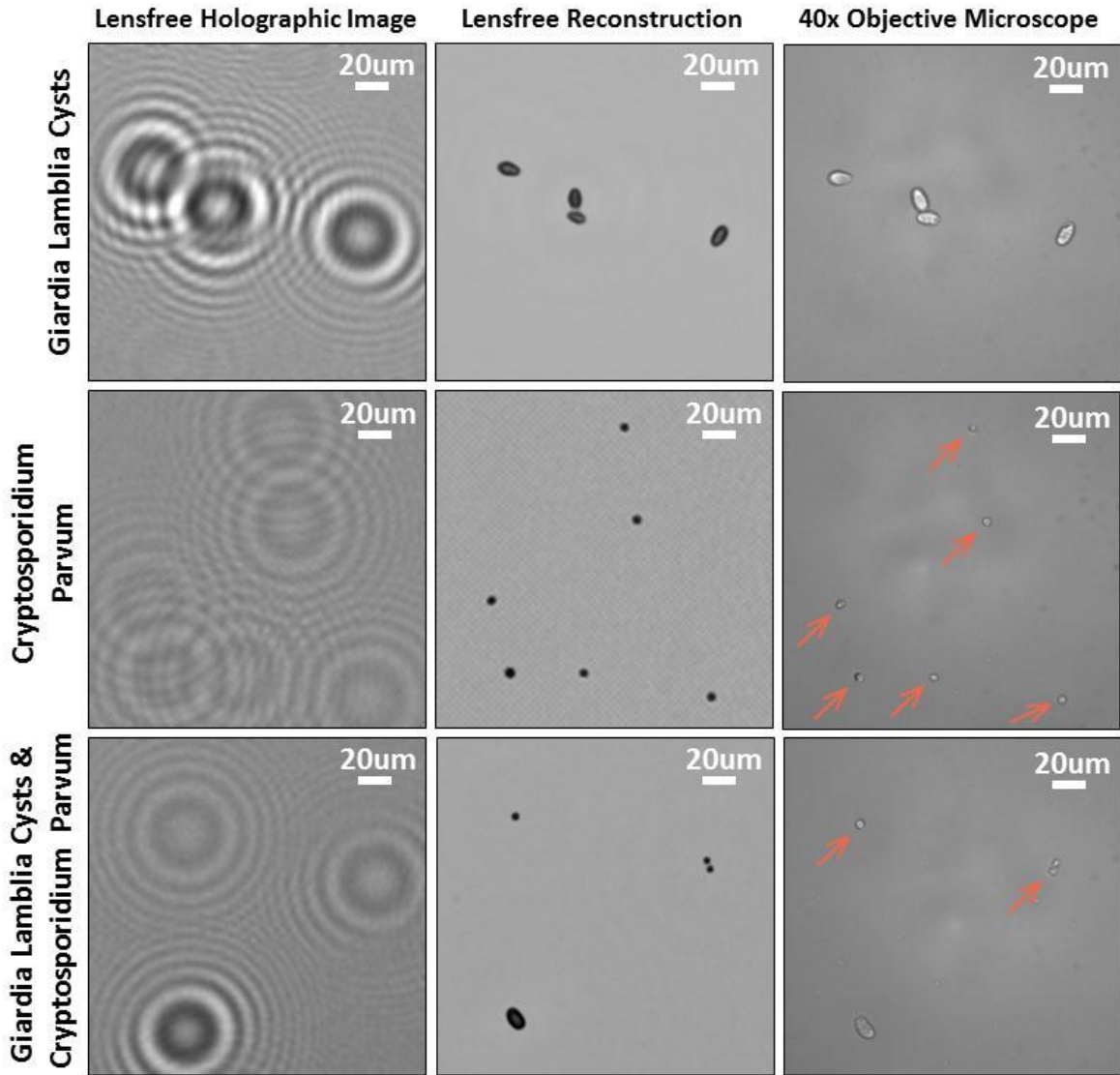


Figure 4.1 Lensfree holographic imaging results of homogeneous and heterogeneous samples of *G. Lambliia* Cyst and *Cryptosporidium Parvum* are illustrated. The raw holographic images (first column on the left) are acquired using the lensfree microscope shown in Fig. 3.2(a); and are digitally processed using custom developed image reconstruction algorithm³⁷ explained in Chapter 2. Holographic reconstruction results (middle column) show very good agreement with the corresponding images obtained using a 40X objective-lens (NA~0.65) shown on the third column. Note that because the samples were suspended in a solution, their relative orientations are slightly shifted in

the microscope comparison images. Since *Cryptosporidium Parvum* samples are relatively small with weak scattering properties their transmission microscope images are rather faint; therefore red arrows were used to point to their locations.

Next, I imaged *Giardia Lamblia Trophozoite* samples using the same lensfree holographic microscope (see Fig. 4.2). Compared to cyst stage (Fig. 4.1), Trophozoites have flagella and nuclei, together with a more complicated morphology and subcellular structure (Fig. 4.2). As shown in Fig. 4.2, holographic reconstruction enables imaging of both the phase and amplitude of these smear samples which nicely match with the 40X objective lens images of the same samples, revealing both the flagella as well as the inner features of the stained *Giardia Lamblia Trophozoites*. For these experiments, 1 μL of *G. Lamblia Trophozoite* sample ($\sim 10^6/\text{mL}$) is dropped on the top of a type-0 glass slide and another glass slide is used for smearing the sample droplet with ~ 30 degrees spreading angle. Smear specimen was air-dried for 5 minutes in room conditions. For the staining process, air-dried samples were sequentially dipped into three jars which contained HEMA 3 fixative solution, HEMA 3 Eosinophilic staining solution (Fisher Scientific), and de-ionized water, which was then repeated 5 times in a row.

These images shown in Figs. 4.1-4.2 illustrate the success of the lensfree holographic microscope for faithfully imaging *Giardia Lamblia Cysts*, *Cryptosporidium Parvum* and *Giardia Lamblia Trophozoites*. However the concentration of the imaged parasites in these experiments was $\geq 10^6/\text{mL}$, which does not shed any light on the detection sensitivity limits of this platform. As a matter of fact, the lensfree holographic microscope of Fig. 3.2(a) has significant advantages to provide rapid screening of large volumes. First, its imaging field of view is $\sim 24 \text{ mm}^2$, which is significantly larger than lens based conventional microscopes. Second, in terms of depth of field, lensfree in-line holography is quite advantageous since it

can image a deeper channel, permitting larger volumes to be screened in a single shot.

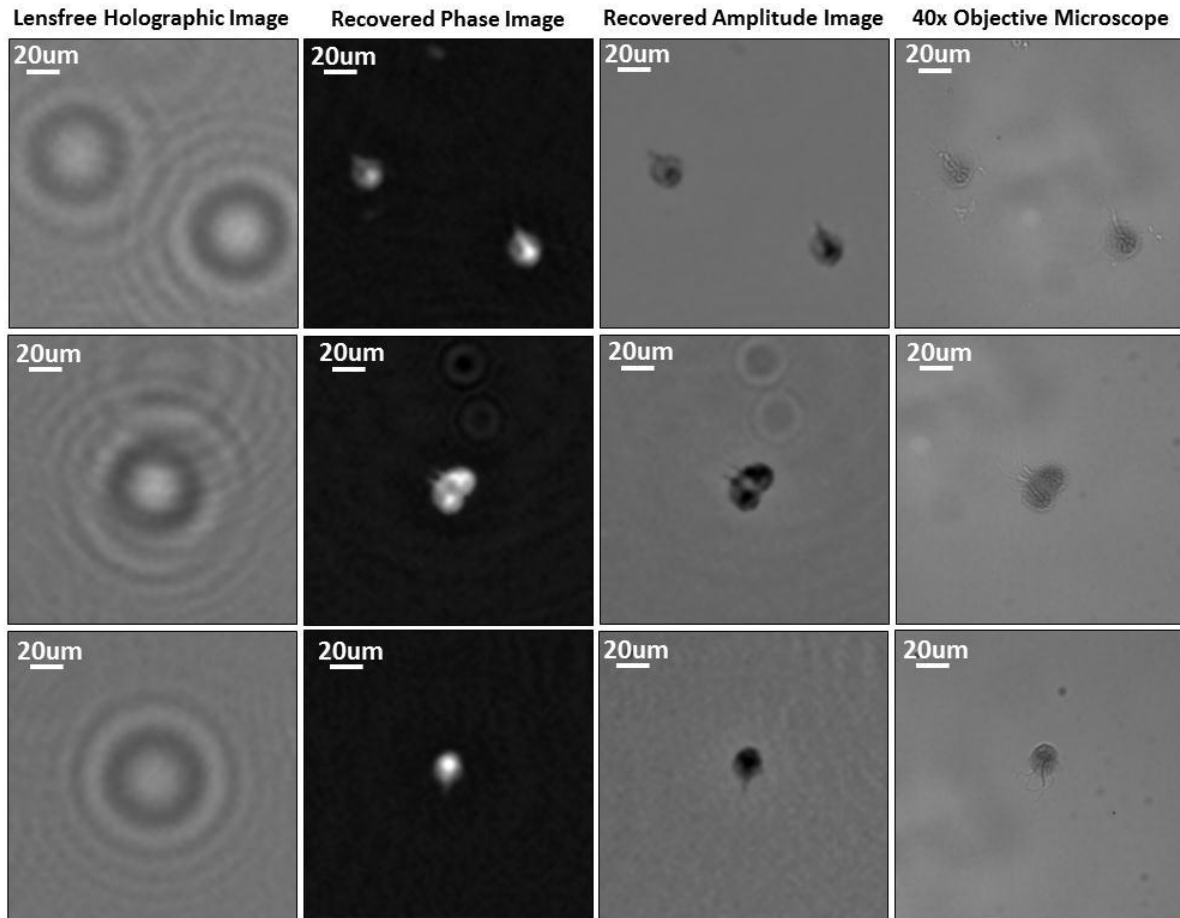


Figure 4.2 Lensfree holographic imaging results of *G. Lamblia* Trophozoite smears are illustrated. The raw holograms of the samples are acquired using the lensfree microscope of Fig. 3.2(a) and are shown on the left column. The second and third columns at the middle show the reconstructed phase and amplitude images from these lensfree holograms, respectively. The flagella of the *G. Lamblia* Trophozoite samples are clearly visible in both the phase and amplitude images. For comparison purposes the same smear samples are also imaged using a 40X objective lens (NA~0.65) the results of which are shown in the right column, which nicely match to lensfree reconstruction results.

In order to test the detection limits of the lensless holographic microscope, I further imaged and automatically characterized parasite counts of several diluted samples containing *Giardia Lamblia* Cysts (see Fig. 4.3). I should emphasize that the standard pre-concentration

steps⁹⁴⁻⁹⁶ that enrich the density of the sample before the detection process are not used here as my aim was to exclusively quantify the counting limits of the lensfree holographic microscope.

In these automated parasite counting experiments, I started with an initial concentration of $>1.5 \times 10^6$ parasites/mL, and then diluted it by 1024, 2048, 4096 and 8192 times to create 4 batches of known parasite concentrations, corresponding to 1510/mL, 755/mL, 378/mL, and 189/mL respectively. The original cyst concentration was double checked with a regular bright-field microscope for validating the accuracy of the parasite density. 13 measurements were then made for each one of these dilution levels (i.e., 52 measurements total). In each measurement, the sample solution was placed within a custom-made cuvette that had a controlled depth of 2.5 mm. Before imaging, I let the samples in the cuvette sediment for ~20 minutes, after which the cuvette was imaged using the lensfree holographic microscope shown in Fig. 3.2(a). These holographic images were then reconstructed to create microscopic images of the sample, which were digitally processed for automated counting of Giardia Lamblia Cysts using a custom developed pattern matching algorithm.^{52,97} The results of this automated counting process are summarized in Fig. 4.3, which indicates that the lensfree holographic microscope on average counted 81.6, 39.9, 23.7 and 16.0 Giardia Lamblia Cysts over the entire imaging FOV ($\sim 24 \text{ mm}^2$) for original cyst concentration levels of 1510/mL, 755/mL, 378/mL, and 189/mL, respectively. Considering the fact that the channel height is 2.5 mm in each cuvette, these average count values per FOV correspond to measured parasite densities of 1372/mL, 671/mL, 398/mL, and 270/mL, which exhibit an average error of 9.1%, 11.1%, 5.3%, and 42.9% for each dilution level, respectively (see Fig. 4.2 for details). In these results, no data points among 52 measurements were eliminated regardless of their value with respect to the mean and the standard deviation. By simply eliminating the maximum and the minimum of the measured values in each batch (which

reduces the number of data points to 11 from 13 for each dilution level), then the mean error in concentration measurements reduced to 7.4%, 7.3%, 3.5% and 37.2%, respectively. These results validate the performance of the lensfree holographic microscope to quantify Giardia Lamblia Cyst concentration of a solution down to a level of 385 parasites/mL with a mean error of <10%. For a lower concentration of ~190 parasites/mL, this mean error increased to ~40% which corresponds to a standard deviation of only ~3 parasites per imaging FOV (24 mm²). I should also underline that using well established pre-concentration steps such as centrifugation and filtration,⁹⁴⁻⁹⁶ I can further improve the detection limit by a factor of e.g., ~100X to claim a detection sensitivity of <5 parasites/mL.

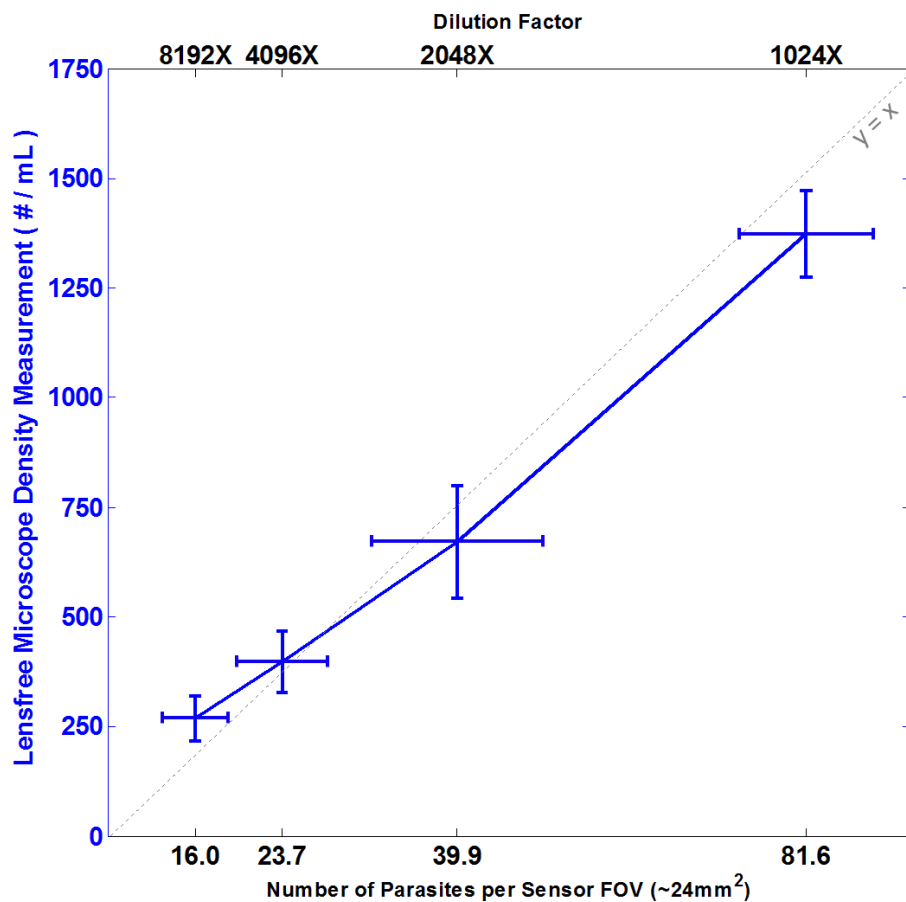


Figure 4.3 Lensfree holographic microscope of Fig. 3.2(a) is used to image 4 different batches of diluted water samples containing Giardia Lamblia cysts at concentration levels of 1510/mL, 755/mL, 378/mL and 189/mL. For

each dilution level, 13 different lensfree holograms corresponding to different samples of the same batch were acquired and digitally processed to reconstruct microscopic images of the samples. These reconstructed images were then automatically counted yielding the number of cysts per frame (over an imaging FOV of ~24 mm²). The above figure illustrates the mean and the standard deviation of these count results, which accordingly measured the average parasite concentration in each dilution level as 1372/mL, 671/mL, 398/mL, and 270/mL respectively. The mean errors in these parasite concentration measurements are 9.1%, 11.1%, 5.3%, and 42.9% respectively. These results validate the performance of the lensfree holographic microscope to quantify Giardia Lamblia cyst concentration of a solution down to a level of ~380 parasites/mL with a mean error of <10%. This also implies that using well established pre-concentration steps such as centrifugation and filtration,⁹⁴⁻⁹⁶ I can potentially improve the detection limits by a factor of e.g., ~100X to claim a detection sensitivity of <5 parasites/mL.

In summary, screening of water quality is a vital requirement to prevent water-associated diseases caused by insufficient sanitation techniques. Although current water-treatment methods offer effective solutions, highly populated urban areas and resource-limited settings still have this risk, and outbreaks continue to occur. Therefore, ancillary testing tools for rapid and quantitative determination of pathogenic contaminants in field-settings are needed to ensure public well-being. The use of lensfree holographic on-chip microscopes can be especially helpful for the detection of waterborne parasites within a mechanically robust, alignment-free and highly sensitive platform. These initial results demonstrate the promising potential of this field-portable on-chip imaging tool for rapid screening of contaminants in both fresh and recreational water resources.

4.2 Lensfree Imaging of Antibody Microarrays for High-Throughput On-Chip Detection of Leukocyte Numbers and Function

Leukocytes (white blood cells) are a heterogeneous mixture of cell types categorized based on size, shape of the nucleus, expression of surface markers and secretion of cytokines.

The numbers of leukocytes and proportions of leukocyte subsets change drastically in the presence of infections, malignancies and autoimmune disorders, making analysis of leukocyte subpopulations valuable in the diagnosis and monitoring of disease.⁹⁸ For example, the number of CD4 T cells and CD4/CD8 ratio are the key parameters used in monitoring human immunodeficiency virus (HIV) and AIDS.⁹⁹⁻¹⁰¹ Release of signaling molecule called cytokines is central to T-cell's role in orchestrating a well-coordinated immune response involving other leukocyte subsets. Therefore, T-cell cytokine profiling is an important indicator of immune system competency in fighting infections such as HIV.¹⁰²⁻¹⁰⁴ Traditionally, leukocytes are phenotyped based on surface antigen expression and cytokine production using flow cytometry.^{105,106} While enabling multi-parametric, high-throughput characterization of leukocytes, flow cytometry is expensive and complicated making this technology suboptimal for blood analysis performed at the point of care or in a resource-poor setting. As a result, considerable effort has been directed towards the development of miniature devices for simple and inexpensive leukocyte analysis.¹⁰⁷⁻¹¹¹

The number of CD4 T-cells in blood is the key diagnostic marker of HIV progression to AIDS and is routinely monitored in conjunction with antiretroviral therapy. Therefore, significant emphasis has been placed on development of miniature devices for CD4 T-cell counting.^{108,110,111} To provide a solution to this need, microfluidic devices modified with anti-CD4 antibodies (Abs) have been used to capture CD4 T-cells and have been shown to accurately predict T-cell numbers when compared with flow cytometry.¹⁰⁸ Rapid enumeration of cells captured inside the microfluidic device has been another important area of research where cell detection schemes based on electrical properties of cells or cell lysate have been described.^{112,113}

However, these approaches do not directly visualize the cells and may be susceptible to sample-to-sample variation.

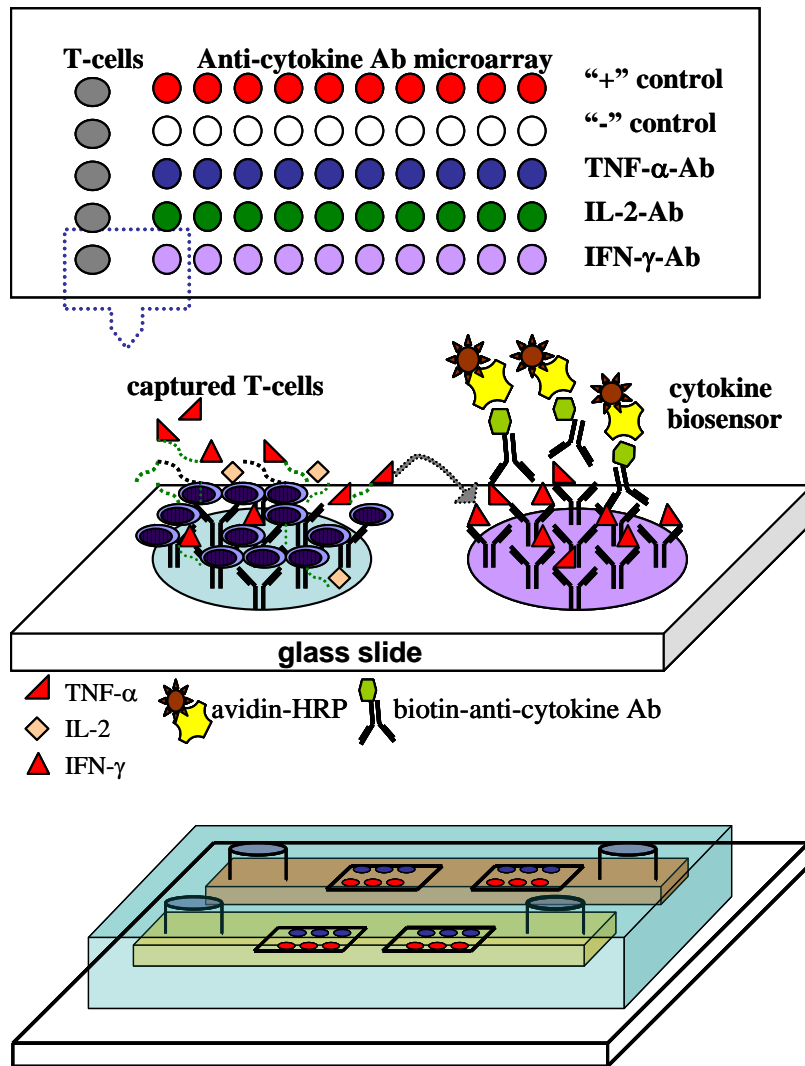


Figure 4.4 (A) Design of an antibody (Ab) microarray for capturing leukocytes and detecting secreted cytokines. T-cell Ab spots were printed next to spots for detection of IFN- γ , TNF- α , and IL-2. Antimouse IgG spots provided negative control whereas biotin spots were used for positive control. (B) Principle of operation of the assay. T-cells are captured in the immediate vicinity of cytokine-sensing Ab spots. On-chip activation of T-cells results in release of cytokines and detection of these secreted molecules on adjacent Ab spots. Sandwich immunoassay with colorimetric readout is used to visualize cytokine signal. (C) Ab microarrays are integrated with a microfluidic conduit to minimize blood volume required for analysis. T-cell capture and cytokine detection occurs in the microfluidic device.

In this section, I explore the use of lensfree holographic microscopy as a rapid, high-throughput cost-effective method for monitoring cell and cytokine signals on Ab microarrays.¹¹⁴ Towards this end, a microarray composed of cell-(anti-CD4, -CD8) and cytokine-specific (TNF- α , -IFN- γ , -IL-2) Ab spots was printed on hydrogel-coated glass slide (see Fig. 4.4), integrated into a silicone rubber microfluidic device, and incubated with human blood. Lensfree holographic imaging (described in Chapter 2) of Ab microarrays and (see Fig. 2.1 and 3.2) quantified CD4 and CD8 T-cell numbers as well as TNF- α , IFN- γ , and IL-2 signals. The use of Ab microarrays in tandem with high-throughput lensfree on-chip imaging paves the way to simple and cost-effective micro-devices for multi-parametric blood analysis at the point of care or in resource-poor settings.

Given the complexity of the immune response, it is clearly beneficial to be able to determine multiple immune markers from the same blood sample. To this end, the goal of the present work is to demonstrate that the simplicity and the cost-effectiveness of the device need not compromise information content of blood analysis. One way to enable multi-parametric blood analysis is to create surfaces containing antibody microarrays where different Ab spots encode for cell surface antigens or secreted molecules.¹¹⁵ For this end, the integration of Ab arrays inside fluidic devices and capture of pure CD4 and CD8 T-cells on Ab spots has been previously demonstrated.^{114,116} More recently, the strategies for detecting secreted cytokines or other proteins in the immediate vicinity of captured cells were described.¹¹⁷⁻¹¹⁹ While these previous reports pointed to the possibility of multiplexed analysis of cells and secreted cytokines from blood, cell enumeration was carried out by laborious manual counting while cytokine signals were detected with an expensive fluorescence laser microarray scanner. Creating a rapid, multi-parametric as well as high-throughput platform to address this important problem, I

combine the lensfree holographic imaging with antibody microarrays for the analysis of leukocytes from human blood. Please refer to the Reference 114 for more details on the methods and materials for the printing of Ab microarrays for cell and cytokine detection as well as its integration into a microfluidic device (see Fig. 4.4).

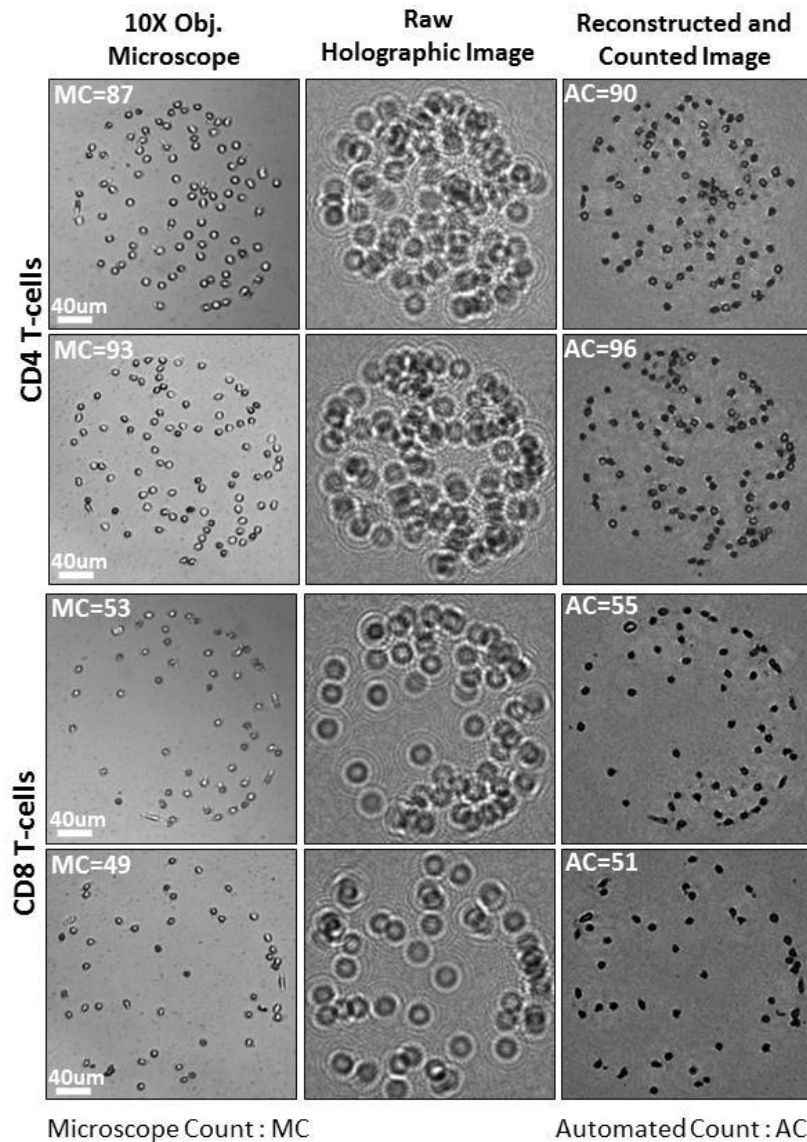


Figure 4.5 Lensfree holographic imaging- and conventional microscopy-based characterization of CD4 and CD8 T-cells on 300 µm diameter Ab spots. Subpanels demonstrate 10× objective-lens microscope images, representative raw holograms (amplitude), and reconstructed and counted holograms of the same Ab spots. Automated CD4 and

CD8 cell counting results using lensfree holographic microscopy match very well with conventional microscope count results.

To highlight the tandem use of Ab microarrays and lensfree holography platform for leukocyte phenotyping, I characterized the CD4/CD8 ratio from blood of healthy volunteers and HIV-infected patients. In these experiments, counts obtained by lensfree holographic imaging were compared to traditional brightfield microscopy to validate the optical characterization approach. Fig. 4.5 compares typical 10x objective-lens microscope images with raw holograms as well as the reconstructed holographic images of T-cells captured on 300 μm diameter Ab spots. Automated identification algorithms¹¹⁴ ensured that cell numbers obtained with holographic imaging were in good agreement with microscopy based counts. In a typical experiment, cells bound on 10 different CD4 and CD8 spots were enumerated and averaged to account for spot-to-spot variability. Fig. 4.6 compares CD4 and CD8 numbers obtained by lensfree holographic imaging and conventional microscopy-based counting for 10 T-cell clusters formed on 300 μm diameter Ab spots. These results show excellent agreement between the two approaches. A tremendous advantage of this approach is that automated cell counting of the entire imaging field of view ($\sim 24 \text{ mm}^2$) of the lensfree holographic imaging platform takes less than a few seconds even using a modest CPU (e.g., at 1.8 GHz).

It should be noted that immunostaining was not required in these T-cell counting experiments. Given the high purity of CD4 and CD8 T-cells on Ab spots, the phenotype was determined solely based on location of the cells within the microarray. The “location gating” was used to assign CD4 and CD8 phenotype to cells residing on anti-CD4 and anti-CD8 Ab spots, respectively. After determining the numbers of CD4 and CD8 T-cells, the CD4/CD8 ratio could be easily established. Fig. 4.7 shows CD4/CD8 ratios of healthy volunteers (n=5) and HIV-

infected patients (n=4) determined by lensfree holographic imaging and conventional bright field microscopy, respectively. As seen from these graphs, there was a close agreement between the two cell counting approaches. Lensfree imaging had significant benefits of capturing a large field of view and providing a rapid cell number readout. The CD4/CD8 ratios of HIV-infected patients were considerably lower than those of healthy subjects (see Fig. 4.7); this is consistent with depletion of CD4 T-cells during HIV.

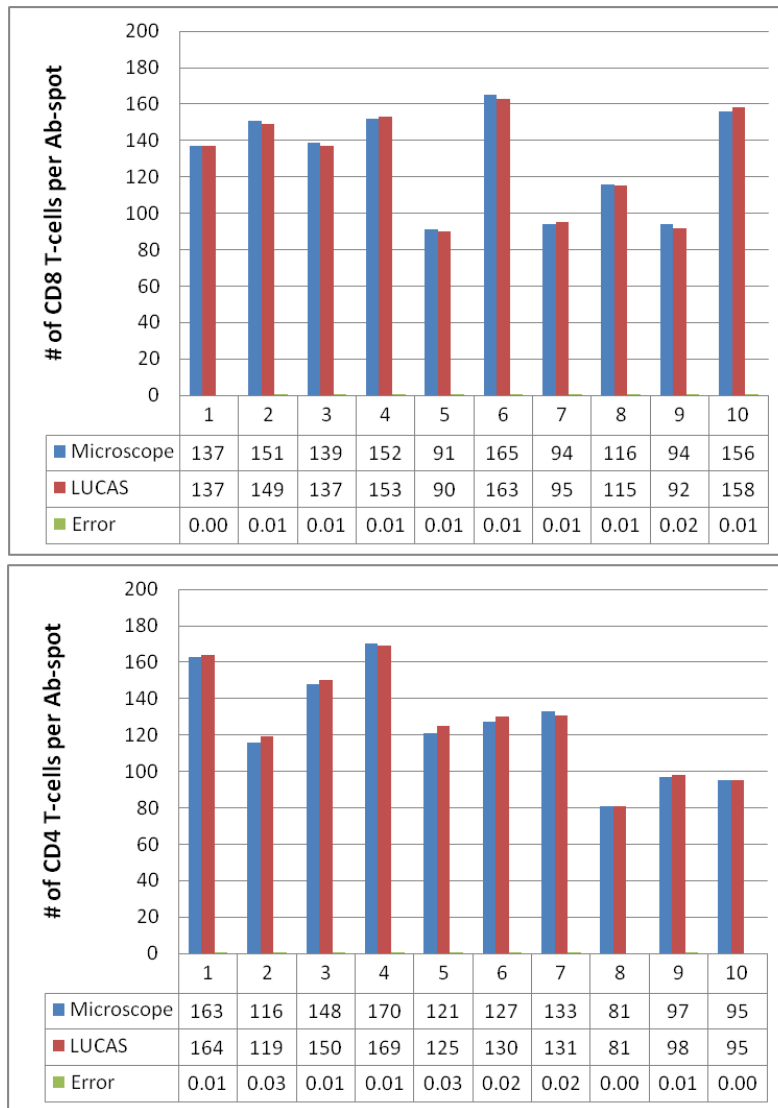


Figure 4.6 Representative histograms showing CD4 and CD8 T-cell counting on an array of Ab spots (n=10). Exemplary holographic imaging results are shown in Fig. 4.5.

The results of Figs. 4.5-4.7 further demonstrate that lensfree scanning allowed one to accurately enumerate surface-bound cells for a large array of Ab spots. T-cell binding to Ab microarrays occurred after 15 min of incubation with RBC depleted blood whereas automated counting of cells on microarrays with lensfree imaging required <4 s using a modest CPU. These results provide proof-of-concept multi-parametric analysis of leukocyte numbers and subset proportions using novel integration of Ab microarrays and lensfree holographic imaging. The information content of this cytometry platform will be further enhanced in the future by including on the same microarray chip various other Abs for capturing different leukocyte subsets (e.g., neutrophils, monocytes, and B-cells).

In summary, I employed lensfree holographic microscopy for high-throughput analysis of Ab microarrays without the use of any lenses or mechanical micro-scanners. Holographic microscopy allows rapid enumeration of CD4 and CD8 T-cells captured on Ab spots and determination of the CD4/CD8 ratio in blood of healthy and HIV infected subjects. The future development of a cytometry device integrating Ab microarrays, microfluidic sample delivery, and lensfree on-chip imaging will enable low cost yet multi-parametric blood analysis at the point of care or in low resource settings.

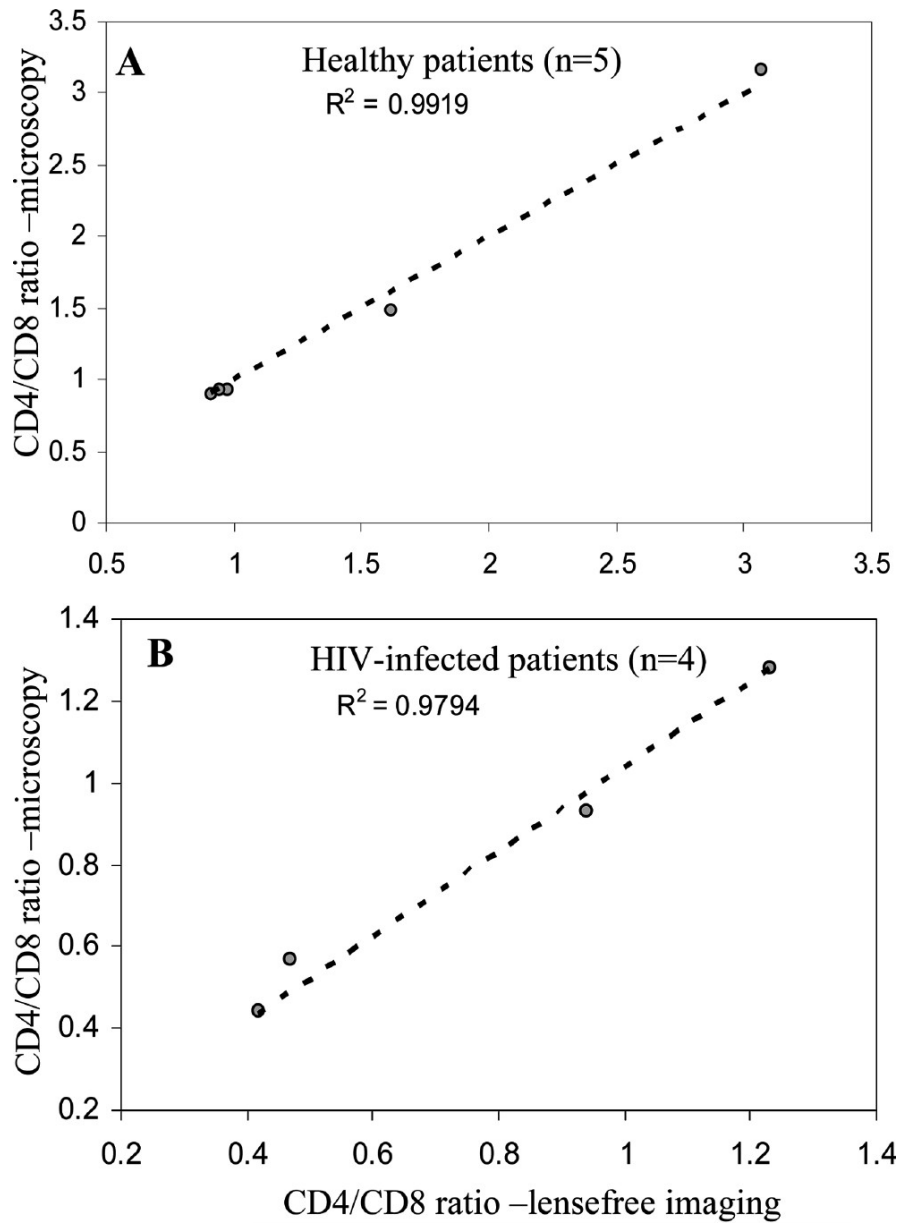


Figure 4.7 CD4/CD8 ratios obtained by lensfree holographic imaging platform as well as conventional microscopy for (A) healthy volunteers (n=5) and (B) HIV-infected patients (n=4) are illustrated. Automated lensfree holographic counting results were in close agreement with conventional lens-based microscopy counting.

Chapter 5 Lensfree Super-Resolution Microscopy using Wetting

Films on a Chip

5.1 Introduction

Screening vital signs of epidemics such as disease-marker cells, parasites or other contaminants within e.g., bodily fluids and water resources is a challenging task to perform in resource-limited field settings. As a result of the progress in advanced microscopy techniques, there has been considerable attention to investigate various infectious disease markers.¹²⁰⁻¹³² However, the use of such advanced microscopy modalities for the evaluation of infectious disease markers has been partially limited to well-established facilities due to their relatively bulky and complex architectures as well labor-intensive operation principles. Towards this end, field-portable lensfree pixel super-resolution microscopy^{47-51,133} has been demonstrated as a robust and cost-effective platform that is based on the recovery of high resolution digital in-line holograms of the objects through acquisition of multiple spatially shifted lensfree frames (see e.g., Fig. 5.1(b-c)). This on-chip microscopy modality is also based on partially coherent illumination such that the scattered optical fields from a specimen (e.g., a cell) interfere with the un-scattered background optical field creating in-line holograms of the objects located on a given opto-electronic sensor chip (see Chapter 2 for more details). This field-portable lensless microscope⁴⁷ achieves $< 1 \mu\text{m}$ resolution over a large imaging area of $\sim 24 \text{ mm}^2$, which is > 100 fold larger compared to e.g., a typical 40X objective-lens. Furthermore, since it does not require any bulky optical components or precise mechanical alignment, it provides a compact and cost-effective imaging tool⁴⁷ to rapidly monitor microscopic samples even in resource limited field environments.

On the other hand, the imaging performance of this lensfree pixel super-resolution microscopy is still limited by the detection SNR, which may pose certain limitations for imaging of e.g., weakly scattering phase objects that are refractive index matched to their surrounding medium such as sub-micron bacteria in water. To mitigate this limitation and significantly improve the imaging SNR and contrast, in this chapter, I demonstrate the use of ultra-thin wetting films to enhance the lensfree on-chip imaging capabilities toward reconstruction of finer morphological features of the samples having dimensions of e.g., $\sim 0.5 \mu\text{m}$.⁴⁶

Wetting thin-film dynamics have already been widely studied in chemistry and biology¹³⁴⁻¹³⁶ and were also utilized in imaging and sensing applications to enhance image contrast and sensitivity.¹³⁷⁻¹⁴¹ Among these prior results, a recent application of thin wetting films towards on-chip detection of bacteria^{140,141} provides a promising approach where formation of evaporation-based wetting films was used to enhance e.g., diffraction signatures of bacteria on a chip. While quite promising, this previous approach^{140,141} unfortunately cannot reveal microscopic images of the specimens under test, and is therefore limited in scope especially for handling heterogeneous or unknown samples, where fine morphological features of the objects need to be microscopically imaged for identification and characterization purposes.

Here I demonstrate an alternative implementation of thin wetting films on a chip that permits repeatable and reliable improvement in image quality of the field-portable lensfree super-resolution microscopes,⁴⁶ revealing deeply sub-micron spatial features of even weakly scattering objects over a large imaging area of $\sim 24 \text{ mm}^2$ (see Fig. 5.1). I demonstrate the improved performance of the lensfree pixel super-resolution microscopy platform by imaging various objects on a chip such as *E. coli*, human sperm, *Giardia lamblia* trophozoites, polystyrene micro beads as well as red blood cells (RBCs). Creating a sensitive, high-resolution and wide-

field micro-analysis toolset that can even work in remote or resource-poor environments, this wetting film based lensfree imaging platform could especially be important for combating global health challenges in third-world countries.

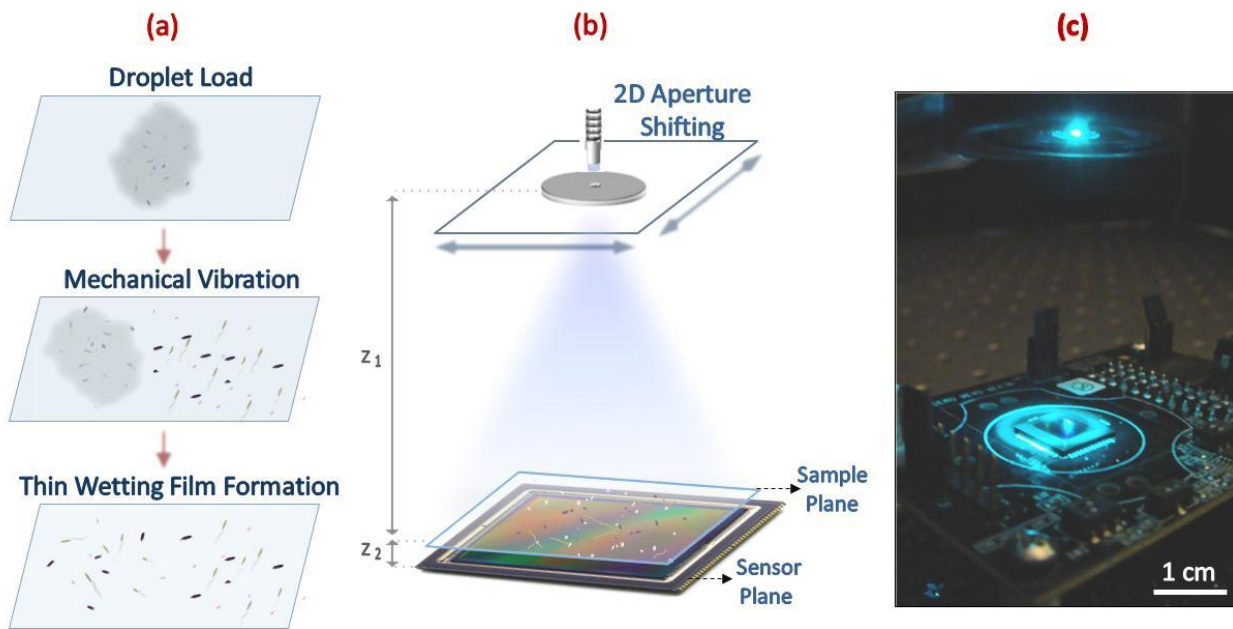


Figure 5.1 (a) Schematic diagram of wetting film formation procedure (not drawn to scale). After wetting film samples were formed on plasma cleaned glass cover slips, stable micro-lens effect is verified by multiple lensfree imaging experiments spread over a day. (b) Schematic diagram of lensfree pixel super-resolution microscopy set-up (not drawn to scale). The aperture to sample plane distance ($Z_1 = \sim 10$ cm) is much larger than the sample to sensor plane distance ($Z_2 = \sim 0.8-1$ mm) such that discrete spatial shifts of the illumination aperture (~ 100 μm diameter) results in sub-pixel shifts of lensfree object holograms on the digital sensor-array. This way the effective pixel size can be digitally reduced at the sensor plane down to e.g., $0.3-0.5$ μm to create higher resolution lensfree images. (c) The corresponding lensfree holographic microscopy set-up which uses a partially coherent light source that is emanating from a large aperture ($D = \sim 100$ μm). Wetting film samples were directly placed onto the CMOS sensor-chip which has an active imaging area of ~ 24 mm^2 .

5.2 Experimental Methods

For the imaging experiments reported here, I utilized Lensfree On-chip Pixel Super-

Resolution Microscopy^{47-51,133} that has been previously introduced by our research group. This emerging lensfree on-chip imaging modality is based on partially coherent illumination (such as a simple light-emitting diode - LED) and relies on the acquisition of multiple lower resolution in-line holograms (see Chapter 2) of the objects (e.g., cells) which are spatially shifted with respect to each other by sub-pixel pitch distances (see Fig. 5.1(b-c)). Using an iterative pixel super-resolution algorithm,^{47-51, 142-145} these sequentially captured lensfree holograms are digitally put together, recovering a higher resolution object hologram. This super-resolved lensfree hologram is then digitally processed through a custom-developed holographic image reconstruction software (see Chapter 2) to yield both phase and amplitude images of the specimens with sub-micron resolution over a large field-of-view (FOV) of $\sim 24 \text{ mm}^2$.

For the imaging experiments summarized in the next section, I used a quasi-monochromatic light source (500 nm center wavelength; $\sim 5 \text{ nm}$ bandwidth; Cornerstone T260, Newport Corp., USA) that is emanating from a large aperture of $\sim 100 \mu\text{m}$ diameter located at $z_1=10 \text{ cm}$ above the digital sensor array (CMOS - Aptina MT9P031I12STM) (see Fig. 5.1(b-c)). The samples to be imaged were located typically at $z_2 < 1\text{-}2 \text{ mm}$ from the active surface of the CMOS sensor-array.

Lensfree holographic microscopy platform described above also operates with unit hologram fringe magnification to claim the entire active area of the digital sensor array as its imaging FOV. As a result of this, individual in-line holograms of the samples can be poorly sampled since each object hologram occupies a relatively small region on the sensor array. Lensfree pixel super-resolution microscopy overcomes this undersampling issue due to the limited pixel density at the sensor-array e.g., a CMOS (complementary metal-oxide-semiconductor) chip by digitally synthesizing higher resolution holograms that effectively have

much smaller pixel sizes. And therefore, lensfree pixel super-resolution microscopy can achieve an effective numerical aperture (NA) of e.g., ~ 0.4 , corresponding to sub-micron spatial resolution over an imaging area that is equivalent to the active area of the opto-electronic sensor-array (e.g., $\sim 24 \text{ mm}^2$ in this case). However, the imaging performance of the lensfree pixel super-resolution microscopy is still limited by the detection SNR, which may pose certain limitations for imaging of e.g., weakly scattering phase objects.

In order to mitigate SNR related limitations in partially coherent lensfree on-chip microscopy in general, I utilized ultra-thin wetting films which effectively act as micro-lenses over individual objects, and therefore enable significant SNR and contrast enhancement for microscopic imaging of fine spatial features of an object. Wetting film formation protocol that is described below is rather controllable and repeatable; and is therefore quite promising for practical implementations of this microscopy platform even in field settings.

Prior to preparation of wetting films, samples of interest (which were obtained from vendors or cultured in laboratory conditions) were brought to room temperature. *Giardia lamblia* trophozoites were fixed in 5 % Formalin at pH 7.4 - 0.01 % Tween 20 (Waterborne Inc., USA) and dissolved in Phosphate buffered saline (PBS). For the particular case of trophozoites, I used zinc-free pure New Methylene Blue dye (Acros Organics) that is purified with 0.45 μm pore size Syringless Filter (Whatman) for the aqueous staining of the parasites. Frozen semen samples (California Cyrobank, USA) were thawed in 37°C water bath for 10 minutes and then diluted with sperm washing medium (Irvine Scientific, USA). Whole blood samples (UCLA Blood Bank, USA) were incubated in room conditions for 30 minutes to acquire sedimented RBCs. Polystyrene beads were purchased from Thermo Scientific and *E. coli* specimens were cultured in UCLA Biomedical Engineering facility.

In order to form wetting films, the sample of interest is initially dissolved and agitated within 0.1 M Tris-HCl – 10 % PEG 600 buffer (Sigma Aldrich) and is incubated for 30 seconds in room temperature. Using a lab pipette, a droplet of the resulting suspension (~5 μ L) is placed onto a No. 1 glass cover slip (Fisher Scientific, USA) which was previously cleaned using a plasma cleaner (Harrick Plasma). Then, the droplet is wiggled over the cover slip by gentle mechanical vibration for around 60 seconds, forming the thin wetting film over the specimen (see Fig. 5.1(a)). This vibration can be created simply by hand for better control of the droplet movement. It is also important to note that this procedure does not require the precise control of the droplet volume, as the wetting film spread can be easily adjusted depending on the imaging area of the CMOS sensor-array.

For comparison purposes, I also prepared traditional smear samples of *E. coli* and sperm (*without* the formation of thin wetting films) which I used to comparatively demonstrate the improvements of wetting films on the image quality. For preparation of these conventional smears, each specimen was centrifuged for 1 minute at 3000 rpm and 2 μ L of sedimented sample was dropped onto a No. 1 glass cover slip. Another cover slip was then used for smearing the droplet with an angle of ~30 degrees and air dried for ~5 minutes.

5.3 Experimental Results and Discussion

I initially demonstrated the performance of wetting films by lensless holographic imaging of *Giardia lamblia* trophozoites, *E. coli* and human RBCs (see Fig. 5.2). Note that some of the fine morphological features of these objects that typically have dimensions smaller than e.g., ~0.5 μ m (such as the width of trophozoite flagella and the *E. coli* itself) generate relatively weak scattering signals and therefore their contributions to lensfree object holograms are rather limited. However, through the micro-lens effect of these wetting films, the contrast and SNR of

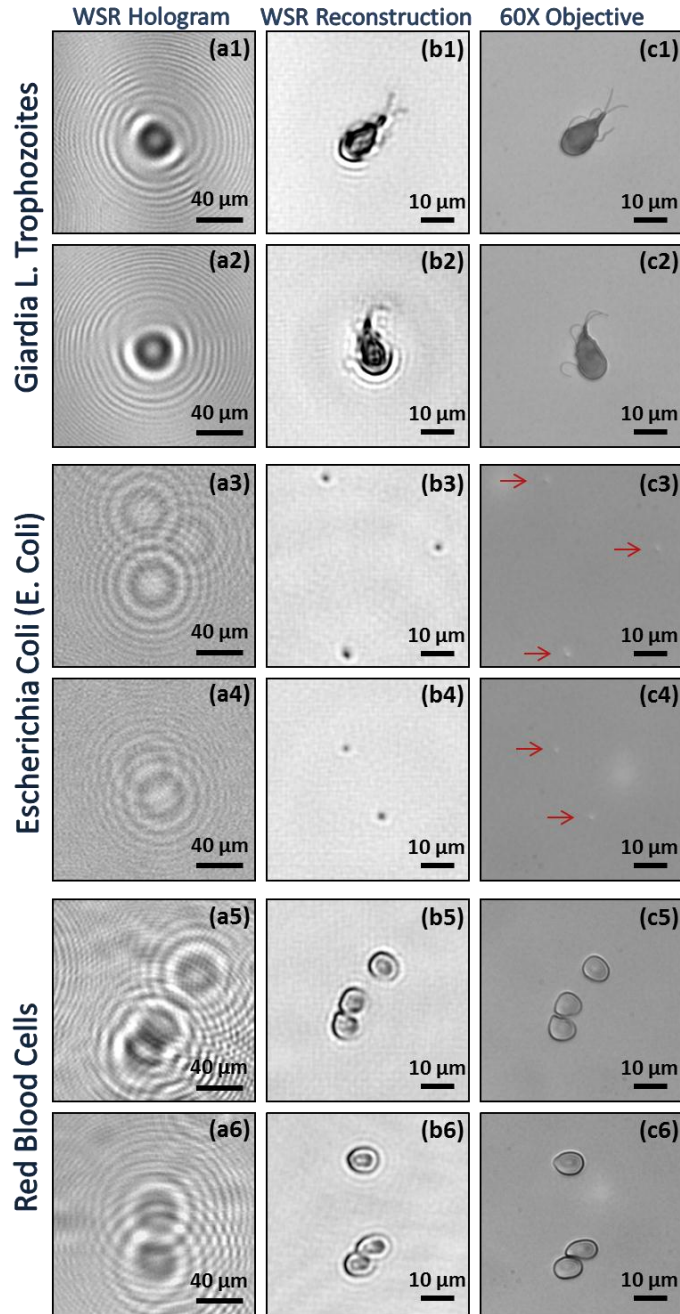


Figure 5.2 (a) Lensfree pixel super-resolution imaging results of Giardia lamblia trophozoites, E. coli and red blood cells are illustrated using thin wetting films (WSR). Digitally recovered super-resolved holograms (1st column) are reconstructed to provide their lensfree microscopic images (2nd column). 60X objective-lens (0.85 NA) bright-field microscope images of the same samples are also provided for comparison purposes (3rd column). Since E. coli samples are relatively faint in their microscope images (due to their weak scattering cross-sections), I used red arrows to point to their locations in microscope comparison images.

the digital holograms of these weakly scattering features were significantly enhanced as shown in Fig. 5.2(a1-a6). As a result, their reconstructed lensfree microscopic images (Fig. 5.2(b1-b6)) successfully revealed finer features of these objects such as the flagella of *Giardia lamblia* trophozoites (Fig. 5.2(b1-b2)) as well as the unique doughnut shape of RBCs (Fig. 5.2(b5-b6)), providing a decent agreement to their corresponding 60X objective-lens (NA=0.85) microscope images (Fig. 5.2(c1-c6)). Note also that bright-field transmission microscope images of *E. coli* samples were particularly faint (even using a 0.85 NA objective-lens) due to their sub-micrometer structure; and therefore I used red arrows to point to their locations (see Fig. 5.2(c3-c4)). The same *E. coli* samples, however, were imaged with a rather strong contrast using the wetting-film based lensfree holographic microscope as illustrated in Fig. 5.2(b3-b4). This relative contrast improvement compared to a regular bright-field microscope is expected since lensfree in-line holography effectively behaves like a phase contrast microscope by indirectly detecting the optical phase information of the specimens in the form of holographic intensity fringes.

Next, to provide a better comparison of the wetting film and its effect on the imaging quality, I conducted experiments on sperm smears that were imaged using lensless pixel super-resolution microscopy with and without the formation of a wetting film (see Fig. 5.3). Without the wetting film, lensfree holograms of sperm samples did not show a major asymmetry in their fringe patterns (see Fig. 5.3(a1-b1)), which is due to the weaker scattering cross-sections of their tails compared to the sperm head. On the other hand, with the formation of the thin wetting film around the sperms, I observed a textural asymmetry on lensfree sperm holograms (e.g., compare Fig. 5.3(a1-b1) with 3(c1-d1)) which reveal the elongated holograms of sperm tails due to the presence of the thin wetting film. The same conclusion was also supported in the reconstructed

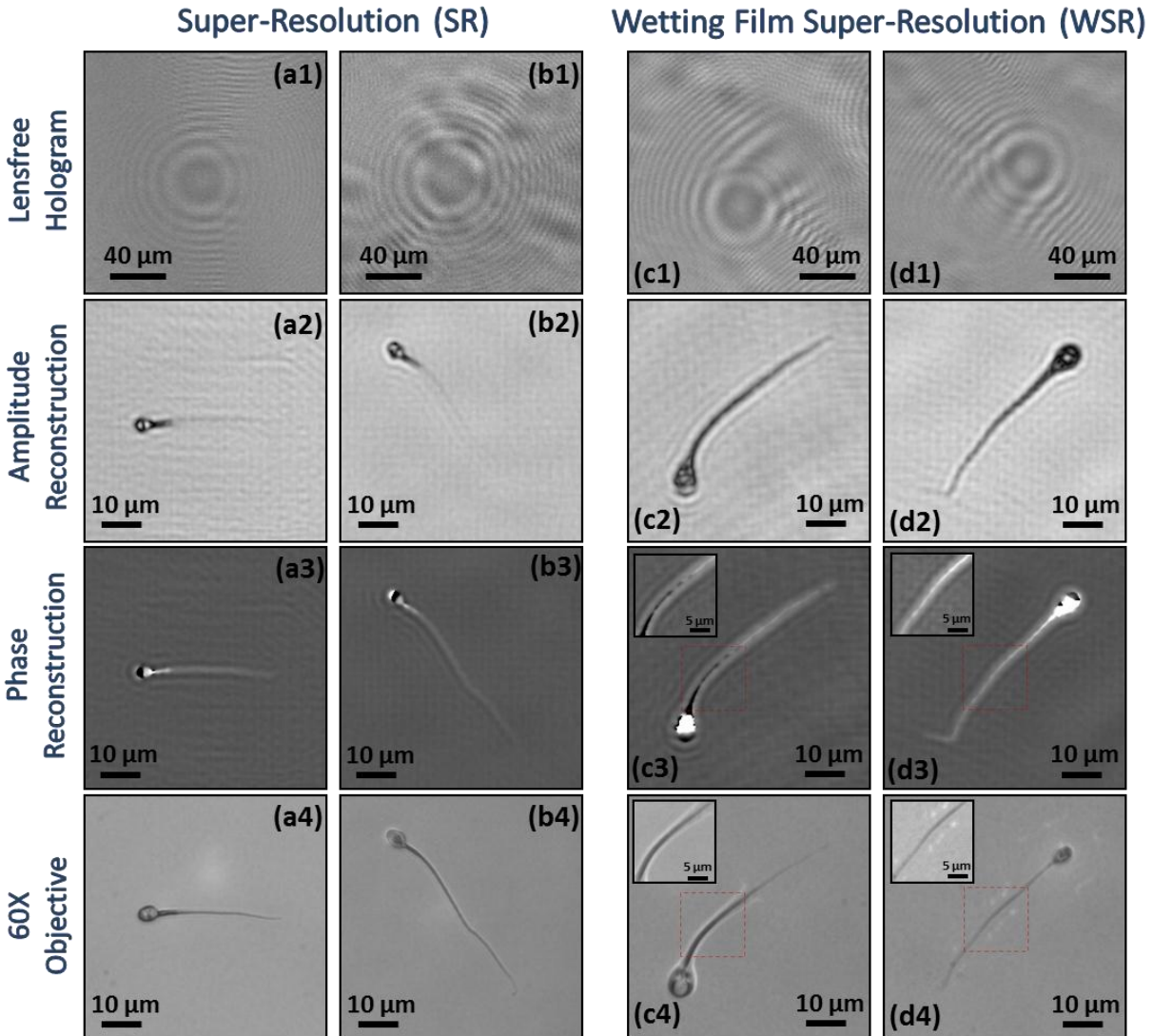


Figure 5.3 (a) Lensfree pixel super Lensfree super-resolution microscopic images of sperm samples are generated using the experimental setup shown in Fig. 5.1 (b and c). Columns (a1-a4) and (b1-b4) are obtained without the use of wetting films, while columns (c1-c4) and (d1-d4) are obtained with the thin wetting films. Significant SNR and contrast improvement in the reconstructed lensfree holographic images is observed with the thin wetting films. For instance, the end of the sperm tail shown in (d4) with an arrow measures $<0.5 \mu\text{m}$ in width, which was faithfully reconstructed using the wetting film based holographic microscope as illustrated in (d2) and (d3). Moreover, as shown in the digitally zoomed-in images (c3 and c4), lensfree phase recovery images revealed both the sperm tails as well as the surrounding wetting film due to the refractive index difference between two regions.

images (see e.g., Fig. 5.3(c2-d2)) such that with the wetting film, the fine morphological features of the sperm tails became much more visible compared to a regular smear without the wetting film (see Fig. 5.3(a2-b2)). As an example, the end of the sperm tail shown in Fig. 5.3(d4) with a red arrow measures $<0.5 \mu\text{m}$ in width, which was faithfully imaged using the wetting film based lensless holographic microscope as illustrated in Figs. 5.3(d2) and 5.3(d3). Although the refractive index difference between the sperm tails and the surrounding medium created a sufficient contrast in the reconstructed phase images for both of the cases (i.e., with or without the use of the wetting film), phase as well as amplitude images of wetting samples were comparatively much better resolved as illustrated in Fig. 5.3. Notice also that the physical existence of the wetting film over the sperm samples was further validated in the phase reconstruction results, showing the tail structure recovered inside the wetting film (see e.g., the digitally zoomed region of interest in Fig. 5.3(c3) inset). The same behavior can be also seen in the corresponding 60X objective-lens image as illustrated in Figure 5.3(c4) and its inset.

An important feature of lensfree holographic microscopy is that by digitally changing the focusing distance (i.e., z_2) different depths within the sample volume can be reconstructed. This feature is illustrated in Fig. 5.4, where for the same sperm sample shown in Fig. 5.3(d2-d3), I show two different reconstruction planes corresponding to $z_2 = 794 \mu\text{m}$ and $778 \mu\text{m}$. Notice that since the wetting film induced micro-lens behaves physically different for the tail and the head of the sperm (due to significant differences in their morphology and size), as expected one can see the tail and the head get in focus at different reconstruction planes (e.g., the tail is in focus at $z_2 = 794 \mu\text{m}$ whereas the head gets in focus at $z_2 = 778 \mu\text{m}$ as illustrated in Fig. 5.4).

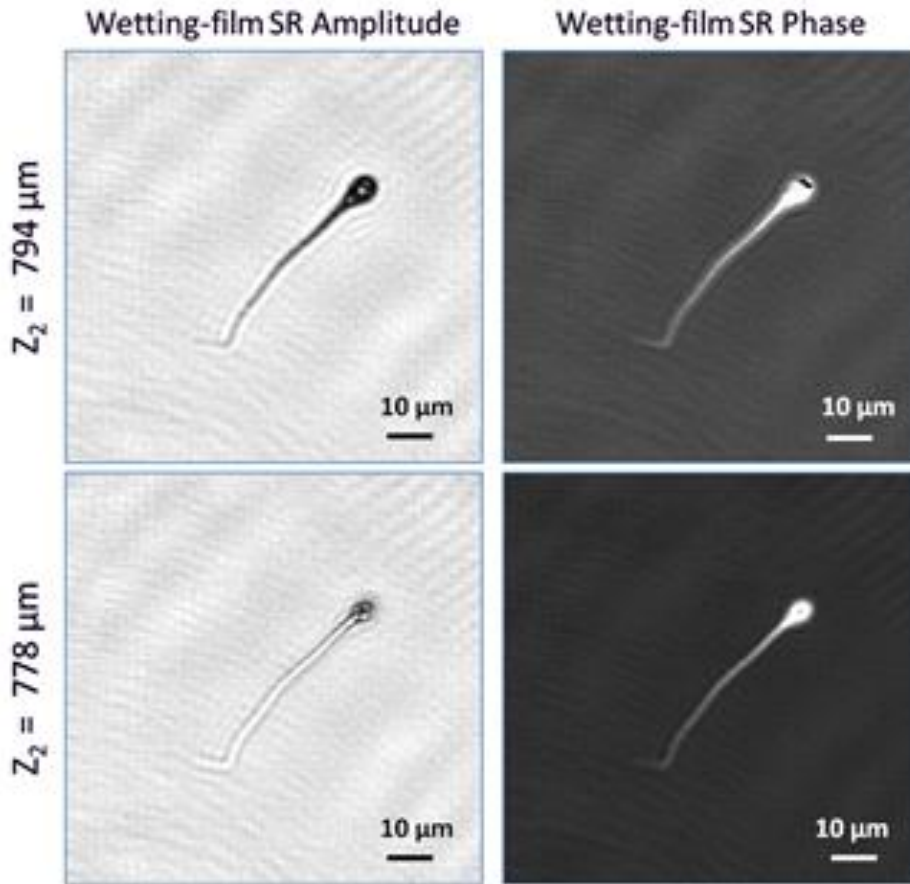


Figure 5.4 By digitally changing the focusing distance (i.e., z_2) different depths within the sample volume can be reconstructed using the lensfree super-resolution (SR) microscope. This feature is illustrated in this figure where for the same sperm sample shown in Fig. 5.3(d2-d3), I show two different reconstruction planes corresponding to $z_2 = 794 \mu\text{m}$ and $778 \mu\text{m}$. Notice that since the wetting film induced micro-lens behaves different for the tail and the head of the sperm (due to differences in their morphology and size), once can see the tail and the head get in focus at different reconstruction planes (e.g., the sperm tail is in focus at $z_2 = 794 \mu\text{m}$ whereas the sperm head gets in focus at $z_2 = 778 \mu\text{m}$).

In order to further investigate the performance improvement of the lensfree microscopy platform due to thin wetting films, I imaged a polystyrene bead of $1 \mu\text{m}$ diameter as well as an E. coli sample with and without the wetting film (see Fig. 5.5). First, notice that without the wetting film, the lensfree super-resolved holograms of these objects did not reveal any “visible”

holographic signatures as illustrated in Figs. 5.5(a1-b1). Despite this fact, their reconstructed holographic images still revealed the weak signatures of these objects as illustrated in Figs. 5.5(a2-b2). With the use of the wetting film, however, the lensfree holograms of these particles showed a significant SNR improvement as illustrated in Figs. 5.5(c1-d1), where the interference

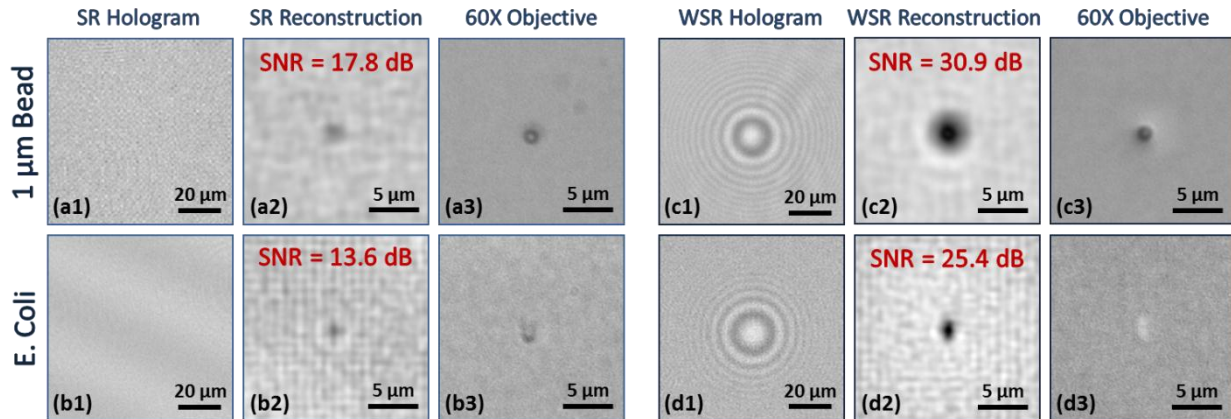


Figure 5.5 1 μm polystyrene bead and E. coli images are illustrated for both cases (Super-resolution only (SR) and Super-resolution using wetting films (WSR)) to quantify the relative SNR improvement. Using the wetting film, SNR increase of up to $\sim 74\%$ and $\sim 87\%$ in logarithmic decibel scale (corresponding to $\sim 352\%$ and $\sim 289\%$ in linear scale) is observed on lensfree amplitude reconstruction images of 1 μm bead and E. coli, respectively (see (a2) vs. (c2) and (b2) vs. (d2)). Also notice that the lensfree super-resolved holograms shown in (a1) and (b1) are not visible to bare eye since their signal intensity is quite weak without the wetting film. Despite this fact, reconstruction of these super-resolved holograms is still feasible as illustrated in (a2) and (b2), respectively.

fringes are rather strong and are visible to bare eye, unlike Figs. 5.5(a1-b1). These improved holographic signatures then translated into much better reconstructed microscopic images as shown in Figs. 5.5(c2-d2). These results demonstrated a significant SNR enhancement of up to $\sim 74\%$ and $\sim 87\%$ in dB (corresponding to $\sim 352\%$ and $\sim 289\%$ in linear scale) on lensfree amplitude reconstruction images of 1 μm bead and E. coli, respectively. These digital SNR values were calculated using the formula: $\text{SNR} = 20\log_{10} |(\max(I) - \mu_0) / \sigma_0|$, where I is the

intensity of the reconstructed image, and μ_0 and σ_0 are the mean and the variance of the background noise region, respectively. Note also that the wetting film based lensfree reconstructed image of *E. coli* (Fig. 5.5(d2)) shows not only a higher contrast and SNR but also the elongated rod-shaped structure of the bacteria is more visible with the wetting film compared to the reconstruction results *without* the wetting film (Figure 5.5(b2)). As I discussed earlier, 60X bright-field microscope comparison images are again quite faint (see e.g., Fig. 5.5(d3)) compared to the holographic reconstruction results.

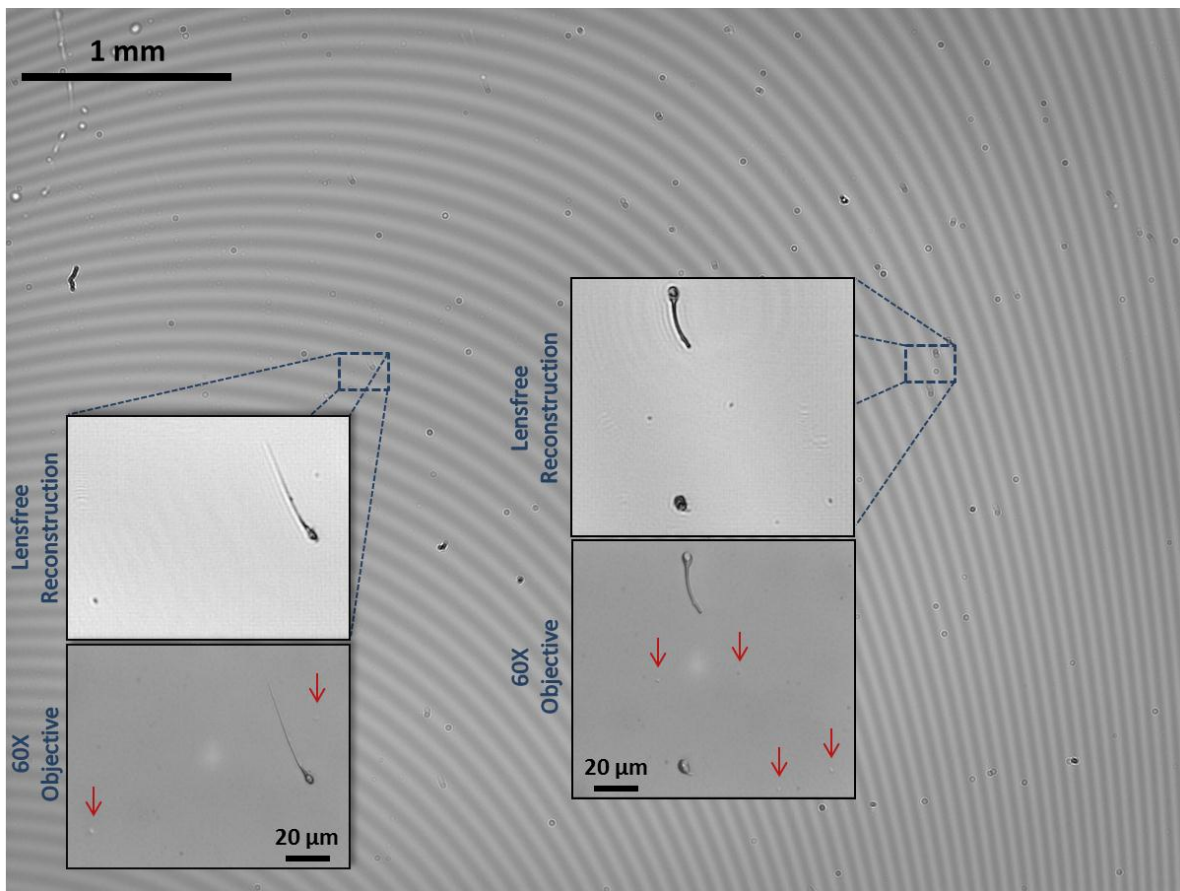


Figure 5.6 Wide-field (FOV $\sim 24 \text{ mm}^2$) high-resolution imaging of a heterogeneous wetting film sample that is composed of *Giardia lamblia* trophozoites, *E. coli* and sperm is demonstrated. This constitutes >100 fold larger FOV, when compared to a bright-field optical microscope using e.g., a 40X objective-lens. For comparison purposes,

conventional bright-field microscope images of zoomed-regions of interest are also provided (60X objective-lens; 0.85 NA), where *E. coli* samples were marked with red arrows due to their faint contrast.

Finally, a full field-of-view (i.e., 24 mm²) lensfree holographic image of a spiked wetting film sample that is composed of *Giardia lamblia* trophozoites, *E. coli* and sperm samples is illustrated in Fig. 5.6 in order to demonstrate the wide imaging area of this on-chip microscopy platform. Considering the additional contrast and SNR improvements due to the micro lens effect of these wetting films, such a high-throughput and high-resolution microscopy platform can be very useful to rapidly evaluate e.g., bodily fluids or water samples even in remote locations or field settings. Moreover, the wetting film formation procedure described here is rather repeatable which makes it applicable even in resource limited environments with relatively low level of training.

In summary, I demonstrated the performance improvement of lensfree on-chip super-resolution microscopy due to wetting film induced micro-lens effect by imaging various micro-objects such as *Giardia lamblia* trophozoites, human sperm, polystyrene beads, *E. coli* as well as RBCs. Experimental results yielded up to 4 fold SNR improvement, showing better recovery of sub-micron features of specimens such as sperm tails and flagella of *Giardia lamblia* parasites. This wetting film approach allows a stable and repeatable micro-lens effect on individual objects to enhance the capabilities of the field-portable lensfree holographic microscopes. Therefore, it may provide a quantitative toolset to carry out highly-sensitive measurements even in resource-limited environments without the need for advanced sample preparation procedures.

Chapter 6 Wide-Field Optical Imaging of Single Nano-Particles and Viruses using On-Chip Microscopy and Self-Assembled Liquid Nano-Lenses

6.1 Introduction

Direct observation of nano-scale objects, e.g., viruses, is a challenging task for optical microscopy because the scattering from an individual nano-particle is typically weak at optical wavelengths. Electron microscopy therefore remains one of the gold standard visualization methods for nano-particles, despite its high cost, limited throughput, and restricted field-of-view. Here I describe a new high-throughput on-chip imaging approach that uses stable and biocompatible wetting films to self-assemble aspheric liquid nano-lenses around individual nano-particles to enhance the contrast between the scattered and the background (unscattered) light. By analytically calculating the three-dimensional geometry of the liquid lens that forms around each nano-particle, the effect of the nano-lens is modeled as a spatial phase mask centered on the particle, which is also confirmed through finite-difference-time-domain (FDTD) simulations. The holographic diffraction pattern of this effective phase mask is then pixel super-resolved in the far-field to directly image, for the first time in on-chip microscopy, individual sub-100 nm particles across a large field-of-view of $>20 \text{ mm}^2$, i.e., more than two orders-of-magnitude larger than other nano-imaging techniques. Such a wide-field on-chip microscopy modality that is capable of directly imaging nano-particles within a field-portable design could especially be important for the detection and enumeration of viruses. As a proof-of-concept demonstration, I also imaged single adenoviruses and influenza A (H1N1) viral particles using the same on-chip

microscopy technique, thus creating new opportunities for rapid medical diagnostics in point-of-care and field conditions.

6.2 Experimental Methods

In this section, I describe the experimental methods and procedures that have enabled high-throughput optical imaging and detection of individual sub-100 nm particles and moderately-sized viruses across an ultra-large FOV of e.g., 20.5 mm² (Fig. 6.1(a)). Unlike some of the advanced imaging modalities,¹⁻³⁰ this technique does not circumvent the optical diffraction limit to boost spatial resolution and therefore cannot serve as a replacement for an ultra-high resolution microscopy modality, but instead it dramatically improves signal-to-noise and contrast to enable nanoparticle detection and imaging over a very large FOV. At the heart of this approach lie two complementary techniques: (1) self-assembled liquid nano-lenses; and (2) lensfree holographic microscopy on a chip. Note here that the term ‘lensfree’ refers to the lack of an ‘imaging’ lens or its equivalent between the sample and the sensor planes, i.e., these self-assembled liquid nano-lenses or the micro-lenses installed on each pixel of an opto-electronic sensor-array are not considered as ‘imaging’ lenses. Using a sample preparation technique that only involves portable equipment and non-toxic chemicals, liquid nano-lenses are assembled around each nano-particle seated on a hydrophilic surface (see Figs. 6.1(b) and (c)). These liquid lenses are composed of a biocompatible buffer that is stable for more than an hour at room temperature without significant evaporative loss. This buffer prevents nano-particle aggregation while also acting as a spatial phase mask that relatively enhances the scattered light from the embedded nano-particle/nano-lens assembly. Liquid film coatings with different compositions and sample preparation methods have been previously used in conjunction with optical microscopy, however these earlier methods employed thick (e.g., ~1 μm) and continuous films,

rather than isolated nano-lenses self-assembled around individual particles, as a result of which they could not enable the detection of single nano-particles that are smaller than $\sim 0.5\text{-}1\ \mu\text{m}$ in width or diameter.^{46,140}

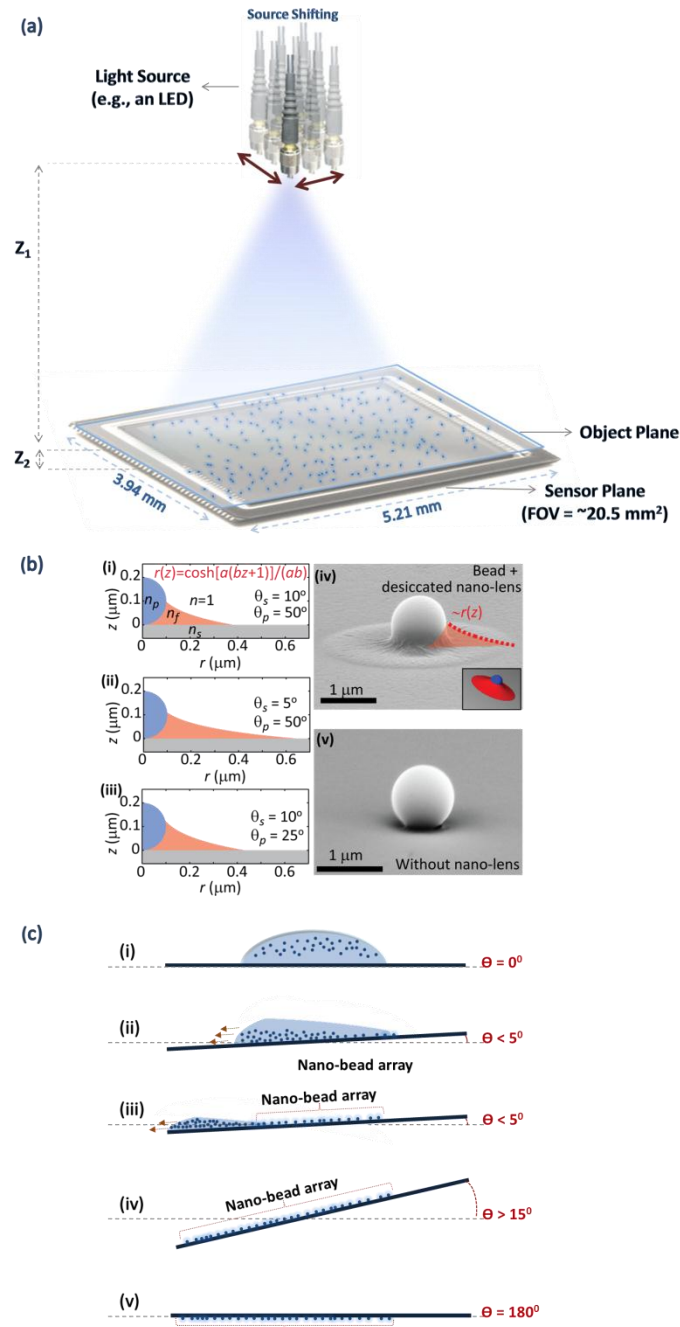


Figure 6.1 (a) Schematic diagram of lensfree pixel super-resolution holography set-up (not drawn to scale). The quasi-monochromatic light source is located at $Z_1 = \sim 8\text{-}12\ \text{cm}$ above the sensor plane, illuminating the sample of

interest (e.g., nano-particles) that is placed very close to the sensor surface (e.g., $Z_2 = \sim 300 \mu\text{m}$). The fiber-coupled source is shifted on a 2D plane (with discrete steps of $\sim 0.1 \text{ mm}$) to create sub-pixel ($< 1.12 \mu\text{m}$) shifts on the detector plane. A pixel super-resolved holographic image is then generated from these sub-pixel shifted lower resolution holographic frames. (b) Self-assembled liquid nano-lens (meniscus) shapes. (i)-(iii) show the theoretical predictions of the meniscus shape for 200 nm polystyrene spheres for different contact angles. (i) corresponds to $\theta_s = 10^\circ$ and $\theta_p = 50^\circ$. In (ii), a smaller substrate contact angle results in greater nano-lens coverage, while in (iii) a smaller particle contact angle results in a thicker nano-lens. (iv) shows an SEM image of a $1 \mu\text{m}$ bead with the residue from the nano-lens that has been desiccated by the SEM sample preparation procedure. The lateral extent of the residue agrees well with the fluid model predictions. The inset shows a cartoon of the 3D FDTD model used in the simulations. For comparison, an SEM image of a regular smear sample (without the nano-lens) of $1 \mu\text{m}$ beads is shown in (v). (c) Sample preparation for the formation of self-assembled liquid nano-lenses is illustrated. After the liquid lenses are formed around individual nano-particles, the sample is stable for more than one hour in ambient conditions without any observable degradation.

One of the most appropriate optical techniques to image such nanoscale phase objects is holography because it converts the phase information into intensity oscillations through a heterodyne detection gain. Therefore, I used partially-coherent lensfree digital in-line holography (see Chapter 2) to sample the interference between the unscattered background light and the far-field diffraction patterns of individual nano-lens/nano-particle complexes using an opto-electronic sensor-array (Fig. 6.1(a)). Since this platform operates under unit magnification without the use of any imaging lenses, its object FOV is equal to the active area of the sensor-array, easily reaching e.g., $20\text{-}30 \text{ mm}^2$ using state-of-the-art CMOS imaging chips that are now commonplace in modern cellphones, or $10\text{-}20 \text{ cm}^2$ with CCD imaging chips.¹⁴⁶ The native resolution of these opto-electronic chips and the signal-to-noise ratio (SNR) of holographically reconstructed images can be further improved by pixel super-resolution techniques.^{21,22,147-149} Here I implement pixel super-resolution through source-shifting⁴⁶⁻⁵¹ as illustrated in Fig. 6.1(a).

This technique captures several lensfree diffraction holograms from the same nano-particle, where the partially-coherent light source is shifted in small increments, on the order of e.g., 0.1 mm. A single pixel super-resolved holographic image is then synthesized from these sub-pixel shifted holograms, and is finally reconstructed to yield phase and amplitude images of the individual nano-particles together with their surrounding self-assembled liquid lenses.

These self-assembled nano-lenses are generated using a sample preparation procedure that is described in Fig. 6.1(c). In the imaging experiments, I worked with concentrated nano-particle solutions (polystyrene beads from Corpuiscular Inc.), as well as cultured influenza A (H1N1) viral particles and adenoviruses, diluted in 0.1 M Tris-HCl with 10% PEG 600 buffer (Sigma Aldrich). I then prepare a hydrophilic substrate by plasma-treating a glass coverslip using a portable and light-weight plasma generator for approximately 5 min, which is a critical step in enabling self-assembled liquid nano-lens formation. Immediately after plasma-treatment, a 5-10 μL droplet of the diluted nano-bead/virus suspension is transferred to the center of the hydrophilic glass substrate (Fig. 6.1(c)-i). The sample is held flat for three minutes to allow for partial sedimentation of the nano-particles, and then tilted with a slope of 3° - 5° , so that gravity slowly drives the droplet toward the edge of the substrate with an average speed of less than 1 mm/s (Fig. 6.1(c)-ii). A sparse monolayer of nano-objects with surrounding liquid lenses remains in the wake of the droplet (Fig. 6.1(c)-iii). Once the droplet reaches the edge of the substrate, the excess fluid is removed by tilting the sample at an angle of 15° - 20° (Fig. 6.1(c)-iv). Following this last step, the nano-particle/virus sample is then flipped 180° and is placed onto a CMOS sensor array for lensfree holographic image acquisition (Fig. 6.1(a) and 6.1(c)-v). At this point, the remaining fluid volume in each nano-lens is so small that its 3D geometry is mainly determined by surface tension, making the effect of the gravity negligible, i.e., this final 180°

rotation step does not affect the nano-lens geometry. The entire sample preparation process takes less than 10 minutes, and is performed without the use of a cleanroom.

After the sample preparation, lensfree holographic super-resolution image acquisition (see Chapter 5) is performed using either only the green pixels of a 16 megapixel color (RGB) CMOS chip or a large area monochrome CCD chip (see e.g., Figs. 6.2-6.5).¹⁴⁶ The sample is illuminated with a quasi-monochromatic fiber-coupled light source located at $Z_1 = 8-12$ cm above the sensor array, as shown in Fig. 6.1(a). For further miniaturization and field portability, the light source can also be a single LED or an array of LEDs, enabling a compact imaging architecture. Because of the small object-to-sensor distance as shown in Fig. 6.1(a) (i.e., $Z_2 \approx 300$ μm), the spatial coherence, temporal coherence, and illumination alignment requirements in the imaging set-up are all relaxed, significantly reducing the speckle and multiple reflection noise artifacts over the entire active area of the CMOS array. On the other hand, because of unit magnification and the finite CMOS pixel size (1.12 μm), individual lensfree holograms are undersampled, partially limiting the achievable spatial resolution and SNR. To mitigate this limitation, I implement a pixel-super resolution technique that digitally merges multiple holographic images that are shifted with respect to each other by sub-pixel pitch distances into a single high resolution image.^{46-51,146} Discrete source shifts of approximately 0.1 mm translate to sub-micron hologram shifts at the detector plane due to the large Z_1 to Z_2 ratio of >200 . These pixel super-resolved high resolution holograms are then used to digitally reconstruct the complex object field at the sample plane using iterative phase retrieval techniques to eliminate twin image noise and obtain higher SNR microscopic images of the sample.^{46-51,146}

The contrast enhancement observed in the imaging results (summarized in the Experimental Results and Discussion section below) due to the formation self-assembled liquid

nano-lenses is also supported by fluid and optical system models. To shed more light on the observations, the shape of the nano-lens meniscus around each nano-particle is modeled using the Young-Laplace equation¹⁵⁰⁻¹⁵³:

$$\Delta p = \rho g h - \gamma \left(\frac{1}{R_1} + \frac{1}{R_2} \right), \quad (1)$$

where Δp is the over-pressure within the meniscus, ρ is the fluid density, g is the gravitational acceleration constant, h is the height of the meniscus, γ is the surface tension, and $(1/R_1)$ and $(1/R_2)$ are the curvatures of the meniscus along its two principal directions. The Young-Laplace equation holds in general at length scales greater than a few tens of nanometers; below this scale, additional forces such as dispersion, van der Waals, steric, or electrostatic forces must also be taken into account.^{153,154}

Equation (1) can be nondimensionalized by the characteristic pressure $\sqrt{\gamma\rho g}$, which presents the capillary length scale $\ell_c = \sqrt{\gamma/(\rho g)}$:

$$\frac{\Delta p}{\sqrt{\gamma\rho g}} = \frac{h}{\ell_c} - \ell_c \left(\frac{1}{R_1} + \frac{1}{R_2} \right). \quad (2)$$

For water, $\ell_c \approx 2$ mm, while for aqueous PEG solutions the surface tension can be a factor of two smaller over a wide range of concentrations with similar density, making the capillary length shorter but still of roughly millimeter length.¹⁵⁵ The overpressure in the film Δp is coupled to the volume of the fluid surrounding the nano-particle, and is determined by the formation process of the liquid nano-lenses. As the fluid slowly drains due to the $<5^\circ$ tilt applied during sample preparation, the sparse nano-particles pin the receding contact line until the surface tension of the fluid in contact with a nano-particle can no longer support the hydrostatic pressure of the deformed contact line, at which point the fluidic bridge between the nano-particle and the bulk

receding contact line ruptures.¹⁵⁶⁻¹⁵⁸ The maximum extent of the contact line deformation before rupture is on the order of the nano-particle size.¹⁵⁹

Therefore the overpressure in the film immediately before and after rupture is on the order of $\rho g R_p$, which makes $\Delta p / \sqrt{\gamma \rho g}$ of order $R_p / \ell_c \approx 10^{-4}$. Note also that the gravitational term h / ℓ_c is of the same order. However, the curvature terms are of order $\ell_c / R_p \approx 10^4$. From this scaling analysis, this analysis is found to be in the low Bond number limit where only the curvature terms are significant.¹⁵¹ It is important to note that this approximation, $\Delta p \approx 0$, neglects the rapid rupture process, where the fluid bridge pinches off and additional overpressure may be introduced. However, quantifying this effect requires numerical fluid dynamic simulations¹⁵⁹⁻¹⁶⁰ that are beyond the scope of the presented work; and more importantly, with the $\Delta p \approx 0$ approximation, a good agreement to the nano-particle imaging experiments (presented in the Experimental Results and Discussion section below) is observed.

Under these assumptions, the Young-Laplace equation (1) reduces to finding a surface with zero net curvature. In cylindrical coordinates, this can be written as,¹⁵¹

$$0 = \frac{1}{R_1} + \frac{1}{R_2} = \frac{r''}{(1 + r'^2)^{3/2}} - \frac{1}{r\sqrt{1 + r'^2}}, \quad (3)$$

where $r = r(z)$ is the radial coordinate of the meniscus at an elevation z above the substrate, and primes indicate derivatives with respect to z . The general solution to this nonlinear second-order ordinary differential equation can be written as a hyperbolic cosine:

$$r(z) = \frac{1}{ab} \cosh[abz + 1]. \quad (4)$$

I refer to this last equation as the ‘‘Nano-lens Equation’’, which is used to determine the 3D geometry of the self-assembled liquid lens around each nano-particle. In this equation, a and b

are constants that are determined by the contact angle at the particle (θ_p), the contact angle at the substrate (θ_s), as well as the particle radius R_p , i.e.,

$$a = -\operatorname{arcsinh}(\cot \theta_s), \quad (5)$$

$$b = \frac{1}{z_0} \left[\frac{1}{a} \operatorname{arcsinh} \left(\frac{\beta(z_0) \cos \theta_p - \sin \theta_p}{\cos \theta_p + \beta(z_0) \sin \theta_p} \right) - 1 \right], \quad (6)$$

where z_0 is the elevation of the meniscus-particle contact line and $\beta(z_0)$ is defined as,

$$\beta(z_0) = \frac{R_p - z_0}{\sqrt{R_p^2 - (R_p - z_0)^2}}. \quad (7)$$

The elevation z_0 of the contact line can be determined by numerically solving the following transcendental equation derived from the intersection between the spherical particle surface and the meniscus shape, resulting in:

$$(\cos \theta_p + \beta(z_0) \sin \theta_p) \left[\operatorname{arcsinh} \left(\frac{\beta(z_0) \cos \theta_p - \sin \theta_p}{\cos \theta_p + \beta(z_0) \sin \theta_p} \right) - a \right] = \frac{R_p}{2 R_p - z_0}. \quad (8)$$

The particle diameter R_p linearly scales both the height and lateral extent of the meniscus, but does ‘not’ affect its shape or aspect ratio. Although both θ_s and θ_p influence all aspects of the meniscus shape, θ_s most significantly affects the radial extent of the meniscus, while θ_p moderately affects its thickness.

Some representative solutions of the nano-lens equation (4) for different contact angles are shown in Fig. 6.1(b) i-iii. The measured contact angle of a ~ 1 mm radius droplet on a plasma-treated glass coverslip is $\theta_s = 10^\circ$, and the measured contact angle on a polystyrene surface is $\theta_p = 50^\circ$. I use these macroscopic contact angles as nominal values for the microscopic system in Fig. 6.1(b)-i since the contact angles cannot be directly measured at this size scale. Small variations in contact angles can affect the aspect ratio of the meniscus, as

illustrated in Fig. 6.1(b) ii and iii, but do ‘not’ alter its general shape. The scanning electron microscopy (SEM) image shown in Fig. 6.1(b)-iv is typical of the nano-lens after it has been desiccated by the vacuum required in SEM sample preparation. Although the original shape of the liquid film has not been preserved due to vacuum, it is clear that the liquid residue from the film only extends a distance on the order of the particle diameter, in good agreement with the model predictions (e.g., see the curve in Fig. 6.1(b)-iv).

6.3 Experimental Results and Discussion

In order to investigate the holographic imaging performance improvement due to formation of self-assembled liquid nano-lenses on single nano-particles, I have conducted various imaging experiments for the detection of single 60-400 nm beads and viruses (i.e., adenoviruses and influenza A (H1N1)).

As shown in Figs. 6.2-6.5, utilizing self-assembled nano-lenses on lensfree holographic imaging enables wide field detection of nano-scale objects even at distant regions on the sensor-arrays. In Fig. 6.2, I have used a CMOS imager (Sony RGB sensor, 1.12 μm pixel size) for the lensfree detection of heterogeneous sample of nano-scale particles over an imaging FOV of $>20 \text{ mm}^2$ (5.2 mm x 3.9 mm) and acquired corresponding SEM images of the same sample to verify the lensfree experimental results. The effect of the number of holographic frames used for pixel super-resolution on the contrast and SNR of the nano-particle images is characterized in the lower set of panels in Fig. 6.2. In these experiments, various lensfree holographic images of 95 nm beads were reconstructed from pixel super-resolved images synthesized using e.g., 1, 4, 8, 16, 36 and 64 sub-pixel shifted holographic frames, respectively. Reconstruction of a single lensfree frame did not provide any satisfactory result for imaging of these 95 nm particles, whereas increasing the number of holographic frames employed in the pixel super-resolution

algorithm significantly enhanced the contrast and the SNR of individual nano-particles, as illustrated in Fig. 6.2.

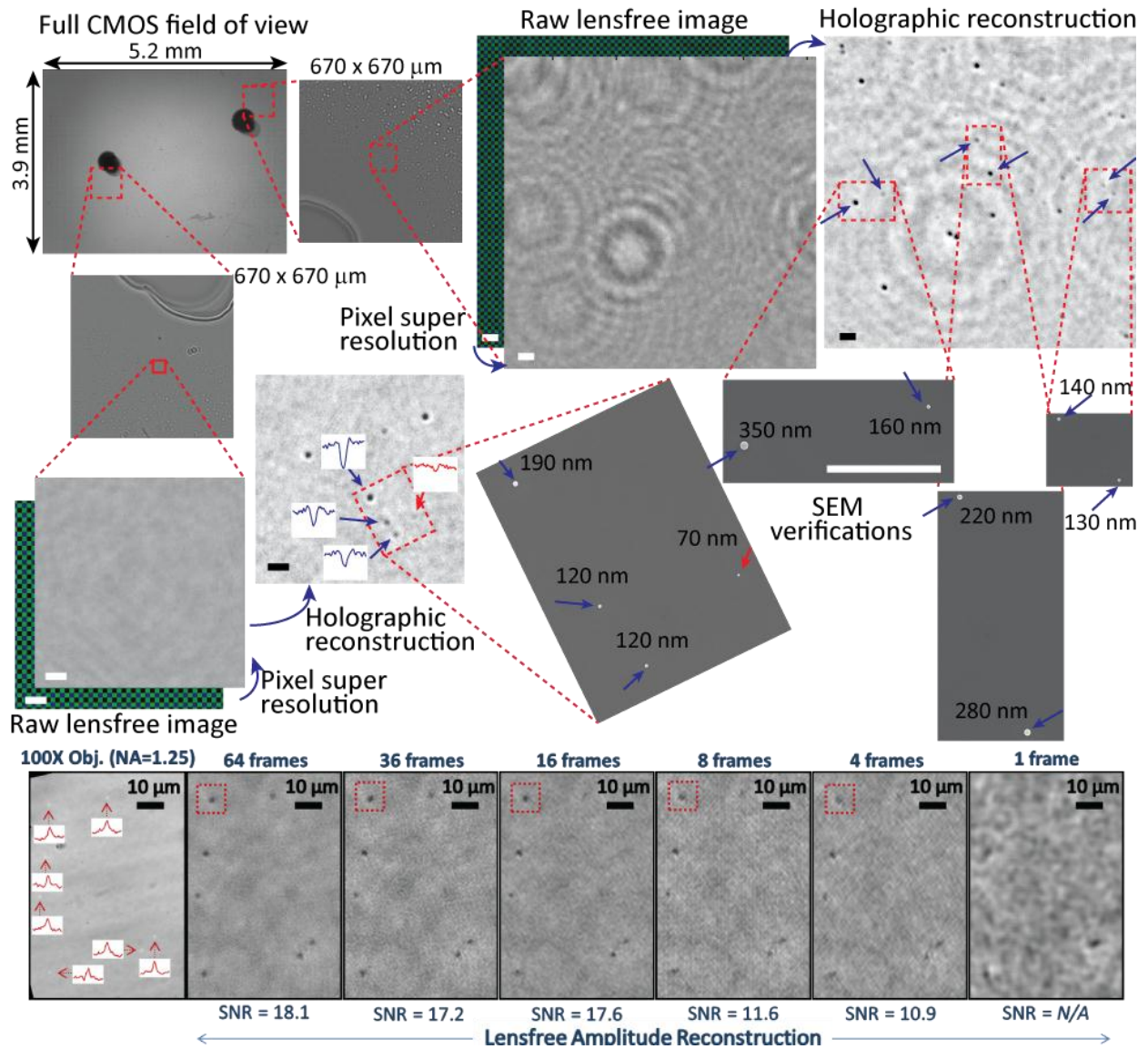


Figure 6.2 The upper set of panels shows regions of interest from opposite sides of the CMOS chip. The black marks within the FOV are placed to ease finding the corresponding SEM images of the nano-particles. Raw lensfree Bayer-pattern RGB images are converted into high-resolution monochrome holograms via pixel super-resolution. Reconstructing the holographic images enables the detection of nanoparticles, as verified by scanning electron microscopy (SEM). The lower set of panels shows the improvement of the contrast and SNR of the reconstructed 95 nm particles by the lensfree pixel super-resolution technique. Even with nano-lenses, individual beads cannot be

discerned using a single lower resolution lensfree holographic image; however, increasing the number of frames used in pixel super-resolution sufficiently improves the contrast and SNR of the reconstructed amplitude images such that individual 95 nm beads can be detected using nano-lenses. I have chosen a single 95 nm bead (shown within the red dotted square) and quantified this SNR enhancement, revealing that ≥ 16 sub-pixel shifted lensfree frames is sufficient to observe individual sub-100 nm particles using nano-lens based holographic imaging. A corresponding bright-field oil-immersion objective-lens (100X, NA=1.25) image of the same sample, with insets of cross-sections of individual nano-particles is also shown for comparison. Scale bars in the upper set of panels are 5 μm ; all SEM images are at the same scale.

In Fig. 6.3, additional lensfree reconstruction that was digitally cropped from a much larger field of view (i.e., $> 20 \text{ mm}^2$ – active area of the CMOS sensor-array) and corresponding SEM verifications from the same heterogeneous nano-bead sample as in Fig. 6.2 are shown.

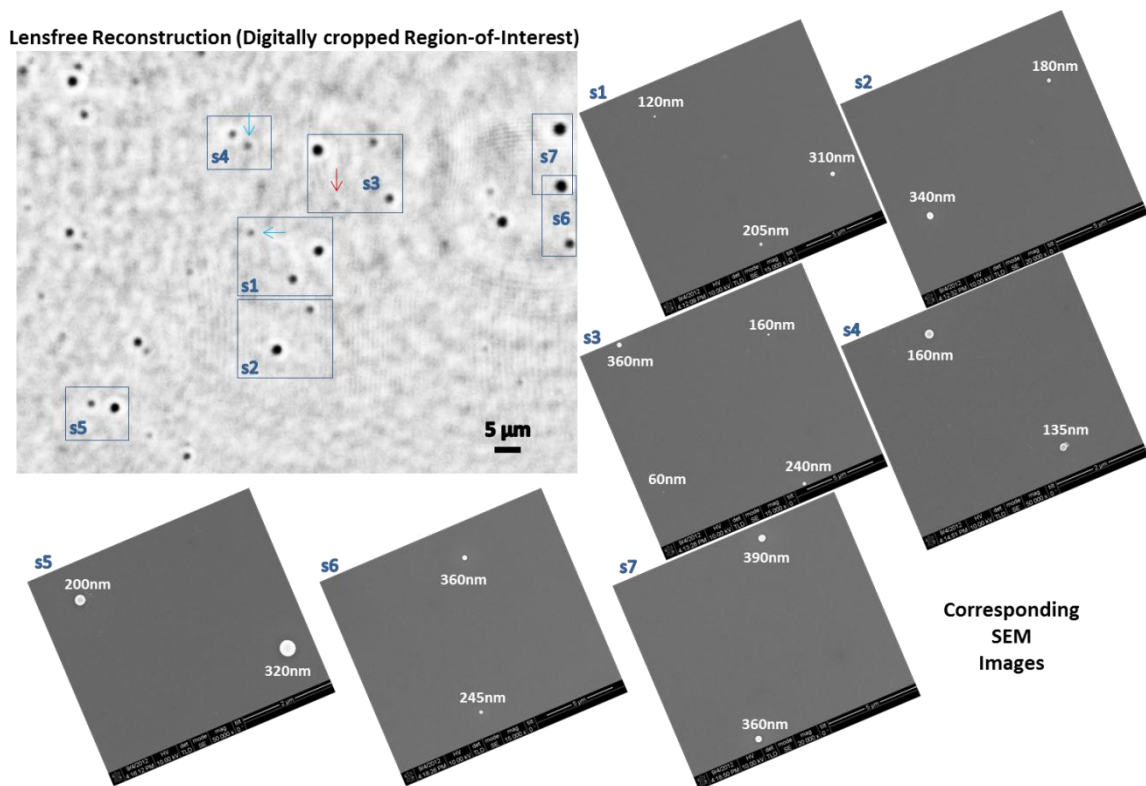


Figure 6.3 Additional reconstructions and corresponding SEM verifications from the same nano-bead sample as in Fig. 6.2 are shown. Red arrows are used to locate the $\leq 100 \text{ nm}$ beads, whereas blue arrows point out the beads

having diameters between 100 nm and 150 nm. Please also note that the lensfree reconstructed image was digitally cropped from a much larger field of view (i.e., $> 20 \text{ mm}^2$ – active area of the CMOS sensor-array).

In Fig. 6.4, I illustrate the lensfree imaging of 200 nm particles over a wide FOV of 37 mm x 25 mm, that is approximately one-half of the active area of a 39 megapixel CCD chip (KAF-39000, Kodak, 6.8 μm pixel size). This FOV is more than 45 fold larger than the CMOS sensor-array used in Fig. 6.2. However the larger pixel size, i.e., 6.8 μm (CCD) vs. 1.12 μm (CMOS), also makes it more challenging to detect the lensfree signatures of nano-particles.

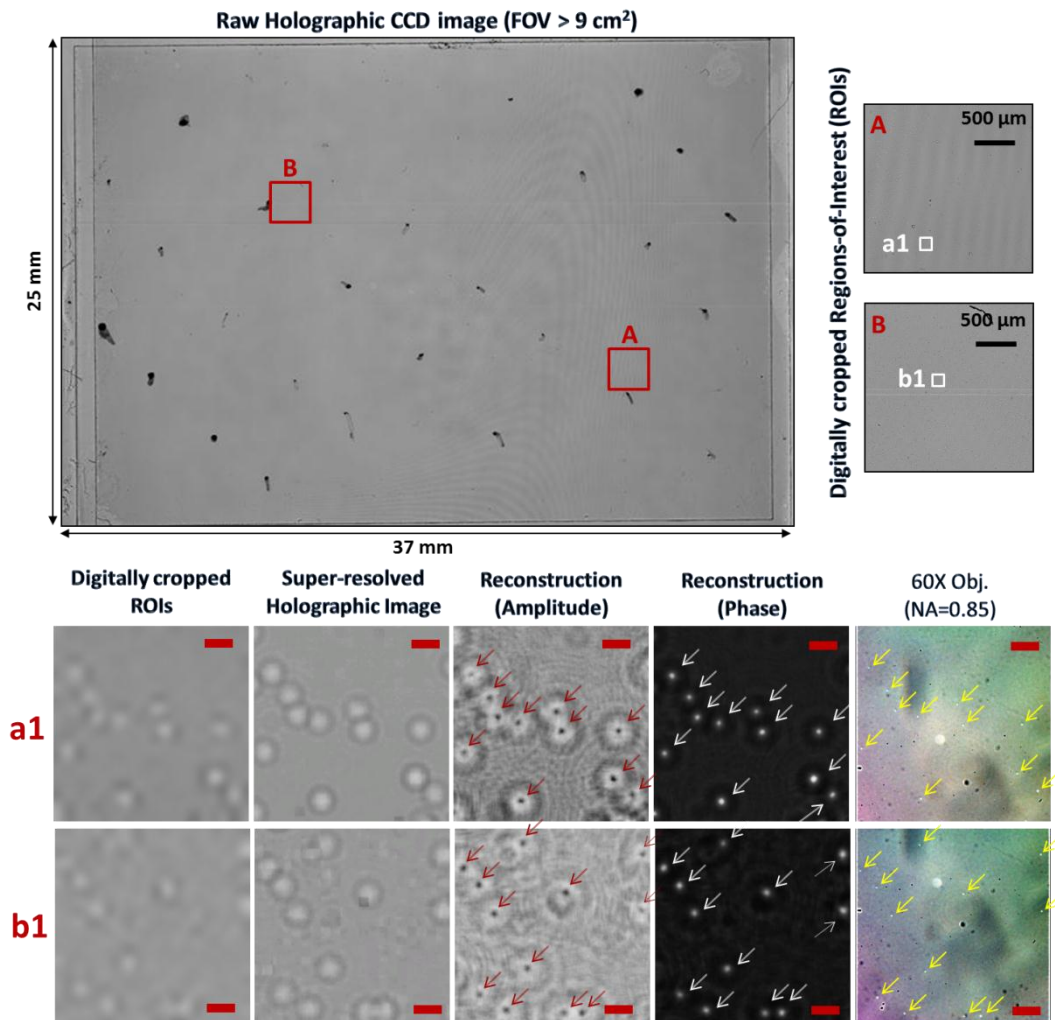


Figure 6.4 Ultra-wide field CCD-based lensfree imaging results of 200 nm particles using self-assembled nano-lenses are shown. The black marks within this FOV (top left) are placed to ease finding the corresponding 60X

objective lens (NA=0.85) images of the nano-particles. The reconstruction process here is similar to that used with the CMOS sensor with minor adjustments because the CCD is monochrome, while the CMOS has a Bayer color pattern. The implementation of pixel super-resolution results in an effective pixel count of more than 0.75 gigapixels across this FOV. a1 and b1 were digitally cropped from A and B, respectively, which were also cropped from the much larger image FOV (37 mm x 25 mm). Lensfree raw holographic images as well as their pixel super-resolved counterparts for a1 and b1 are shown together with their amplitude and phase reconstructions. Iterative twin image (TI) elimination algorithm described in Chapter 2 was utilized to suppress the TI noise of reconstructed particles. Arrows point out the locations of 200 nm particles in holographic reconstructions as well as their corresponding objective lens images. Note that some of the stationary particles visible in microscope comparison images are located on the objective lens, not on the samples. Red scale bars in a1 and b1 are 20 μm .

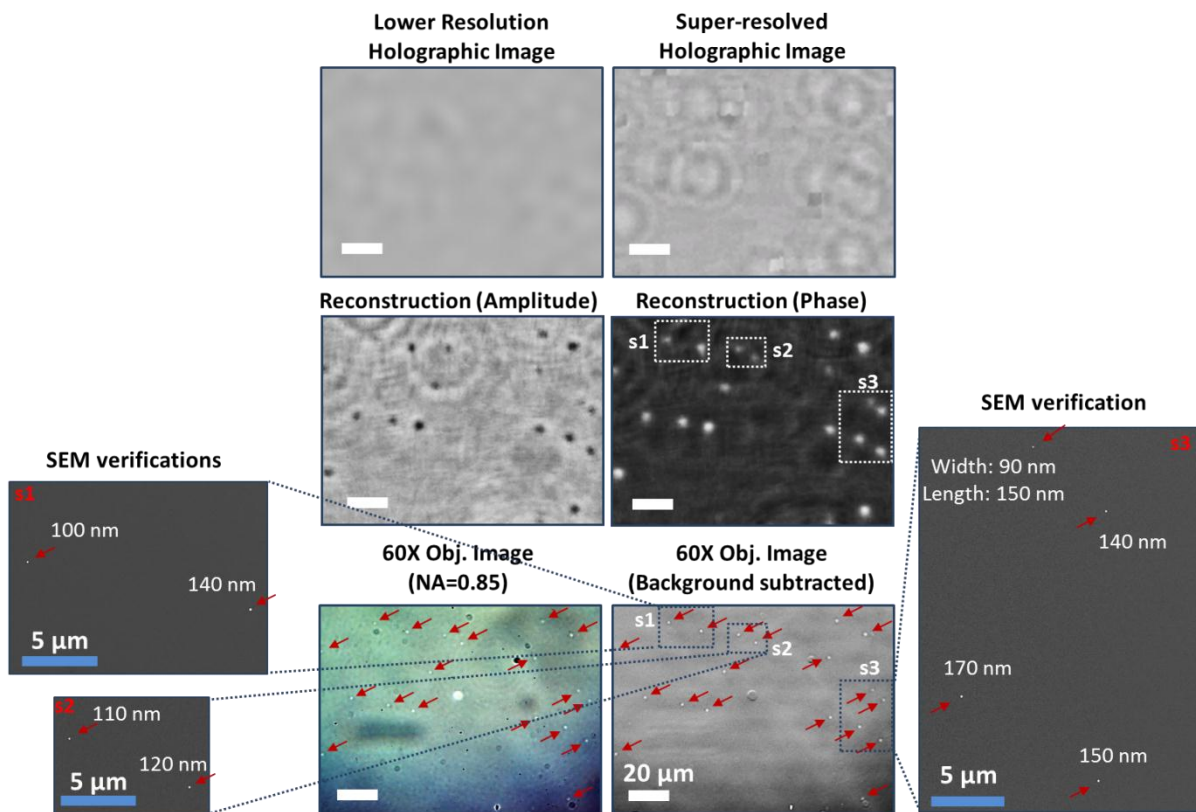


Figure 6.5 CCD-based lensfree imaging results of 100-150 nm particles using self-assembled nano-lenses are shown. Same as in Fig. 6.4, some of the stationary particles visible in the microscope comparison image are located on the objective lens, not on the samples. To digitally clean such objective lens artifacts, I also show a background

subtracted microscope image to better illustrate the locations of the nanoparticles on the sample, providing a decent match to the lensfree reconstructions. SEM comparisons are also provided for some of the particles within the same field of view; unless otherwise mentioned, all the numbers noted in these SEM images refer to the diameter of the corresponding nanoparticle. White scale bars: 20 μm ; Blue scale bars: 5 μm .

Similar to Fig. 6.4, in Fig. 6.5, various nanoparticles with sizes ranging between 100 nm and 150 nm are imaged using a wide-field CCD chip (KAF-39000, Kodak, 6.8 μm pixel size, full field-of-view: $\sim 18 \text{ cm}^2$). The much larger pixel size ($\sim 6.8 \mu\text{m}$) when compared to the CMOS imager ($\sim 1.1 \mu\text{m}$) makes it more difficult to detect individual nano-particles; however, the reconstructed images, especially the phase image, provide a decent contrast. Please also note that the reconstruction process utilized in CCD based lensfree experiments is similar to that used with the CMOS sensor with minor adjustments because the CCD is monochrome, while the CMOS has a Bayer color pattern.

The combination of self-assembled liquid nano-lenses and holographic computational on-chip microscopy enables the detection of individual sub-100 nm particles (see Figs. 6.2 and 6.3) that are not visible with holographic imaging techniques alone, and have extremely low contrast even under conventional oil-immersion objective-lenses e.g., with a numerical aperture (NA) of 1.25. As an example, I demonstrate in Fig. 6.6 that without the liquid nano-lenses, neither 198 nm nor 95 nm diameter polystyrene beads provide a signal above the background noise level in the lensfree holographic imaging setup. However with the formation of the above discussed nano-lenses, these nano-particles become clearly visible in both phase and amplitude reconstructions as illustrated in Fig. 6.6 (also see Figs. 6.2 and 6.3). Both with and without the liquid lenses, the presence of the nano-particles on the substrate is confirmed in these experiments using oil-immersion bright-field microscopy, although the contrast and SNR of

these images are rather low despite the use of a high power objective-lens (100X, NA = 1.25 – see Fig. 3). On the other hand, using lensfree on-chip imaging, the contrast of the same nanoparticles are significantly improved (Fig. 6.6) after the formation of the nano-lenses, which act as spatial phase masks enhancing the diffraction holograms of individual nano-particles.

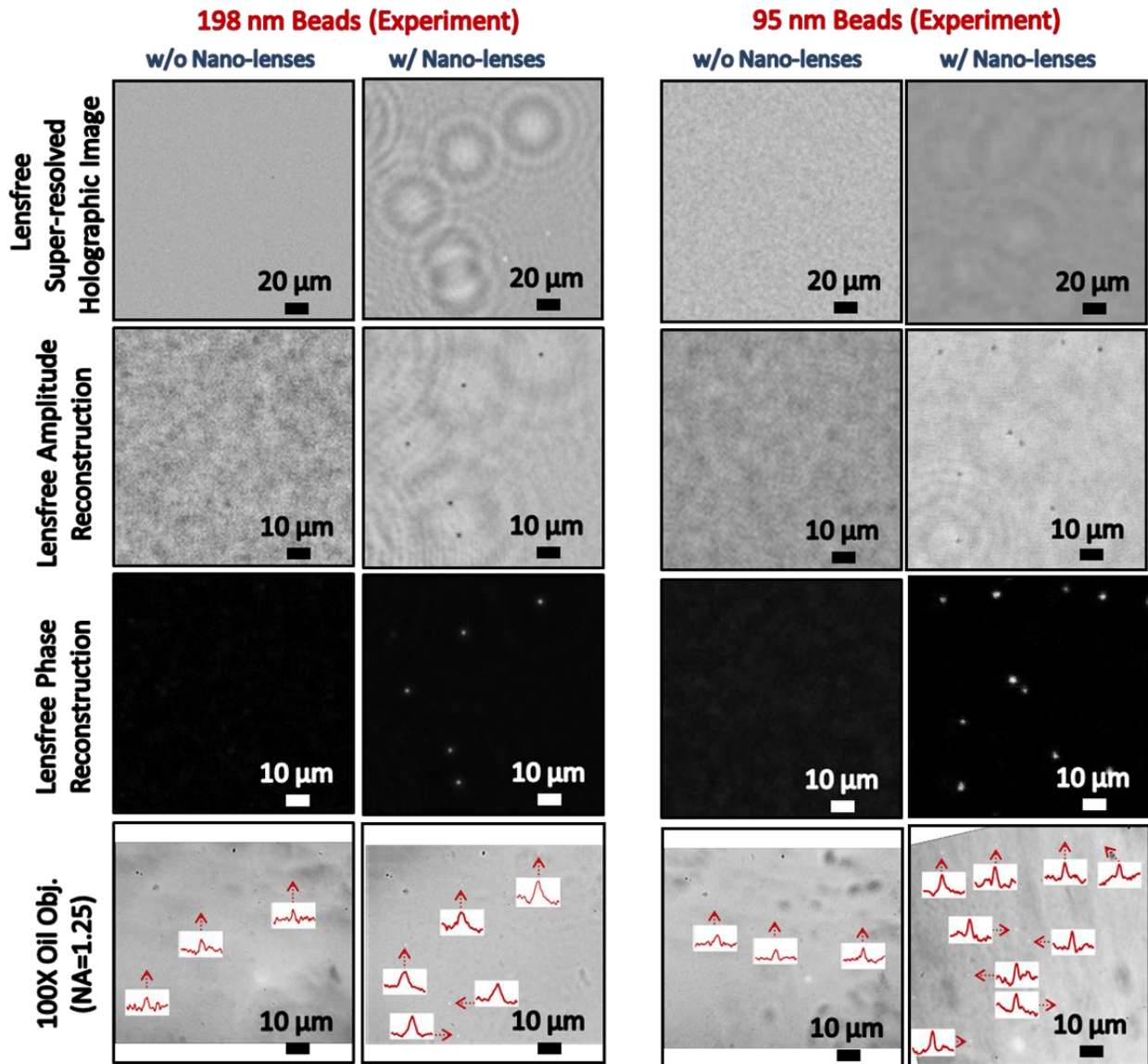


Figure 6.6 Lensfree holographic imaging results of 198 nm and 95 nm polystyrene beads with and without self-assembled liquid nano-lenses are illustrated. Neither 198 nm nor 95 nm beads can be detected with lensfree on-chip imaging using regular smears (i.e., without the formation of liquid lenses). In contrast, the formation of liquid nano-

lenses enabled the reconstruction of lensfree amplitude and phase images of both 198 nm and 95 nm beads. Nano-lens based holographic images are in a good agreement with 100X (NA=1.25) oil-immersion objective images of the same samples. In these bright-field oil-immersion microscope images, however, the contrast is relatively poor, and intensity cross-section curves of individual nano-beads are shown in insets to aid in locating these beads. The holographic images shown here are digitally cropped from much larger FOV of $>20 \text{ mm}^2$.

In order to evaluate the optical effects of each nano-lens on the recorded lensfree holograms of the nano-particles, two numerical models are employed: (1) a finite-difference time-domain (FDTD) simulation followed by Rayleigh-Sommerfeld wave propagation; and (2) a thin-lens model followed by Rayleigh-Sommerfeld wave propagation (Also see Experimental Methods section). In the FDTD model (see Fig. 6.1(b)), I simulate the particle ($n_p = 1.61$)¹⁶¹, the nano-lens ($n_f = 1.35$)¹⁶², and the substrate ($n_s = 1.52$) within a simulation volume of $20 \times 20 \times 5 \text{ }\mu\text{m}$, calculating the amplitude and phase of the transmitted optical field $3 \text{ }\mu\text{m}$ beyond the glass-air interface, i.e., no evanescent waves are considered as the detection occurs beyond the near-field. These results are then substituted at the center of a larger ($100 \times 100 \text{ }\mu\text{m}$) homogeneous field (i.e., uniform plane wave) that is numerically propagated a distance of $297 \text{ }\mu\text{m}$ (i.e., $Z_2 - 3 \text{ }\mu\text{m}$), resulting in a simulated lensfree diffraction hologram. In the thin lens model, however, 3D scattering is ignored and represent the particle and its surrounding nano-lens as a single 2D phase-only object whose phase delay as a function of radial coordinate is the free-space wavenumber k_0 times the line integral of the optical path length in z through the entire depth of the materials at that coordinate. For both of these optical models, the nano-lens equation (4) of Experimental Methods section, described above, is used to estimate the 3D geometry of the liquid lens that forms around each nano-particle. FDTD and thin-lens model simulation results for a 95 nm particle with surrounding nano-lens are illustrated in Fig. 6.7.

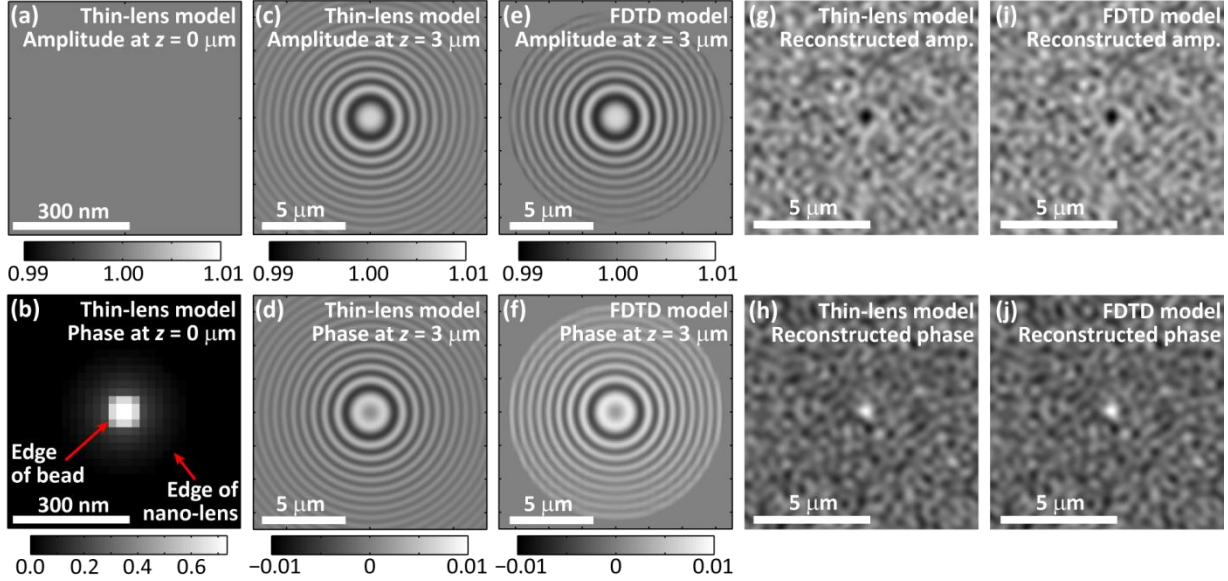


Figure 6.7 (a) Under the thin-lens model, the object does not introduce any amplitude modulation. (b) The large phase modulation from the bead and the more subtle modulation from the surrounding nano-lens are indicated. A 20 nm grid resolution is used to numerically model the system. (c) and (d) Amplitude and phase of the thin-lens object after a free-space propagation of 3 μm . (e) and (f) FDTD-modeled amplitude and phase recorded 3 μm after the glass-air interface, within the air gap between the sample and the sensor. Because of the limited FDTD domain, the fields are truncated at a radius of 6.5 μm . Within this region, there is very good agreement between FDTD and the thin-lens models. (g-j) Simulated amplitude and phase reconstructions from the two models agree very well. These reconstructions are obtained by propagating the fields to $z = 300 \mu\text{m}$, adding Gaussian noise with standard deviation 1% of the mean hologram intensity, quantizing to 10-bit intensity levels, downsampling to a super-resolved pixel size of 0.28 μm , and finally back-propagating -300 μm to $z = 0 \mu\text{m}$.

To provide a fair comparison to the experimental imaging results, numerically generated lensfree holograms are downsampled to a super-resolved effective pixel size (i.e., 0.28 μm); and then randomly generated Gaussian noise is added to each hologram, and the pixel values to 10-bit levels are quantized. In Fig. 6.8, these numerically-generated noisy holograms are used to attempt to reconstruct 95 nm particles with and without nano-lenses. For both the FDTD and thin-lens models, the nano-lenses significantly improve the image contrast such that the nano-

particle can be clearly distinguished from the background noise in both the amplitude and phase reconstructions. Without the liquid nano-lens, however, the same numerical models reveal that the signature of the 95 nm particle is effectively lost within the background noise (see Fig. 6.8), also agreeing with the experimental observations in Fig. 6.6.

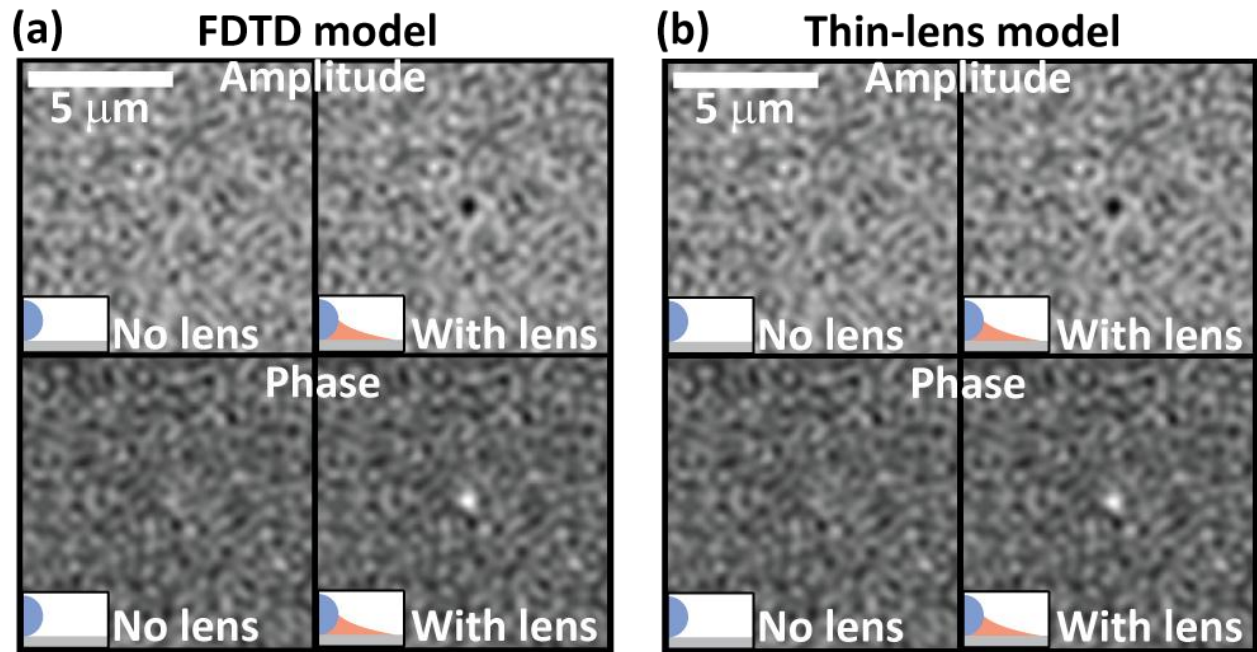


Figure 6.8 In (a), the results of an FDTD simulation are holographically propagated and then reconstructed, while in (b) the thin lens model is used to generate the holograms. The holographic imaging system is simulated using a super-resolved pixel size of 0.28 μm. Both amplitude and phase reconstructions are shown in each case, where the nano-particle is located at the center of the frame. The standard deviation of the Gaussian noise added to the holograms is 1% of the mean hologram intensity.

A more detailed comparison between the experimental and theoretical nano-lens phase functions is illustrated in Fig. 6.9, which provides an independent verification of the nano-lens shape predicted by the theoretical analysis.

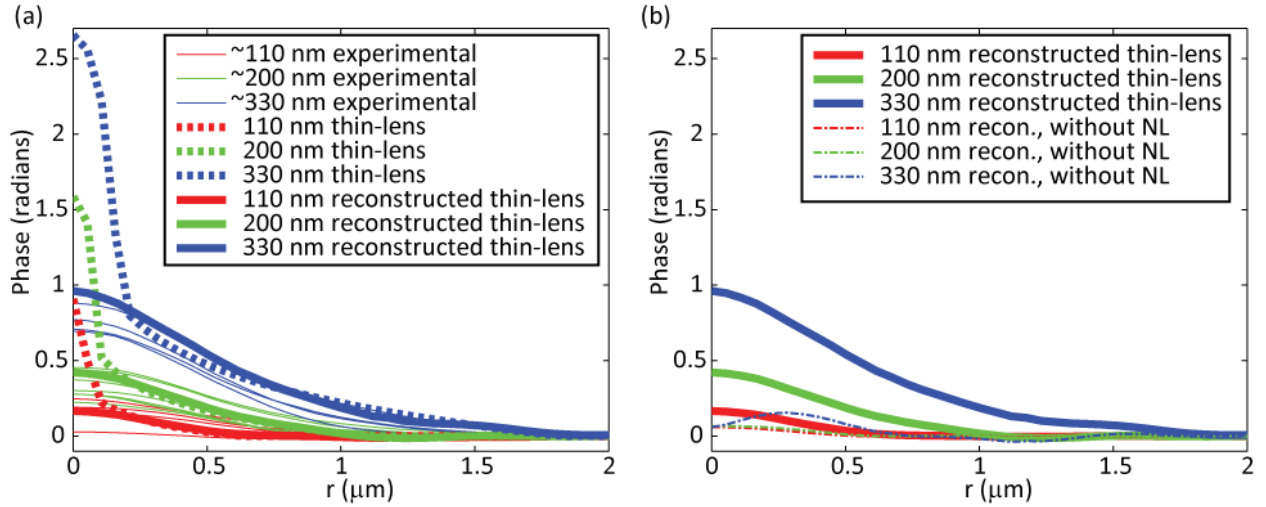


Figure 6.9 (a) shows the comparison between the experimentally reconstructed phase profiles (thin lines) and two different models (thick lines), based on the SEM bead size measurements in Fig. 6.3. Beads in the range 60 nm to 140 nm (mean value 110 nm) are colored red. Beads in the range 160 nm to 245 nm (mean value 200 nm) are colored green. Beads in the range 310 nm to 360 nm (mean value 330 nm) are colored blue. Thick dashed lines show the thin-lens phase profile predicted by the Nano-lens Equation (Eq. 4 in Experimental Methods) using contact angles $\theta_p = 50^\circ$, $\theta_s = 2.5^\circ$ (θ_s is an adjustable parameter here, but is consistent with the very small macroscopic contact angle measured using a sessile drop). Thick solid lines show the theoretically propagated and reconstructed thin-lens phase profiles. Propagation and reconstruction (solid lines) reduce the axial phase value when compared to the Nano-lens equation (thick dashed lines) near the center of the particle due to diffraction; however, the phase profiles in the wings of the nano-lenses are maintained as illustrated in this figure. The theoretically predicted reconstructions agree well with experimental curves, validating the mathematical form of the Nano-lens Equation (Eq. 4 in Experimental Methods). (b) shows a comparison between the theoretically propagated and reconstructed bead + nano-lens profiles from (a) (solid thick lines) and the much weaker theoretically propagated and reconstructed profiles for beads alone “without” the nano-lenses (thin dot-dashed lines).

Furthermore, a numerical study of the effects of the nano-lens film properties (such as refractive index, extinction coefficient, substrate contact angle) is also presented in Fig. 6.10, shedding more light on the detection limits of this approach.

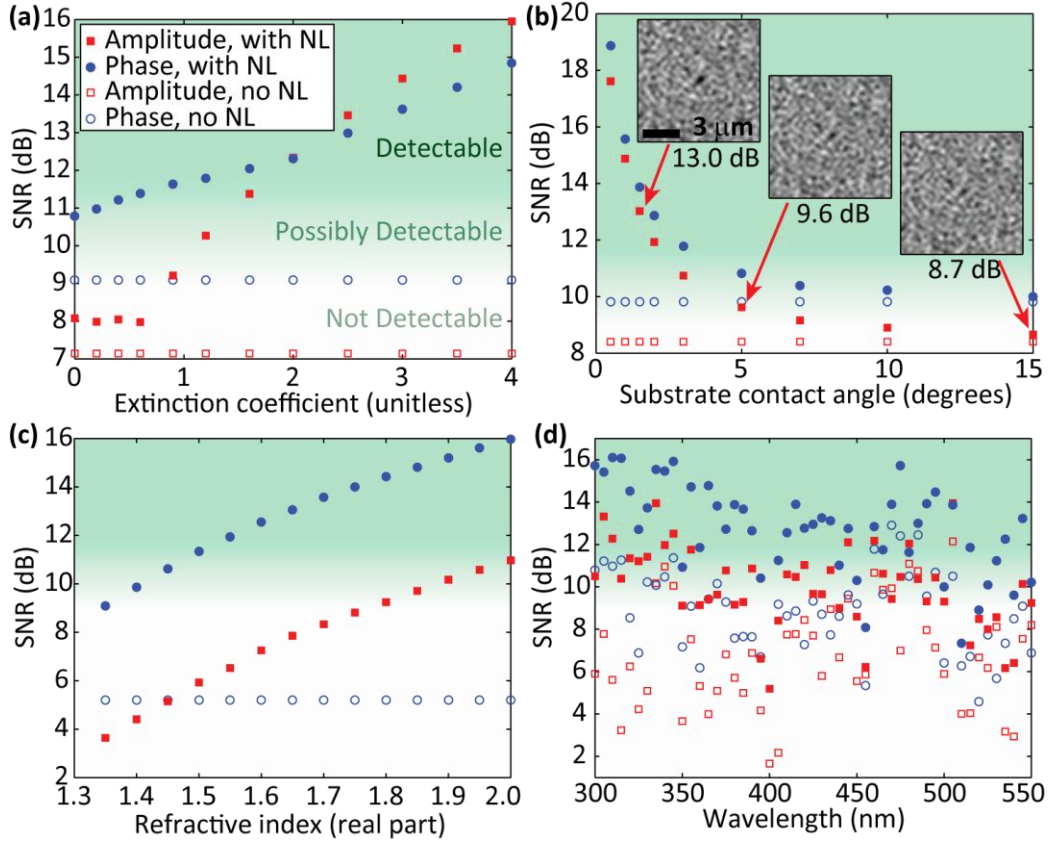


Figure 6.10 (a) Nano-lenses composed of absorbing or scattering films can increase the signal-to-noise ratio (SNR), making particles with surrounding nano-lenses (NL) easier to detect via both amplitude and phase reconstructions. (b) When the nano-lens is more wetting (smaller contact angle), larger lenses form, making particles easier to detect. (c) Higher refractive nano-lenses generate a stronger signal, making particle detection easier. All amplitude reconstructions without nano-lenses show $\text{SNR} < 2\text{ dB}$ here. (d) Shorter wavelength illumination provides better SNR on average due to improved resolution. Background shading indicates particle detectability with a detection threshold between 9 and 12 dB. The insets in (b) show the amplitude reconstructions for three points in the vicinity of this detection threshold. (a) and (b) assume a polystyrene particle size of 50 nm, while (c) and (d) assume a particle size of 75 nm. For all data in a given subplot, randomly-generated 1% Gaussian noise field is added at the holograms. In (a-c), this noise field results in identical noise fields at the reconstructed image plane and therefore smooth curves, as the reconstruction distance ($z_2 = 100 \mu\text{m}$ here) and wavelength ($\lambda = 480 \text{ nm}$) are the same for each data point. In (d), however, the wavelength is different for each data point, resulting in different reconstructed noise fields and the large scatter in SNR. Unless a parameter is being explicitly varied, all simulations assume a purely real film refractive index of 1.35, and a substrate contact angle of 10° .

Finally, using the same lensfree imaging platform, I demonstrated computational on-chip imaging of single H1N1 virus particles and sub-100 nm adenoviruses (see Fig. 6.11). Different super-resolved holographic regions of interest were digitally cropped from a much larger FOV (20.5 mm^2) for these virus samples, and were then digitally reconstructed to yield both lensfree amplitude and phase images of the viral particles. For comparison, 100X oil-immersion objective (NA=1.25) and SEM images of the same samples are also shown, matching very well with the reconstructed images.

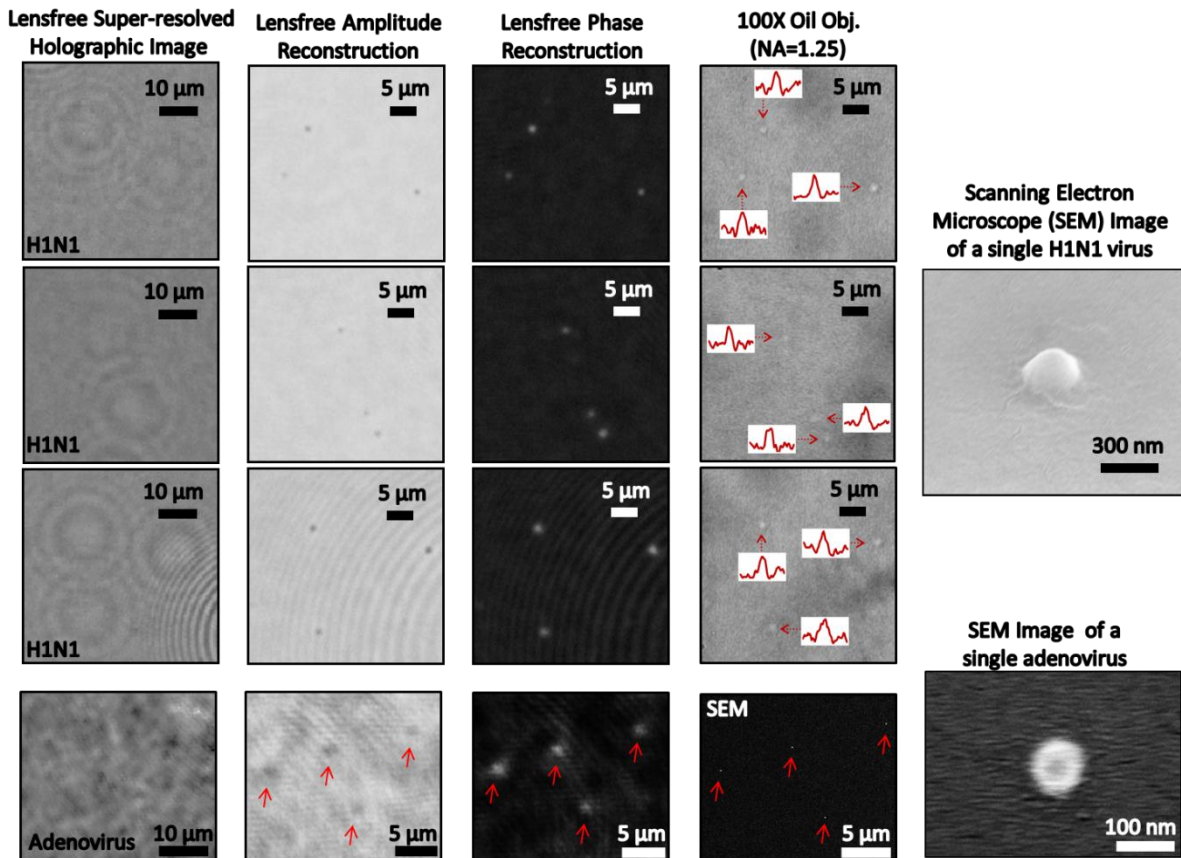


Figure 6.11 Lensfree pixel super-resolved holographic images of individual influenza A (H1N1) viruses and adenoviruses (digitally cropped from a wide FOV of $>20 \text{ mm}^2$) are illustrated. Corresponding bright-field oil-immersion objective-lens (100X, NA=1.25) images of the same samples, with insets of cross-sections of individual viruses are also shown for comparison. Since adenoviruses could not be observed under 100X oil-immersion optical microscopy, SEM was instead used for verification of the field of view. Holographic fringes for adenoviruses are not

clearly visible due to the weak signatures of these sub-100 nm particles. A tilted SEM image of a single H1N1 virus surrounded by a liquid nano-lens is also shown, as is a normal-incidence SEM image of a single adenovirus. Due to the vacuum involved in sample preparation prior to SEM imaging, the liquid lenses are desiccated in these SEM images.

In summary, this computational on-chip imaging technique presented in this chapter can detect individual sub-100 nm particles and viruses across an ultra large FOV of 20.5 mm^2 , i.e., more than two orders-of-magnitude larger than other nano-imaging techniques. Through a wetting film based method that induces self-assembled liquid nano-lenses around individual particles, I reconstruct both amplitude and phase images of single nano-particles that were otherwise undetectable with on-chip microscopy. The enhancement provided by the self-assembled nano-lenses is well-understood via analytical models of the liquid meniscus shape and numerical models of its contribution to the optical diffraction signal. These results are very promising to provide e.g., a highly-sensitive and high-throughput medical diagnostics and screening platform, especially for field settings and resource-limited environments.

Chapter 7 Conclusion

For decades optical microscopy has been the workhorse of various fields including engineering, physical sciences, medicine and biology. Despite its long history, until relatively recently, there has not been a significant change in the design and working principles of optical microscopes. Over the last decade, motivated partially by the quest to better understand the realm of the nano-world, super-resolution techniques started a renaissance for optical microscopy by addressing some of the most fundamental limitations of optical imaging such as the diffraction limit.¹⁻³⁰ This recent progress in microscopy utilized various innovative technologies to overcome the fundamental barriers in imaging and has created significant excitement in a diverse set of fields by enabling new discoveries to be made. However, together with this progress, the overall complexity and the cost of the optical imaging platform relatively increased which limits the wide spread use of some of these advanced optical imaging modalities beyond well-equipped laboratories.

In the meantime, we have been also experiencing a rapid advancement in digital technologies, with much cheaper 2D solid state detector arrays having significantly larger areas with smaller pixels, better dynamic ranges, frame rates and signal to noise ratios, as well as much faster, cheaper and more powerful digital processors and memories. This on-going digital revolution, when combined with advanced imaging theories and numerical algorithms, also creates an opportunity for optical imaging and microscopy to face another dimension in this renaissance towards simplification of the optical imaging apparatus, making it significantly more compact, cost-effective and easy to use, potentially without a trade-off in its performance. As described in detail in this dissertation, lensfree holographic on-chip imaging can be considered to

be at the heart of this new opportunity and when combined with the advanced state of the art and cost-effective nature of digital electronics, it can provide a transformative solution to some of the unmet needs of cell biology and medical diagnostics especially for resource-limited environments.

Meanwhile, the massive volume of wireless phone communication brings an enormous cost-reduction and unprecedented levels of access to cellphones despite their sophisticated hardware and software capabilities. Quite importantly, most of these existing cellphones are already equipped with advanced digital imaging and sensing platforms that can be utilized for various health monitoring applications Utilizing this advanced state-of-the-art of the cellphone technology towards medical diagnostics, imaging and/or sensing applications can offer numerous opportunities to improve health care especially in the developing world where medical facilities and infrastructure are extremely limited or even do not exist. For this revolution in health care to occur, lab-on-a-chip systems that can potentially be miniaturized to the level of a handheld wireless unit are needed. Ideally, such systems should better be compatible with the existing designs of cellphones, which will make their wide-spread use in the developing world much more cost-effective. In order to complement the efforts centered on this vision, in this dissertation, I have demonstrated the compact, light-weight and cost-effective lensfree stand alone and cell-phone microscopes as well as cell-phone based smart rapid diagnostics test reader. These telemedicine microscopes and diagnostics platforms provide an alternative diagnostics toolset which may be especially useful for healthcare delivery to resource-limited settings and contribute to our combat against global health challenges.

In addition, I have also demonstrated a new lensfree nano-particle imaging modality, which is capable of directly imaging nano-particles within field-portable designs, providing a

highly-sensitive and high-throughput toolset for rapid medical diagnostics and screening especially for resource-limited regions of the world. This computational microscopy and nano-particle imaging platform directly images, for the first time in on-chip microscopy, single sub-100 nm particles (e.g., viruses) using self-assembled aspheric liquid nano-lenses around individual nano-particles across a large field-of-view of $>20 \text{ mm}^2$, i.e., more than two orders-of-magnitude larger than existing nano-imaging techniques.

Creating new opportunities for rapid medical diagnostics in point-of-care and field conditions, this lensfree microscopy and nano-particle imaging toolset may bring improved healthcare delivery especially to resource-poor regions of the world and may significantly benefit our fight against various global health challenges including HIV, malaria, waterborne diseases and viral infections.

Appendix: Smart Rapid Diagnostics Test Reader running on a Cell-Phone for Real-time Mapping of Epidemics

Early evaluation of infectious diseases is essential to prevent the long-term effects of emerging public health threats and to reduce disease burden. For this end, lateral flow immuno-chromatographic tests or Rapid-Diagnostic-Tests (RDTs) provide emerging tools to screen infectious diseases even in resource limited settings or remote locations where conventional approaches (e.g., clinical examination, standard lab-tests and microscopy, etc.) are limited or even not available. Penetration of RDT technologies to public health endeavours has generated several advantages including, but not limited to, better patient management where the infection symptoms are not specific to a particular disease (i.e., asymptomatic diseases), efficient surveillance of outbreaks in high-risk endemic areas, and wide-spread health care delivery by minimally trained technicians.¹⁶³⁻¹⁷⁰

In parallel to the development of various RDTs, the current status of wireless telecommunication technologies exhibits a promising potential to be utilized for healthcare applications even in the least developed parts of the world. This existing wireless telecommunication infrastructure, and in particular cellphones, may provide stimulating opportunities to transform our global fight against e.g., infectious diseases, creating new avenues for cloud-based health monitoring & management platforms.

Toward the same broad goal, here I demonstrate a compact and cost-effective RDT reader platform installed on a cellphone that can work with various lateral flow immuno-chromatographic assays and similar tests to sense the presence of a target analyte in samples.¹⁷¹ This RDT reader attachment, weighing ~65 grams, includes an inexpensive

plano-convex lens, three light-emitting diode (LED) arrays, and two AAA batteries (see Fig. A.1). Installed at the back of the existing camera unit of a cellphone, this mechanical attachment allows digital acquisition of images (in reflection or transmission) of an RDT of interest. These raw images are then processed in real time through a custom-developed application/software running on the cellphone to generate an automated report that consists of test validation and reading of the diagnostic results as well as quantification of the test lines' colour intensities (see Fig. A.2 and A.3).

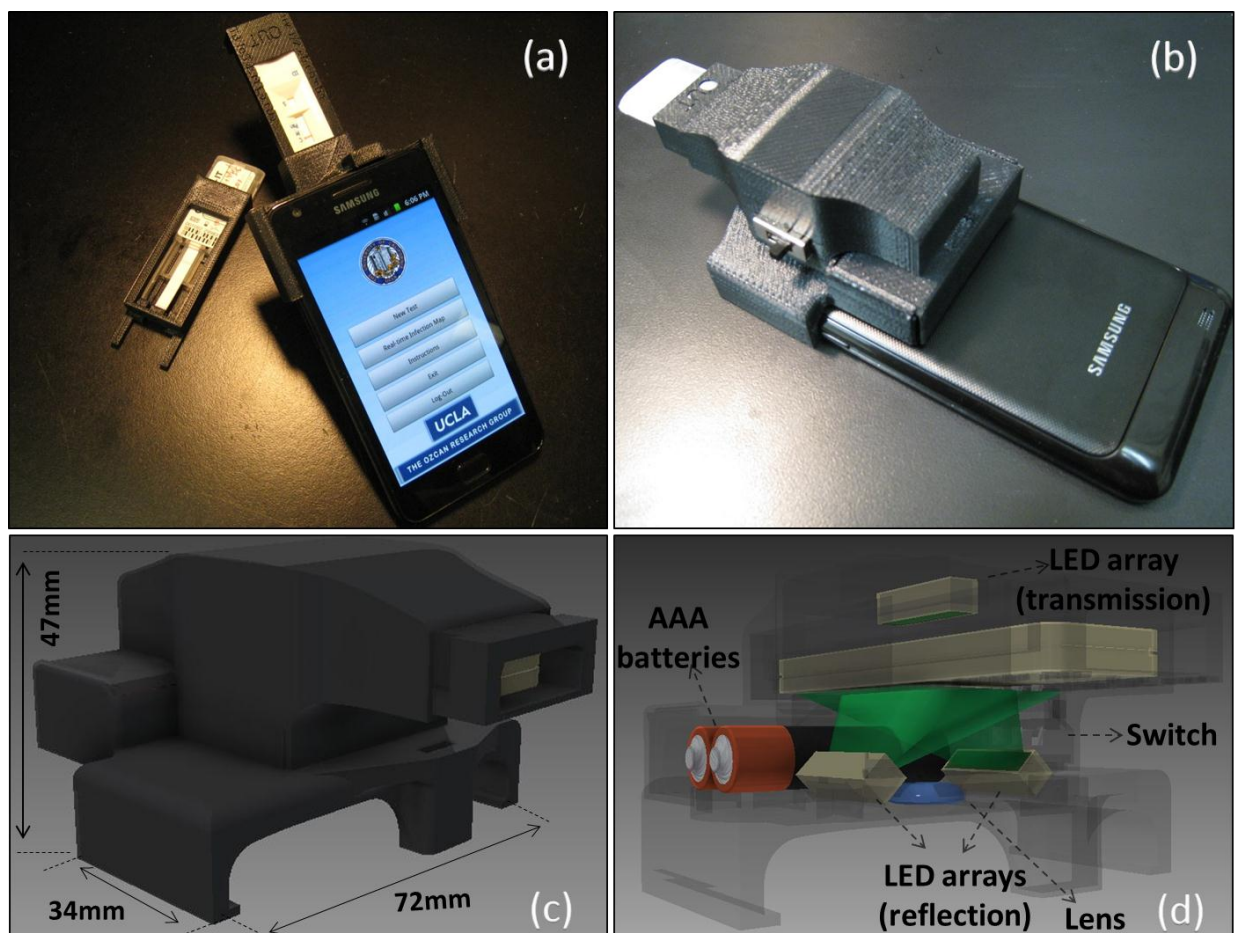


Figure A.1 (a-b) Different views of the smart RDT reader prototype installed on an Android phone (Samsung Galaxy S II). This light-weight (65 grams) and compact attachment can be repeatedly attached/detached to the cellphone body without the need for fine alignment and modification. To accommodate various RDT types using the same base attachment, customized sample trays are used. (c-d) Schematic diagrams of the designed optical RDT

reader attachment are shown. It utilizes three LED arrays with diffusers to ensure uniform illumination of the tests which are loaded to the attachment with customized trays. Two of the LED arrays are located underneath the RDT tray to illuminate it for reflection imaging, whereas a third LED array is used for top illumination to record transmission images of the same RDT. Powered by two AAA batteries, reflection and transmission illumination LED arrays are controlled manually by a physical switch located on the side of the attachment or digitally through the audio jack of the cellphone device (if available). Depending on the format of the diagnostic test, users can switch between the two illumination schemes (reflection vs. transmission) to acquire an image of the RDT with high contrast. This image is then rapidly processed within less than 0.2 sec/image through a custom-developed application running on the cellphone (see Fig. A.2) to generate an automated report that consists of test validation and reading of the diagnostic results as well as quantification of the test lines' color intensities.

This cellphone based RDT reader is also wirelessly integrated into a global database/server to store and organize its diagnostic results/reports and related data (e.g., RDT images, demographic data, test lot ID, etc.). The resulting spatio-temporal map of various RDTs (see Fig. A.4) can then be viewed and shared using internet browsers or through the same cellphone application connecting to the central server (protected by password), which can be quite useful for short- and long-term monitoring of temporal and spatial evolution of various infectious diseases or conditions that can be diagnosed and monitored through RDTs. It is also important to emphasize that size of the entire data package for each test (including the diagnostic report, digitally processed RDT image, patient information, etc.) to be sent from the cellphone to the server is less than 0.05 MBytes such that it does not put a major burden on the network. In case of poor wireless connectivity, these digital test reports are also stored locally at the cellphone memory to be automatically uploaded to the central servers when wireless connection becomes available.

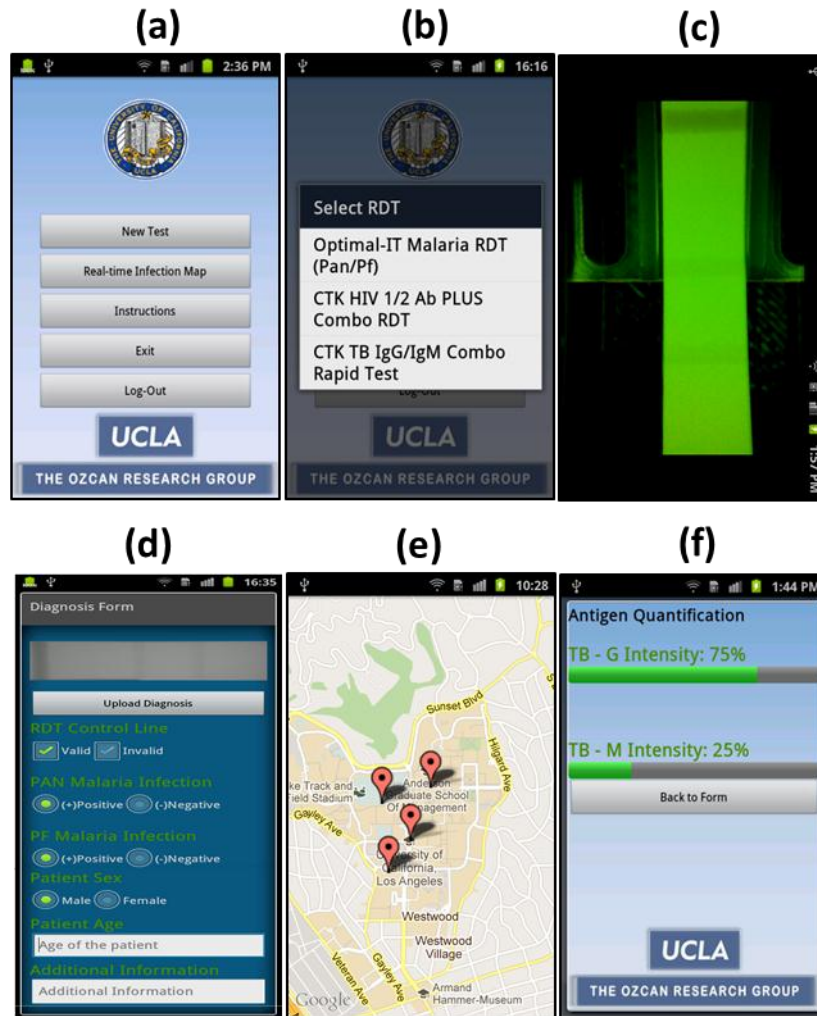


Figure A.2 RDT reader application running on the cell-phone device. (a) Authorized users can access to the main menu of the application only after successful log-in. (b) A pull-down menu is displayed for the previously-configured RDTs if user selects to image a new RDT. (c) Once the illumination scheme is chosen, users touch the cell-phone screen to digitally acquire image of the RDT that is then automatically processed and evaluated by the application. (d) Cell-phone application displays the RDT evaluation form including the validity and diagnostics results generated within <math><0.2</math> seconds. User can manually enter additional data to the evaluation form which is then uploaded to the central database/server (e), presented on a Google Maps based interface in real-time. (f) Same cell-phone application can perform semi-quantitative test color intensity measurement that is correlated to the disease antigen levels on the target analyte. Such quantitative analysis of a particular test kit requires a one-time initial

calibration by imaging a blank un-used test (for minimum color intensity reference) and a saturated test (for maximum color intensity reference) functionalized using positive control antigens.

Note also that the RDT cartridges to be digitally read are inserted into the base of the cellphone attachment using custom-designed trays (i.e., mechanical adapters specific to each RDT type – see e.g., Fig. A.1). This enables different types of RDTs to be evaluated on the same smart reader without any modification to the base of the main platform. Moreover, the custom-designed RDT application running on the cellphone can automatically identify the type of the RDT that is inserted, among a set of pre-programmed RDTs (see Fig. A.5) and permits software updates to digitally recognize additional RDT types when they are needed or become available.

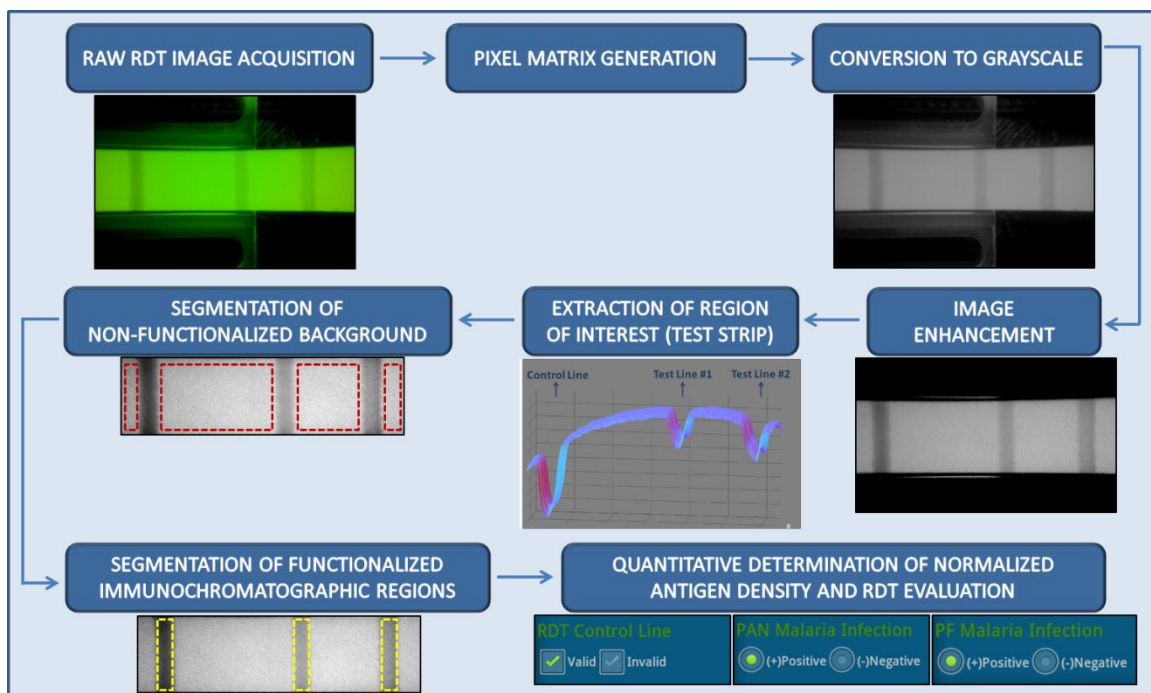


Figure A.3 Block diagram of the automated image processing algorithm that is run by the cellphone based smart RDT reader application. In this case a reflection image of the RDT is shown and processed.

Over the last few years there has also been a considerable effort focused toward the development of digital test readers which are capable of objective and quantitative analysis of

RDTs, e.g., lateral flow strips, dipsticks, cassette tests, or pads.¹⁷²⁻¹⁸² As a result, several commercial product lines have already been introduced, including LFDR101 Reader (Forsite Diagnostics Ltd, UK), ESEQuant Lateral Flow System (QIAGEN, CA, USA), RDS-1000 (Detekt Biomedical L.L.C., TX, USA), and DOA Test Reader (GenPrime, WA, USA). However, these existing digital test readers are still relatively bulky and costly; and more importantly they work with only a limited number of RDTs from a given manufacturer, which limits their wide-scale deployment and use, especially in resource scarce settings.



Figure A.4 Web interface of the Real Time RDT Map generated by the central server is shown. This global database stores and organizes test results uploaded by users. The server displays the test data on an internet browser using Google Maps and can filter the data displayed based on several attributes, including: disease type, test location and

time/date, RDT type/manufacture, patient age, etc. It can be reached from the main menu of the cellphone application or from a remote location using a personal computer or other mobile devices running a web browser.

On the other hand, this integrated RDT reader platform is a compact (~65 grams) and cost-effective alternative, capable of handling various types of RDTs from different manufacturers/vendors. For this end, using the camera module of the cellphone as well as its micro-processors creates a very efficient and cost-effective solution for any type of RDT (with various sizes and shapes) since imaging and signal processing provide the flexibility to digitize and automatically read different RDT types on the same cellphone platform. Moreover, it allows users to be part of a global network and browse through a real-time database of RDT results even in remote locations. Therefore, this RDT reader platform running on a cellphone does not only provide a complementary effort toward the development of inexpensive and mobile digital test readers, but also serves as a smart communication tool to connect health-care professionals and policy makers through a global network.

I tested this cellphone enabled RDT reader platform using malaria, tuberculosis as well as HIV tests by installing it on both Android based smart-phones as well as an iPhone (see Fig. A.1).¹⁷¹ I should emphasize that in this design, rather than capturing simple images of the RDTs using the cellphone camera under e.g., sunlight or room light, I created a specific add-on which had its own illumination and mechanical interface. This is quite important to increase the measurement repeatability and avoid reading errors due to illumination and field-of-view variations or tilts, all of which are now almost entirely eliminated in the cost-effective design shown in Fig. A.1.

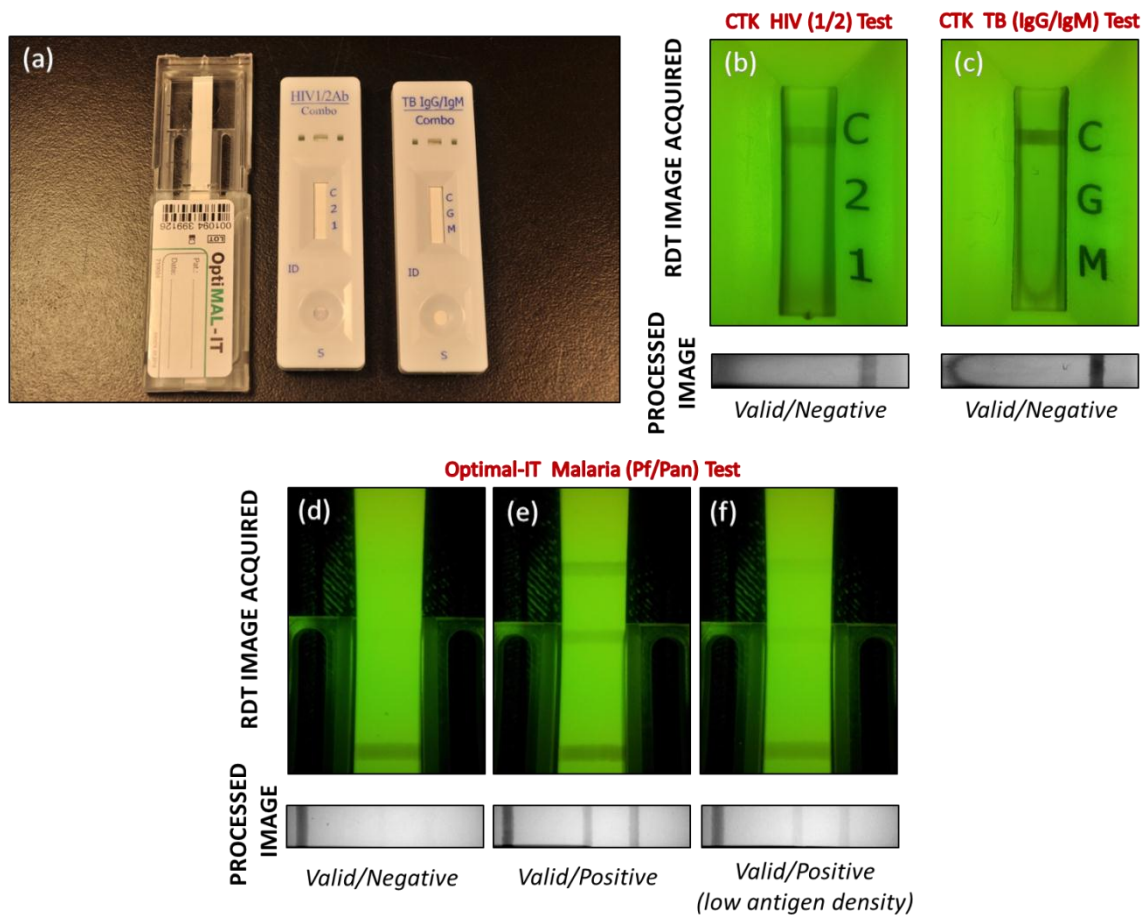


Figure A.5 (a) Rapid-diagnostic-tests (RTDs) used in this study (*Left*: Optimal-IT *P. falciparum*-specific and Pan-specific Malaria Test, *Middle*: CTK HIV 1/2 Ab PLUS Combo Test *Right*: CTK TB IgG/IgM Combo Test) are shown. HIV 1/2 Combo RDT (b) has a control reagent line indicating the validity of the test, and two pre-deposited antigen (HIV-1 and HIV-2) coated lines indicating the infections. (c) TB IgG/IgM Combo RDT is also a lateral-flow based immunoassay for the simultaneous detection and differentiation of IgM anti-*Mycobacterium Tuberculosis* (M.TB) and IgG anti-M.TB in human serum or whole blood. Digitally processed images of RDTs which are activated by fresh whole blood samples and their automated decisions are shown below the raw RDT images (b and c) acquired by the RDT reader application (in reflection mode). Optimal-IT Malaria Test (d, e, and f) detects *Plasmodium* antigens (pLDH) using monoclonal antibodies. I imaged (in reflection) a malaria test that was activated using human blood (d) and analyzed by cellphone RDT application. Moreover, I tested Malaria RDTs using positive control wells which are previously coated by recombinant antigens of *P. falciparum*.

Design of Smart RDT Reader Attachment

I implemented the RDT reader platform on various cell-phone units including Samsung Galaxy S II as a primary device, an iPhone 4S as well as a lower-end Android phone (Samsung Galaxy Fit GT-S5670) as shown in Figs. A.1 and A.6(a) and A.6(b), respectively.¹⁷¹ It should be noted that this platform is independent of the cell-phone operating system and hardware such that the same RDT attachment can work on different cell-phone devices with minor modifications on its base clip-on design. Custom-built using a recyclable and eco-friendly thermoplastic ABSplus™ modeling material on a 3-D printer, the mechanical body, weighing ~65 grams, encloses the optical components and eliminates the effect of environmental conditions (e.g., room light or sunlight) on image acquisition performance. Moreover, RDT trays were customized for each RDT type to accommodate different formats with varying dimensions (e.g., dipsticks, cassettes, strips, or cards) such that they can be evaluated using the same universal cellphone reader attachment without any modification on its imaging architecture.

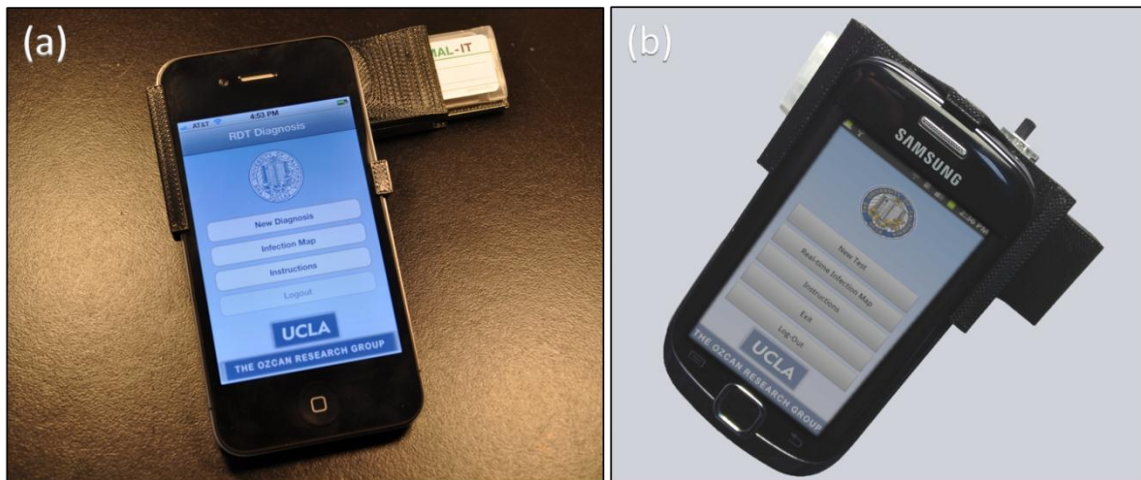


Figure A.6 In addition to the prototypes designed for Samsung Galaxy S II (see Fig. A.1 and A.7), I also implemented the same RDT reader attachment on (a) an iPhone 4S and (b) a lower-end Android phone (Samsung Galaxy Fit GT-S5670).

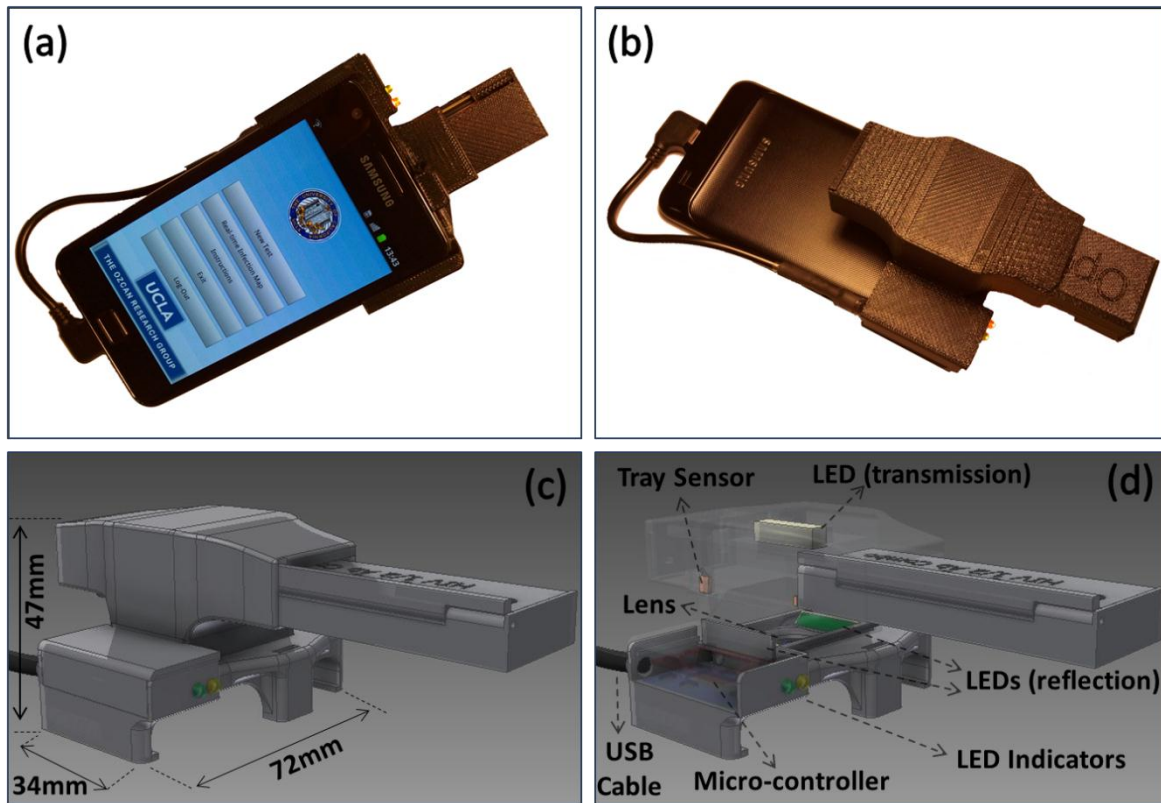


Figure A.7 A smart RDT reader prototype (attached to Samsung Galaxy S II) which is entirely powered by the cell-phone battery through a USB connection. Controlled through a cost-effective micro-controller, two LED indicators are also used in this design to automatically detect (i) if the attachment is successfully powered through USB; and (ii) if the RDT is properly loaded into the reader and is ready to be imaged.

In order to ensure uniform illumination of RDTs and high-quality imaging performance, multiple diffused LED arrays with a peak wavelength of 565 nm are located within the reader attachment. This operation wavelength was determined based on spectral measurements on RDTs (Optimal-IT *P. falciparum*-specific and Pan-specific Malaria Test, CTK HIV 1/2 Ab PLUS Combo Test, CTK TB IgG/IgM Combo Test)¹⁸³⁻¹⁸⁵ that have target test regions formed by immobilized colloidal gold-labeled antibody – antigen complexes (see Fig. A.8). Two of these diffused LED arrays are located underneath the RDT plane to uniformly illuminate the test of interest for reflection mode image acquisition that is convenient for most test formats (e.g.,

cassette-type RDTs). For the transmission mode imaging that is especially useful while working with strip tests, another LED array is positioned on the top of RDT plane, allowing high-contrast image acquisition. Users can switch between these two different illumination schemes using the physical switch located on the side of the attachment or digitally through the cell-phone audio jack (if it is available).

The RDT reader hardware attachment also utilizes an inexpensive plano-convex lens in front of the existing lens of the cell-phone camera unit that provides an overall optical demagnification factor of ~ 4 between the RDT plane on the attachment and CMOS image sensor plane on the cell-phone. Depending on the optical specifications of the different cell-phone camera modules, this demagnification factor can be tuned simply by changing the external plano-convex lens in the RDT reader attachment and does not affect the post-processing of the raw RDT images.

In addition to the AAA battery powered RDT reader shown in Fig. A.1, I also designed a hardware attachment that uses the cell-phone battery to power up the transmission and reflection mode illumination LED arrays (see Fig. A.7). Using a simple and inexpensive micro-controller, USB port of cell-phone device is utilized for power transfer and data communication between the reader attachment and the cell-phone device. Moreover, this particular design has two indicator LEDs that are also powered by the cell-phone battery, alerting the user if the illumination LEDs are successfully powered and RDT is properly inserted into the attachment for its digital reading and evaluation.

RDT Reader Cell-phone Application and Spatio-temporal Mapping of Epidemics

In this RDT reader platform, Android and iPhone applications¹⁷¹ were developed to digitally capture and rapidly process the raw RDT images to generate a digital test evaluation

report within <0.2 sec/test, consisting of test validation (Valid/Invalid), assessment of the diagnostic results (Positive/Negative) as well as other related patient information that can be manually entered to the form (see Fig. A.2). Once the cell-phone application acquires raw RDT image (e.g., transmission or reflection), it runs a set of custom-designed image processing steps (see Fig. A.3) to extract the necessary spatial features and analyze the color changes on the test that indicates the presence of the infection on immuno-chromatographic tests. In order to relieve the computational load on the cell-phone processor and memory, raw RDT image is first converted to grayscale and the regions of interests (e.g., test validation/control and diagnostics/infection-indicating lines) are digitally extracted based on the calibration results which is needed to be performed only once for each test type. Furthermore, cell-phone application also runs a central moving averaging function, decreasing the effect of spatial noise and manufacturing related non-uniformities on digital test evaluation prior to final decision process.

For the final evaluation of the digitally enhanced RDT image, cell-phone application automatically measures the grayscale pixel intensity values on regions of interest and determines the result of the test (valid/invalid and positive/negative) based on previously calibrated intensity levels. Once the diagnostics result is ready, an evaluation report is displayed on the cell-phone, allowing the user to manually add other necessary information such as patient ID, sex or other personal notes (see A.2). Using the available wireless communication links (e.g., Wi-Fi, GSM, etc.), this RDT evaluation report is transferred to the central database/server without putting any extra burden to the network as it has a data package size of < 0.05 Mbytes/test. In case the wireless resources are not available at the time of the testing, cell-phone application stores the

test results in its internal memory to be shared later when the wireless connectivity becomes available again.

RDT evaluation results uploaded by users are displayed on an encrypted web interface and spatio-temporal map. Reached from the main menu of the cell-phone application or internet browsers on remote computers by authorized users, spatio-temporal statistics of RDTs can be filtered based on several attributes (e.g., disease type, RDT type, testing location, patient age/sex, etc.) and allows users to access most up-to-date epidemiological information as shown in Fig. A.4.

Results and Discussions

To validate the performance of this smart RDT reader, I imaged several lateral flow based immuno-chromatographic RDTs including Optimal-IT P. falciparum-specific and Pan-specific Malaria Tests (Bio-Rad Laboratories, Inc., CA, USA), HIV 1/2 Ab PLUS Combo Rapid Tests as well as TB IgG/IgM Combo Rapid Tests (CTK Biotech Inc., CA, USA).¹⁸³⁻¹⁸⁵ I used healthy whole blood specimen and OptiMAL positive control wells (Bio-Rad Laboratories, Inc., CA, USA) containing recombinant antigens (LDH) of P. falciparum to mimic positive cases (see Figs. A.5 and A.8).

In order to demonstrate the repeatability of measurements using the smart RDT reader, imaging experiments were repeated more than 10 times per test type for Malaria, HIV and TB RDTs that were activated by healthy blood samples. Verified by visual examination following manufacturer's instructions, all the tests were correctly evaluated as "Valid/Negative" for each case (see e.g., Fig. A.5(c)).

I also conducted digital evaluation measurements on Malaria RDTs that were activated using OptiMAL positive control wells containing recombinant Pan-malaria antigens (see e.g., Fig. A.5(e)). Previously deposited on the control wells, antigens were released by mixing with sample diluents to mimic positive Pan-malaria (*P. Falciparum*, *P. Vivax*, *P. Ovale* and *P. malariae*) cases. In order to validate the quantitative imaging performance of the cellphone based RDT reader, I activated malaria RDTs at different positive control antigen levels as shown in Fig. A.8.

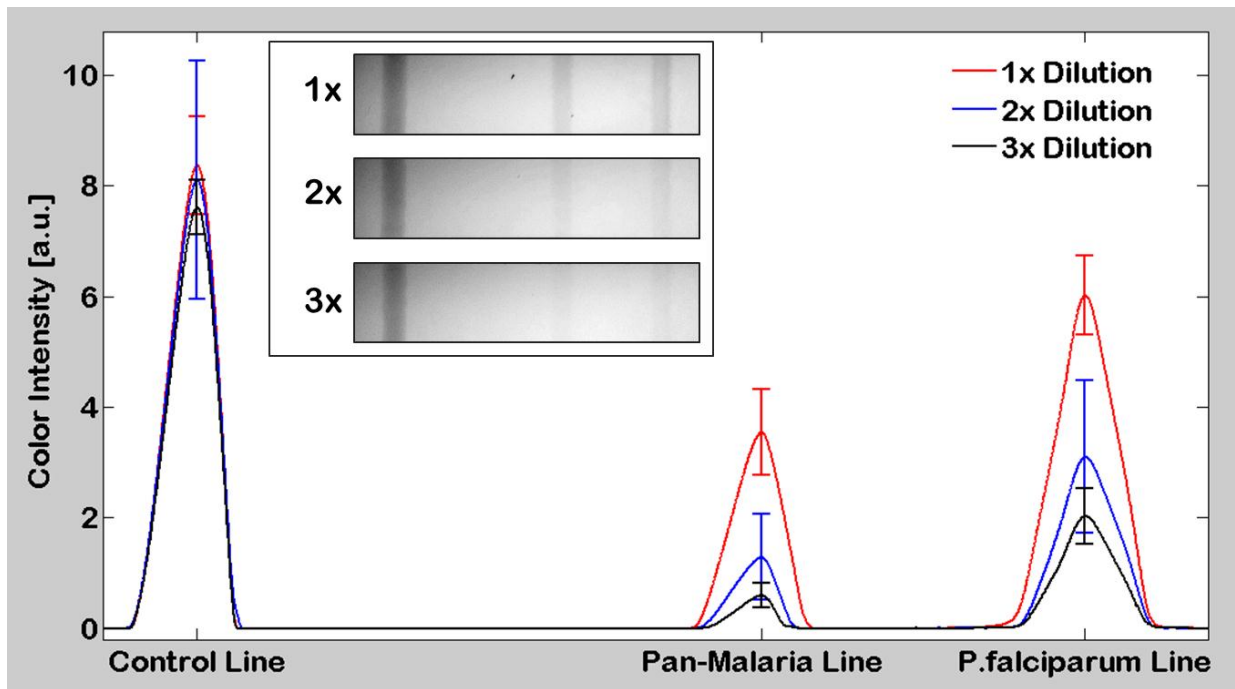


Figure A.8 Cross-sectional analysis of automatically processed Malaria RDT images captured in reflection mode. The RDT reader shown in Fig. 1(a) was used to evaluate Malaria RDTs activated with 3 different batches of *Positive Control Well Antigen* (PCWA) at dilution levels of PCWA/20 μ l (1x), PCWA/40 μ l (2x), PCWA/60 μ l (3x). The above figure illustrates the mean of 10 pre-processed RDT image cross-sections (for each dilution level) and the standard deviation of maximum peak values of each test line. Mean and standard deviation values of the Control, Pan-Malaria, and P. Falciparum lines of the 1x dilution level are 8.37, 3.54, 6.02; 0.89, 0.77, and 0.72, respectively. Mean and standard deviation values of the Control, Pan-Malaria, and P. Falciparum lines of the 2x dilution level are 8.11, 1.29, 3.10; 2.10, 0.77, and 1.38, respectively. Mean and standard deviation values of the Control, Pan-Malaria,

and P. Falciparum lines of the 3x dilution level are 7.62, 0.60, 2.03; 0.50, 0.22, and 0.51, respectively. Exemplary cellphone images of RDTs for each dilution level are also shown in the inset.

Starting with the “recommended” dilution level by the manufacturer, i.e., Positive Control Well Antigen (PCWA)/20 μ l, I further diluted it by 2, 3, and 4 times to create lower antigen concentration levels of PCWA/40 μ l (2x dilution), PCWA/60 μ l (3x dilution), and PCWA/80 μ l (4x dilution), respectively. For each concentration level, RDT imaging measurements were repeated 10 times and correctly analyzed as “Valid/Positive” by the cellphone application for all tests activated with PCWA/20 μ l (recommended 1x dilution), PCWA/40 μ l (2x dilution) as well as PCWA/60 μ l (3x dilution). The accuracy dropped down to ~60% for PCWA/80 μ l (4x dilution) due to the corresponding weak color intensity response on the RDTs (see Fig. A.8).

As shown in Fig. A.8, I observed higher average color intensity on P. Falciparum lines that were pre-deposited by only P. Falciparum specific antibodies, whereas the response of the Pan-malaria lines to the positive control wells are relatively weaker. Considering the fact that positive control wells only contain recombinant antigens (LDH) of P. falciparum, there was less number of antibody-antigen complexes formed in Pan-malaria test lines compared to the complexes formed on P. Falciparum specific lines and therefore lower mean color intensity was observed. These results exhibit the quantitative imaging performance and sensitivity of the RDT reader to differentiate even minor color intensity variations that may not be differentiated during visual validation of RDTs by humans. Note also that control lines indicate the validity of the RDTs to avoid manufacturing related problems on diagnostics results and their color response has no correlation with the content and density the target analyte or antigens.

In summary, this smart digital platform, which can automatically recognize, read and digitally store various kinds of RDTs, could be quite useful to reduce manual test reading errors and confusions arising due to simultaneous use of various RDT types, each of which might have different standards for control and positive/negative lines. Digitizing and quantifying the test results are also important since the color changes in RDTs do not last more than a few hours in field conditions, which makes physical storage of these tests not feasible, unless it is in digital format as implemented in our platform. Finally, offering real-time spatio-temporal statistics for the prevalence of various infectious diseases, this integrated RDT reader running on cellphones could assist health-care professionals and policy makers to rapidly track emerging epidemics worldwide and help epidemic preparedness.

References

1. Betzig, E. & Chichester, R. J. Single Molecules Observed by Near-Field Scanning Optical Microscopy. *Science* **262**, 1422–1425 (1993).
2. Lange, F. D. *et al.* Cell Biology Beyond the Diffraction Limit: Near-Field Scanning Optical Microscopy. *J Cell Sci* **114**, 4153–4160 (2001).
3. Kalkbrenner, T., Ramstein, M., Mlynek, J. & Sandoghdar, V. A single gold particle as a probe for apertureless scanning near-field optical microscopy. *Journal of Microscopy* **202**, 72–76 (2001).
4. Ozcan, A. *et al.* Differential Near-Field Scanning Optical Microscopy. *Nano Lett.* **6**, 2609–2616 (2006).
5. Huang, F. M. & Zheludev, N. I. Super-Resolution without Evanescent Waves. *Nano Lett.* **9**, 1249–1254 (2009).
6. Huang, B., Babcock, H. & Zhuang, X. Breaking the Diffraction Barrier: Super-Resolution Imaging of Cells. *Cell* **143**, 1047–1058 (2010).
7. Bates, M., Huang, B., Dempsey, G. T. & Zhuang, X. Multicolor Super-Resolution Imaging with Photo-Switchable Fluorescent Probes. *Science* **317**, 1749–1753 (2007).
8. Kner, P., Chhun, B. B., Griffis, E. R., Winoto, L. & Gustafsson, M. G. L. Super-resolution video microscopy of live cells by structured illumination. *Nature Methods* **6**, 339–342 (2009).
9. Fitzgibbon, J., Bell, K., King, E. & Oparka, K. Super-Resolution Imaging of Plasmodesmata Using Three-Dimensional Structured Illumination Microscopy. *Plant Physiol.* **153**, 1453–1463 (2010).

10. Huang, B., Wang, W., Bates, M. & Zhuang, X. Three-Dimensional Super-Resolution Imaging by Stochastic Optical Reconstruction Microscopy. *Science* **319**, 810–813 (2008).
11. Binnig, G., Quate, C. F. & Gerber, C. Atomic Force Microscope. *Phys. Rev. Lett.* **56**, 930–933 (1986).
12. Ebenstein, Y., Nahum, E. & Banin, U. Tapping Mode Atomic Force Microscopy for Nanoparticle Sizing: Tip–Sample Interaction Effects. *Nano Lett.* **2**, 945–950 (2002).
13. Chithrani, B. D., Ghazani, A. A. & Chan, W. C. W. Determining the Size and Shape Dependence of Gold Nanoparticle Uptake into Mammalian Cells. *Nano Lett.* **6**, 662–668 (2006).
14. Feinstone, S. M., Kapikian, A. Z. & Purcell, R. H. Hepatitis A: Detection by Immune Electron Microscopy of a Viruslike Antigen Associated with Acute Illness. *Science* **182**, 1026–1028 (1973).
15. Hockley, D. J., Wood, R. D., Jacobs, J. P. & Garrett, A. J. Electron microscopy of human immunodeficiency virus. *J. Gen. Virol.* **69**, (Pt 10), 2455–2469 (1988).
16. Pease, L. F. *et al.* Quantitative characterization of virus-like particles by asymmetrical flow field flow fractionation, electrospray differential mobility analysis, and transmission electron microscopy. *Biotechnol. Bioeng.* **102**, 845–855 (2009).
17. Shevchuk, A. I. *et al.* Imaging Single Virus Particles on the Surface of Cell Membranes by High-Resolution Scanning Surface Confocal Microscopy. *Biophys J* **94**, 4089–4094 (2008).
18. Ignatovich, F. V., Topham, D. & Novotny, L. Optical Detection of Single Nanoparticles and Viruses. *IEEE Journal of Selected Topics in Quantum Electronics* **12**, 1292 –1300 (2006).

19. Daaboul, G. G. *et al.* High-Throughput Detection and Sizing of Individual Low-Index Nanoparticles and Viruses for Pathogen Identification. *Nano Lett.* **10**, 4727–4731 (2010).
20. Hong, X. *et al.* Background-Free Detection of Single 5 nm Nanoparticles through Interferometric Cross-Polarization Microscopy. *Nano Lett.* **11**, 541–547 (2011).
21. Stern, A. & Javidi, B. Improved-resolution digital holography using the generalized sampling theorem for locally band-limited fields. *J. Opt. Soc. Am. A* **23**, 1227–1235 (2006).
22. Rivenson, Y., Stern, A. & Javidi, B. Single exposure super-resolution compressive imaging by double phase encoding. *Opt. Express* **18**, 15094–15103 (2010).
23. Hell, S. W. Toward fluorescence nanoscopy. *Nat Biotech* **21**, 1347–1355 (2003).
24. Gustafsson, M. G. L. Nonlinear structured-illumination microscopy: Wide-field fluorescence imaging with theoretically unlimited resolution. *Proceedings of the National Academy of Sciences of the United States of America* **102**, 13081–13086 (2005).
25. Betzig, E. *et al.* Imaging Intracellular Fluorescent Proteins at Nanometer Resolution. *Science* **313**, 1642–1645 (2006).
26. Rust, M. J., Bates, M. & Zhuang, X. Sub-diffraction-limit imaging by stochastic optical reconstruction microscopy (STORM). *Nat Meth* **3**, 793–796 (2006).
27. Hess, S. T., Girirajan, T. P. K. & Mason, M. D. Ultra-High Resolution Imaging by Fluorescence Photoactivation Localization Microscopy. *Biophysical Journal* **91**, 4258–4272 (2006).
28. Ma, Z., Gerton, J. M., Wade, L. A. & Quake, S. R. Fluorescence near-field microscopy of DNA at sub-10 nm resolution. *Phys. Rev. Lett* **97**, 260801 (2006).

29. Chung, E., Kim, D., Cui, Y., Kim, Y.-H. & So, P. T. C. Two-Dimensional Standing Wave Total Internal Reflection Fluorescence Microscopy: Superresolution Imaging of Single Molecular and Biological Specimens. *Biophysical Journal* **93**, 1747–1757 (2007).
30. Pavani, S. R. P. *et al.* Three-dimensional, single-molecule fluorescence imaging beyond the diffraction limit by using a double-helix point spread function. *Proceedings of the National Academy of Sciences* **106**, 2995–2999 (2009).
31. Schaller, Robert R. Moore's law: past, present and future. *IEEE Spectrum* **34**, 52-59 (1997).
32. Tseng, D. *et al.* Lensfree microscopy on a cellphone. *Lab Chip* **10**, 1787-1792 (2010).
33. International Telecommunication Union, Market information and statistics, <http://www.itu.int/ITU-D/ict/statistics/maps.html> (2007).
34. Banjanovic, A. Special Report: Towards universal global mobile phone coverage, *Euromonitor International* (2009).
35. Nokia, Nokia 808 Pureview, <http://europe.nokia.com/findproducts/devices/nokia-808-pureview> (2012).
36. Mavandadi, S. *et al.* Crowd-sourced BioGames: managing the big data problem for next-generation lab-on-a-chip platforms. *Lab Chip* **12**, 4102-4106 (2012).
37. Mudanyali, O. *et al.* Compact, light-weight and cost-effective microscope based on lensless incoherent holography for telemedicine applications. *Lab Chip* **10**, 1417-1428 (2010).
38. Psaltis, D., Quake, S. R. & Yang, C. Developing optofluidic technology through the fusion of microfluidics and optics. *Nature* **442**, 381–386 (2006).

39. Haddad, W. S. *et al.* Fourier-transform holographic microscope. *Appl. Opt.* **31**, 4973–4978 (1992).
40. Xu, W., Jericho, M. H., Meinertzhagen, I. A. & Kreuzer, H. J. Digital in-line holography for biological applications. *Proceedings of the National Academy of Sciences of the United States of America* **98**, 11301–11305 (2001).
41. Pedrini, G. & Tiziani, H. J. Short-Coherence Digital Microscopy by Use of a Lensless Holographic Imaging System. *Appl. Opt.* **41**, 4489–4496 (2002).
42. Repetto, L., Piano, E. & Pontiggia, C. Lensless digital holographic microscope with light-emitting diode illumination. *Opt. Lett.* **29**, 1132–1134 (2004).
43. Garcia-Sucerquia, J., Xu, W., Jericho, M. H. & Kreuzer, H. J. Immersion digital in-line holographic microscopy. *Opt. Lett.* **31**, 1211–1213 (2006).
44. Heng, X. *et al.* Optofluidic microscopy—a method for implementing a high resolution optical microscope on a chip. *Lab Chip* **6**, 1274–1276 (2006).
45. Cui, X. *et al.* Lensless high-resolution on-chip optofluidic microscopes for *Caenorhabditis elegans* and cell imaging. *Proceedings of the National Academy of Sciences of the United States of America* **105**, 10670–10675 (2008).
46. Mudanyali, O., Bishara, W. & Ozcan, A. Lensfree super-resolution holographic microscopy using wetting films on a chip. *Opt. Express* **19**, 17378–17389 (2011).
47. Bishara, W. *et al.* Holographic pixel super-resolution in portable lensless on-chip microscopy using a fiber-optic array. *Lab Chip* **11**, 1276–1279 (2011).
48. Bishara, W., Su, T.-W., Coskun, A. F. & Ozcan, A. Lensfree on-chip microscopy over a wide field-of-view using pixel super-resolution. *Opt. Express* **18**, 11181–11191 (2010).

49. Isikman, S. O. *et al.* Lens-Free Optical Tomographic Microscope with a Large Imaging Volume on a Chip. *Proceedings of the National Academy of Sciences of the United States of America* **108**, 7296-7301 (2011).
50. Isikman, S. O. *et al.* Lensfree computational microscopy tools for cell and tissue imaging at the point-of-care and in low-resource settings. *Anal Cell Pathol* **35**, 229–247 (2012).
51. Greenbaum, A., Sikora, U. & Ozcan, A. Field-portable wide-field microscopy of dense samples using multi-height pixel super-resolution based lensfree imaging. *Lab Chip* **12**, 1242–1245 (2012).
52. Mudanyali, O. *et al.* Detection of waterborne parasites using field-portable and cost-effective lensfree microscopy. *Lab Chip* **10**, 2419-2423 (2010).
53. Brady, D. J. *Optical imaging and spectroscopy.* (John Wiley & Sons, Hoboken, NJ, USA: 2009).
54. Lohmann, A. W. Wavefront Reconstruction for Incoherent Objects. *J. Opt. Soc. Am.* **55**, 1555_1–1556 (1965).
55. Mertz, L. *Transformation in Optics.* (John Wiley & Sons, Hoboken, NJ, USA: 1965).
56. Dubois, F., Joannes, L. & Legros, J.-C. Improved Three-Dimensional Imaging with a Digital Holography Microscope With a Source of Partial Spatial Coherence. *Appl. Opt.* **38**, 7085–7094 (1999).
57. Dubois, F., Novella Requena, M.-L., Minetti, C., Monnom, O. & Istasse, E. Partial spatial coherence effects in digital holographic microscopy with a laser source. *Appl. Opt.* **43**, 1131–1139 (2004).
58. Rosen, J. & Brooker, G. Non-scanning motionless fluorescence three-dimensional holographic microscopy. *Nat Photon* **2**, 190–195 (2008).

59. Situ, G. & Sheridan, J. T. Holography: an interpretation from the phase-space point of view. *Optics Letters* **32**, 3492-3494 (2007).
60. Sherman, G. C. Application of the convolution theorem to Rayleigh's integral formulas. *JOSA* **57**, 546-547 (1967).
61. Koren, G., Polack, F., & Joyeux, D. Iterative algorithms for twin-image elimination in in-line holography using finite-support constraints. *JOSA A* **10**, 423-433 (1993).
62. Fienup, J. R. Reconstruction of an object from the modulus of its Fourier transform. *Optics Letters* **3**, 27-29 (1978).
63. Monroy, F. *et al.* Quantitative assessment of lateral resolution improvement in digital holography. *Optics Communications* **281**, 3454-3460 (2008).
64. England, J. M. *et al.* Guidelines for the evaluation of blood cell analysers including those used for differential leucocyte and reticulocyte counting and cell marker applications. *Clinical & Laboratory Haematology* **16**, 157-174 (1994).
65. Breslauer, D. N. *et al.* Mobile phone based clinical microscopy for global health applications. *PLoS One* **4**, e6320. (2009).
66. Zhu, H. *et al.* Cost-effective and compact wide-field fluorescent imaging on a cell-phone. *Lab Chip* **11**, 315-322 (2010).
67. Fife, K., Gamal, A. E., and Wong H. S. P. A multi-aperture image sensor with 0.7 μm pixels in 0.11 μm CMOS technology. *IEEE Journal of Solid-State Circuits* **43**, 2990-3005 (2008).
68. Dziuban, E. J. *et al.* Surveillance for waterborne disease and outbreaks associated with recreational water, United States, 2003-2004 (In: Surveillance Summaries). *MMWR* **55**, 1-30 (2008).

69. Shannon, M. A. *et al.* Science and technology for water purification in the coming decades. *Nature* **452**, 301-310 (2008).
70. Marris, E. Film: Water policy in the can. *Nature* **452**, 288-288 (2008).
71. Fenwick, A. Waterborne infectious diseases-could they be consigned to history?. *Science* **313**, 1077-1081 (2006).
72. Bouzid, M., Steverding D., & Tyler K. M. Detection and surveillance of waterborne protozoan parasites. *Current Opinion In Biotechnology* **19**, 302-306 (2008).
73. Huang, D. B., & White, A. C. An updated review on Cryptosporidium and Giardia. *Gastroenterology Clinics of North America* **35**, 291-314 (2006).
74. Ferrari, B. C., Stoner, K., & Bergquist, P. L. Applying fluorescence based technology to the recovery and isolation of Cryptosporidium and Giardia from industrial wastewater streams. *Water Research* **40**, 541-548 (2006).
75. Kulkarni, Y., *et al.* A simple and rapid technique for concentration of Entamoeba histolytica cysts from contaminated water. *International Journal of Environmental Studies* **44**, 307-311 (1993).
76. De Roubin, M. R. *et al.* Application of laser scanning cytometry followed by epifluorescent and differential interference contrast microscopy for the detection and enumeration of Cryptosporidium and Giardia in raw and potable waters. *Journal of Applied Microbiology* **93**, 599-607 (2002).
77. Szewzyk, U. *et al.* Microbiological safety of drinking water. *Annual Reviews in Microbiology* **54**, 81-127 (2000).
78. Brettar, I. & Höfle, M. G. Molecular assessment of bacterial pathogens - a contribution to drinking water safety. *Current Opinion in Biotechnology* **19**, 274-280 (2008).

79. Shanks, O. C. *et al.* Quantitative PCR for detection and enumeration of genetic markers of bovine fecal pollution. *Applied and Environmental Microbiology* **74**, 745-752 (2008).
80. Lothigius, Å. *et al.* Enterotoxigenic *Escherichia coli* is detectable in water samples from an endemic area by real-time PCR. *Journal of Applied Microbiology* **104**, 1128-1136 (2008).
81. Ahn, S. & Walt, D. R. Detection of *Salmonella* spp. using microsphere-based, fiber-optic DNA microarrays. *Analytical Chemistry* **77**, 5041-5047 (2005).
82. Liao, W. C. & Ho, J. A. Attomole DNA electrochemical sensor for the detection of *Escherichia coli* O157. *Analytical Chemistry* **81**, 2470-2476 (2009).
83. Wang, C. & Irudayaraj, J. Gold nanorod probes for the detection of multiple pathogens. *Small* **4**, 2204-2208 (2008).
84. Maalouf, R. *et al.* Label-free detection of bacteria by electrochemical impedance spectroscopy: comparison to surface plasmon resonance. *Analytical Chemistry* **79**, 4879-4886 (2007).
85. Bushon, R. N. *et al.* Rapid detection of *Escherichia coli* and enterococci in recreational water using an immunomagnetic separation/adenosine triphosphate technique. *Journal of Applied Microbiology* **106**, 432-441 (2009).
86. Hammes, F. *et al.* Flow-cytometric total bacterial cell counts as a descriptive microbiological parameter for drinking water treatment processes. *Water Research* **42**, 269-277 (2008).
87. Yang, L. *et al.* Rapid, absolute, and simultaneous quantification of specific pathogenic strain and total bacterial cells using an ultrasensitive dual-color flow cytometer. *Analytical Chemistry* **82**, 1109-1116 (2009).

88. Rule, K. L. & Vikesland P. J. Surface-enhanced resonance Raman spectroscopy for the rapid detection of *Cryptosporidium parvum* and *Giardia lamblia*. *Environmental Science & Technology* **43**, 1147-1152 (2009).
89. Li, X. X. *et al.* Detection of pathogen based on the catalytic growth of gold nanocrystals." *Water Research* **43** 1425-1431 (2009).
90. Sakamoto, C., Yamaguchi, N., & Nasu, M. Rapid and simple quantification of bacterial cells by using a microfluidic device. *Applied and Environmental Microbiology* **71**, 1117-1121 (2005).
91. Sakamoto, C. *et al.* Rapid quantification of bacterial cells in potable water using a simplified microfluidic device. *Journal of Microbiological Methods* **68**, 643-647 (2007).
92. Lee, L. M., Cui, X., & Yang, C. The application of on-chip optofluidic microscopy for imaging *Giardia lamblia* trophozoites and cysts. *Biomedical Microdevices* **11**, 951-958 (2009).
93. Mudanyali, O. *et al.* Lensless on-chip imaging of cells provides a new tool for high-throughput cell-biology and medical diagnostics. *Journal of Visualized Experiments* **34**, (2009).
94. Holman, B. *et al.* Recovery Of *Giardia* Cysts From Water: Centrifugation vs Filtration. *Water Research* **17**, 1705-1707 (1983).
95. Kepner, R. L. & Pratt, J. R. Use of fluorochromes for direct enumeration of total bacteria in environmental samples: past and present. *Microbiological Reviews* **58**, 603-615 (1994).
96. Lee, C. M. *et al.* Covalently linked immunomagnetic separation/adenosine triphosphate technique (Cov-IMS/ATP) enables rapid, in-field detection and quantification of

- Escherichia coli and Enterococcus spp. in freshwater and marine environments. *Journal Of Applied Microbiology* **109**, 324-333 (2009).
97. Seo, S. *et al.* Lensfree holographic imaging for on-chip cytometry and diagnostics. *Lab Chip* **9**, 777-787 (2008).
98. Turgeon, M. L. Clinical hematology: theory and procedures. (Lippincott Williams & Wilkins, Philadelphia, PA, 2004).
99. Alimonti, J. B. *et al.* Mechanisms of CD4+ T lymphocyte cell death in human immunodeficiency virus infection and AIDS. *Journal of general Virology* **84**, 1649-1661 (2003).
100. Douek, D. C. *et al.* HIV preferentially infects HIV-specific CD4+ T cells. *Nature* **417**, 95-98 (2002).
101. Brenchley, J. M. *et al.* CD4+ T cell depletion during all stages of HIV disease occurs predominantly in the gastrointestinal tract. *The Journal of Experimental Medicine* **200**, 749-759 (2004).
102. Pantaleo, G. & Harari, A. Functional signatures in antiviral T-cell immunity for monitoring virus-associated diseases. *Nature Reviews Immunology* **6**, 417-423 (2006).
103. Pantaleo, G. & Koup, R. A. Correlates of immune protection in HIV-1 infection: what we know, what we don't know, what we should know. *Nature Medicine* **10**, 806-810 (2004).
104. Rosenberg, E. S. *et al.* Vigorous HIV-1-specific CD4+ T cell responses associated with control of viremia. *Science* **278**, 1447-1450 (1997).
105. Brando, B. *et al.* Cytofluorometric methods for assessing absolute numbers of cell subsets in blood. *Cytometry* **42**, 327-346 (2000).

106. Karlsson, A. C. *et al.* Comparison of the ELISPOT and cytokine flow cytometry assays for the enumeration of antigen-specific T cells. *Journal of Immunological Methods* **283**, 141-153 (2003).
107. Toner, M. & Irimia, D. Blood-on-a-chip. *Annu. Rev. Biomed. Eng.* **7**, 77-103 (2005).
108. Cheng, X. *et al.* A microfluidic device for practical label-free CD4+ T cell counting of HIV-infected subjects. *Lab Chip* **7**, 170-178 (2006).
109. Sethu, P. *et al.* Microfluidic isolation of leukocytes from whole blood for phenotype and gene expression analysis. *Analytical Chemistry* **78**, 5453-5461 (2006).
110. Cheng, X. *et al.* Enhancing the performance of a point-of-care CD4+ T-cell counting microchip through monocyte depletion for HIV/AIDS diagnostics. *Lab Chip* **9**, 1357-1364 (2009).
111. Rodriguez, W. R. *et al.* A microchip CD4 counting method for HIV monitoring in resource-poor settings. *Plos Medicine* **2**, e182 (2005).
112. Cheng, X. *et al.* Cell detection and counting through cell lysate impedance spectroscopy in microfluidic devices. *Lab Chip* **7**, 746-755 (2007).
113. Wang, Y. N. *et al.* On-chip counting the number and the percentage of CD4+ T lymphocytes. *Lab Chip* **8**, 309-315 (2007).
114. Stybayeva, G. *et al.* Lensfree holographic imaging of antibody microarrays for high-throughput detection of leukocyte numbers and function. *Analytical Chemistry* **82**, 3736-3744 (2010).
115. Belov, L. *et al.* Immunophenotyping of leukemias using a cluster of differentiation antibody microarray. *Cancer Research* **61**, 4483-4489 (2001).

116. Zhu, H. *et al.* A miniature cytometry platform for capture and characterization of T-lymphocytes from human blood. *Analytica Chimica Acta* **608**, 186-196 (2008).
117. Zhu, H. *et al.* A microdevice for multiplexed detection of T-cell-secreted cytokines. *Lab Chip* **8**, 2197-2205 (2008).
118. Zhu, H. *et al.* Detecting cytokine release from single human T-cells. *Analytical Chemistry* **81**, 8150-8156 (2009).
119. Jones, C. N. *et al.* Multifunctional protein microarrays for cultivation of cells and immunodetection of secreted cellular products. *Analytical Chemistry* **80**, 6351-6357 (2008).
120. Hubner, W. *et al.* Quantitative 3D Video Microscopy of HIV Transfer Across T Cell Virological Synapses. *Science* **323**, 1743-1747 (2009).
121. Bonnet, M. *et al.* Bleach Sedimentation: An Opportunity to Optimize Smear Microscopy for Tuberculosis Diagnosis in Settings of High Prevalence of HIV. *Clin Infect Dis* **46**, 1710-1716 (2008).
122. Nakada, T. *et al.* In Vivo Visualization of Senile-Plaque-Like Pathology in Alzheimer's Disease Patients by MR Microscopy on a 7T System. *Journal of Neuroimaging* **18**, 125-129 (2008).
123. Patel D. V. & McGhee C. N. J. In vivo confocal microscopy of corneal stromal nerves in patients with peripheral neuropathy. *Arch Neurol* **66**, 1179-1180 (2009).
124. Selvarajah, M. *et al.* Targeted urine microscopy in Anderson-Fabry Disease: a cheap, sensitive and specific diagnostic technique. *Nephrology Dialysis Transplantation* **26**, 3195-3202 (2011).

125. Kojima, T. *et al.* The application of in vivo laser scanning confocal microscopy as a tool of conjunctival in vivo cytology in the diagnosis of dry eye ocular surface disease. *Mol Vis* **16**, 2457-2464 (2010).
126. Sartori, A. *et al.* Correlative Light/Electron Microscopy: a Tool for Investigating Infectious Diseases. *MAM* **15**, 862 (2009).
127. Shea, Y. R. *et al.* High Sensitivity and Specificity of Acid-Fast Microscopy for Diagnosis of Pulmonary Tuberculosis in an African Population with a High Prevalence of Human Immunodeficiency Virus. *Journal of Clinical Microbiology* **47**, 1553-1555 (2009).
128. Wu, S.-R. *et al.* Single-particle cryoelectron microscopy analysis reveals the HIV-1 spike as a tripod structure. *Proceedings of the National Academy of Sciences* **107**, 18844-18849 (2010).
129. Marais, B. J. *et al.* Use of Light-Emitting Diode Fluorescence Microscopy to Detect Acid-Fast Bacilli in Sputum," *Clin Infect Dis* **47**, 203-207 (2008).
130. Essaka, D. C. *et al.* Monitoring the Uptake of Glycosphingolipids In Plasmodium falciparum -Infected Erythrocytes Using Both Fluorescence Microscopy and Capillary Electrophoresis with Laser-Induced Fluorescence Detection. *Anal. Chem.* **82**, 9955-9958 (2010).
131. Krause, M. *et al.* Localizing and Identifying Living Bacteria in an Abiotic Environment by a Combination of Raman and Fluorescence Microscopy. *Anal. Chem.* **80**, 8568-8575 (2008).
132. Hassan, S. E.-D. H. *et al.* Testing the sensitivity and specificity of the fluorescence microscope (Cyscope) for malaria diagnosis. *Malar. J* **9**, 88 (2010).

133. Bishara, W., Zhu, H., & Ozcan, A. Holographic opto-fluidic microscopy. *Opt. Express* **18**, 27499-27510 (2010).
134. Bonn, D. *et al.* Wetting and spreading. *Rev. Mod. Phys.* **81**, 739-805 (2009).
135. De Gennes, P. Wetting: statics and dynamics. *Rev. Mod. Phys.* **57**, 827-863 (1985).
136. Starov, V. M., Velarde, M. G., & Clayton, J. R. *Wetting and Spreading Dynamics* (CRC Press, 2007).
137. Stelmashenko, N. A. *et al.* Topographic contrast of partially wetting water droplets in environmental scanning electron microscopy. *Journal of Microscopy* **204**, 172-183 (2002).
138. Wei, Q. F., Mather, R. R., Fotheringham, A. F., & Yang, R. D. Dynamic Wetting of Fibers Observed in an Environmental Scanning Electron Microscope. *Textile Research Journal* **73**, 557-561 (2003).
139. Bormashenko, E. *et al.* Environmental Scanning Electron Microscopy Study of the Fine Structure of the Triple Line and Cassie–Wenzel Wetting Transition for Sessile Drops Deposited on Rough Polymer Substrates. *Langmuir* **23**, 4378-4382 (2007).
140. Allier, C. P., Hiernard, G., Poher, V., & Dinten, J. M. Bacteria detection with thin wetting film lensless imaging. *Biomed. Opt. Express* **1**, 762-770 (2010).
141. Allier, C. P., Poher, V., Coutard, J. G., Hiernard, G., & Dinten, J. M. Thin wetting film lensless imaging. (in Proceedings of the SPIE 2011), 790608-790608-8. (2011).
142. Hardie, R. C., Barnard, K. J., & Armstrong, E. E. Joint MAP registration and high-resolution image estimation using a sequence of undersampled images. *IEEE Trans. on Image Process.* **6**, 1621-1633 (1997).

143. Park, S. C., Park, M. K., & Kang, M. G. Super-resolution image reconstruction: a technical overview. *IEEE Signal Process. Mag.* **20**, 21-36 (2003).
144. Woods, N. A., Galatsanos, N. P., & Katsaggelos, A. K. Stochastic methods for joint registration, restoration, and interpolation of multiple undersampled images. *IEEE Trans. on Image Process.* **15**, 201-213 (2006).
145. Hardie, R. C. High-resolution image reconstruction from a sequence of rotated and translated frames and its application to an infrared imaging system. *Opt. Eng.* **37**, 247 (1998).
146. Greenbaum, A. *et al.* Imaging without lenses: achievements and remaining challenges of wide-field on-chip microscopy. *Nature Methods* **9**, 889-895 (2012).
147. Zalevsky, Z., Gur, E., Garcia, J., Micó, V. & Javidi, B. Superresolved and field-of-view extended digital holography with particle encoding. *Opt. Lett.* **37**, 2766–2768 (2012).
148. Borkowski, A., Zalevsky, Z. & Javidi, B. Geometrical superresolved imaging using nonperiodic spatial masking. *J. Opt. Soc. Am. A* **26**, 589–601 (2009).
149. Mendlovic, D. & Zalevsky, Z. *Optical Super Resolution*. (Erich Schmidt Verlag: 2003).
150. Young, T. An Essay on the Cohesion of Fluids. *Philosophical Transactions of the Royal Society of London* **95**, 65–87 (1805).
151. Gennes, P.-G. D., Brochard-Wyart, F. & Quéré, D. *Capillarity and Wetting Phenomena: Drops, Bubbles, Pearls, Waves*. (Springer: 2004).
152. Yeh, E. K., Newman, J. & Radke, C. J. Equilibrium configurations of liquid droplets on solid surfaces under the influence of thin-film forces: Part I. Thermodynamics. *Colloids and Surfaces A: Physicochemical and Engineering Aspects* **156**, 137–144 (1999).

153. Yeh, E. K., Newman, J. & Radke, C. J. Equilibrium configurations of liquid droplets on solid surfaces under the influence of thin-film forces: Part II. Shape calculations. *Colloids and Surfaces A: Physicochemical and Engineering Aspects* **156**, 525–546 (1999).
154. Israelachvili, J. N. *Intermolecular and Surface Forces*. (Academic Press: 2011).
155. Compostizo, A., Cancho, S. M., Rubio, R. G. & Crespo Colin, A. Experimental study of the equation of state and the surface tension of water-soluble polymers: poly(ethylene glycol)-b-poly(propylene glycol)-b-poly(ethylene glycol) + water at 298.15 K. *Physical Chemistry Chemical Physics* **3**, 1861–1866 (2001).
156. Nadkarni, G. D. & Garoff, S. An Investigation of Microscopic Aspects of Contact Angle Hysteresis: Pinning of the Contact Line on a Single Defect. *Europhysics Letters (EPL)* **20**, 523–528 (1992).
157. Marsh, J. A. & Cazabat, A. M. Dynamics of contact line depinning from a single defect. *Phys. Rev. Lett.* **71**, 2433–2436 (1993).
158. Born, P., Blum, S., Munoz, A. & Kraus, T. Role of the Meniscus Shape in Large-Area Convective Particle Assembly. *Langmuir* **27**, 8621–8633 (2011).
159. Bonn, D., Eggers, J., Indekeu, J., Meunier, J. & Rolley, E. Wetting and spreading. *Rev. Mod. Phys.* **81**, 739–805 (2009).
160. Beltrame, P., Knobloch, E., Hänggi, P. & Thiele, U. Rayleigh and depinning instabilities of forced liquid ridges on heterogeneous substrates. *Phys. Rev. E* **83**, 016305 (2011).
161. Kasarova, S. N., Sultanova, N. G., Ivanov, C. D. & Nikolov, I. D. Analysis of the dispersion of optical plastic materials. *Optical Materials* **29**, 1481–1490 (2007).

162. Mohsen-Nia, M., Modarress, H. & Rasa, H. Measurement and Modeling of Density, Kinematic Viscosity, and Refractive Index for Poly(ethylene Glycol) Aqueous Solution at Different Temperatures. *J. Chem. Eng. Data* **50**, 1662–1666 (2005).
163. Vasoo, S., Stevens, J. & Singh, K. Rapid antigen tests for diagnosis of pandemic (Swine) influenza A/H1N1. *Clinical Infectious Diseases* **49**, 1090-1093 (2009).
164. Mills, L.A. *et al.* Performance of a prototype malaria rapid diagnostic test versus thick film microscopy among HIV-positive subjects in rural Rakai, Uganda. *Transactions of the Royal Society of Tropical Medicine and Hygiene* **104**, 237-239 (2010).
165. Dhorda, M. *et al.* Performance of a Histidine-Rich Protein 2 Rapid Diagnostic Test, Paracheck Pf®, for Detection of Malaria Infections in Ugandan Pregnant Women. *The American Journal Of Tropical Medicine And Hygiene* **86**, 93-95 (2012).
166. Okeke, I. N. *et al.* Diagnostics as essential tools for containing antibacterial resistance. *Drug Resistance Updates* **14**, 95-106 (2011).
167. Murray, C. K., Gasser, R. A., Magill, A. J., & Miller, R. S. Update on rapid diagnostic testing for malaria. *Clinical Microbiology Reviews* **21**, 97-110 (2008).
168. Skarbinski, J. *et al.* Effect of malaria rapid diagnostic tests on the management of uncomplicated malaria with artemether-lumefantrine in Kenya: a cluster randomized trial. *The American Journal Of Tropical Medicine And Hygiene* **80**, 919-926 (2009).
169. Yager, P. *et al.* Microfluidic diagnostic technologies for global public health. *Nature* **442**, 412-418 (2006).
170. Sia, S. K., Linder, V., Parviz, B. A., Siegel, A., & Whitesides, G. M. An Integrated Approach to a Portable and Low-Cost Immunoassay for Resource-Poor Settings. *Angewandte Chemie International Edition* **43**, 498-502 (2004).

171. Mudanyali, O. *et al.* Integrated rapid-diagnostic-test reader platform on a cellphone. *Lab Chip* **12**, 2678-2686 (2012).
172. Hurling, R. *et al.* Using internet and mobile phone technology to deliver an automated physical activity program: randomized controlled trial. *J Med Internet Res* **9**, e7, (2007).
173. Corstjens, P. L. A. M., Li, S., Zuiderwijk, M., Kardos, K., Abrams, W. R., Niedbala, R. S., & Tanke, H. J. Infrared up-converting phosphors for bioassays. In *Nanobiotechnology, IEE Proceedings* **152**, 64-72 (2005).
174. Lee, D. S., Jeon, B. G., Ihm, C., Park, J. K., & Jung, M. Y. A simple and smart telemedicine device for developing regions: a pocket-sized colorimetric reader. *Lab on a Chip* **11**, 120-126 (2011).
175. Li, J. J., Ouellette, A. L., Giovangrandi, L., Cooper, D. E., Ricco, A. J., & Kovacs, G. T. Optical scanner for immunoassays with up-converting phosphorescent labels. *IEEE Transactions on Biomedical Engineering* **55**, 1560-1571 (2008).
176. Kuswandi, B., Huskens, J., & Verboom, W. Optical sensing systems for microfluidic devices: a review. *Analytica Chimica Acta* **601**, 141-155 (2007).
177. Jianchun, M., Qing, Y., Wenyuan, Z., Wangwei, H., & Jianguo, T. Development and study of lateral flow test strip reader based on embedded system. In *2011 10th International Conference on Electronic Measurement & Instruments (ICEMI)* **1**, 201-204 (2001).
178. Huang, L. *et al.* A simple optical reader for upconverting phosphor particles captured on lateral flow strip. *IEEE Sensors Journal* **9**, 1185-1191 (2009).
179. Wongwilai, W., Lapanantnoppakhun, S., Grudpan, S., & Grudpan, K. Webcam camera as a detector for a simple lab-on-chip time based approach. *Talanta* **81**, 1137-1141 (2010).

180. Hanes, R., & Borich, D. Beacon Sciences: Commercialisation from biothreat detection to beauty enhancement. *Journal of Commercial Biotechnology* **15**, 347-359 (2009).
181. Li, Z., Wang, Y., Wang, J., Tang, Z., Pounds, J. G., & Lin, Y. Rapid and sensitive detection of protein biomarker using a portable fluorescence biosensor based on quantum dots and a lateral flow test strip. *Analytical Chemistry* **82**, 7008-7014 (2010).
182. Lee, D. S., Jung, M. Y., Jeon, B. G., & Sohn, M. J. Novel optical absorbance-based multi-analytes detection module using a tri-chromatic LED, PDs and plastic optical fibers and its application to a palm-sized urine test strip reader. In *2010 IEEE Sensors*, 1411-1414 (2010).
183. Pattanasin, S. *et al.* Evaluation of a new Plasmodium lactate dehydrogenase assay (OptiMAL-IT®) for the detection of malaria. *Transactions of the Royal Society of Tropical Medicine and Hygiene* **97**, 672-674 (2003).
184. Moody, A. H. & Chiodini, P.L. Non-microscopic method for malaria diagnosis using OptiMAL IT, a second-generation dipstick for malaria pLDH antigen detection. *British Journal of Biomedical Science* **59**, 228-231 (2002).
185. Moody, A. Rapid diagnostic tests for malaria parasites. *Clinical Microbiology Reviews* **15**, 66-78 (2002).